Accumulating Positrons in an Ion Trap

A thesis presented

by

Loren Dean Haarsma

to

The Department of Physics

in partial fulfillment of the requirements

for the degree of

Doctor of Philosophy

in the subject of

Physics

Harvard University

Cambridge, Massachusetts

May 1994

Abstract

Accumulating Positrons in an Ion Trap

by Loren Dean Haarsma

Thesis advisor: Professor Gerald Gabrielse
Department of Physics, Harvard University

A Penning trap which accumulates positrons in a cryogenic, ultra-high vacuum has been demonstrated. Positrons from a 10 mCi sodium-22 source are moderated by a carefully prepared tungsten (110) crystal and enter the trap through an entrance tube in the endcap electrode. Due to the electric potentials at the entrance aperture and the positrons' magnetron motion, a fraction of the moderated positrons dissipate sufficient energy in a damping circuit to be trapped. After positrons have accumulated for some time, they are moved to the center of the trap via magnetron sideband cooling and counted non-destructively by their interaction with the circuit. With optimal adjustment of the experimental parameters, 0.2 positrons are accumulated per second, which is near the expected performance for this apparatus. Accumulation of more than 3.6×10^4 positrons at one time has been demonstrated; the cryogenic vacuum and trap stability should allow positrons to accumulate indefinitely, limited only by trap capacity (more than three orders of magnitude higher in this case). The design and high vacuum operation of this trap make it easily compatible with existing ion traps, opening the way for low-temperature antihydrogen production and for ion cooling applications. Modifications in trap design and moderator preparation which could lead to substantially higher trapping rates are discussed.

Contents

Acknowledgments

I would like to thank my advisor, Professor Gerald Gabrielse, for providing guidance, a good work environment, and an enjoyable thesis topic. I am also very grateful for the contributions of Dr. Benjamin Brown, who helped design and build the positron trapping apparatus, and Dr. Kamal Abdullah, who helped make it work.

Dr. Steve Rolston, Dr. Luis Orozco, and Dr. Won Ho Jhe provided help early in my thesis work, especially providing insights on antihydrogen recombination and helping with initial stages of the proton/electron recombination trap; David Hall gave valuable assistance during the latter stages of the experiment and analysis. I have had the good fortune of interacting with Joseph Tan, Ching-Hua Tseng, Robert Tjoelker, Xiang Fei, David Phillips, Anton Khabbaz, Daphna Enzer, Lisa Lapidus, Paul Janzen, and Steve Peil.

I am grateful to C. Cantor and K. Lynn for our profitable discussions about positron moderators, to T. O'Neil and M. Glinsky for calculating three-body recombination rates in high magnetic fields, to Capp Spindt for his patience and assistance with the field emission point arrays, and to Jan Ragusa for help in navigating the university bureaucracy.

Early theoretical work for this thesis was done at the University of Washington. Funding came from the Office of Naval Research, with earlier support from the National Science Foundation.

I especially want to thank my parents, Henry and Beth, for all of their support, encouragement, and prayers throughout the years, and Deborah Becker, who makes the future look especially bright.

Publications during Ph.D. study

1. "Antihydrogen Production,"
   (with G. Gabrielse, S.L. Rolston, and W. Kells)
   in *Laser Spectroscopy VIII,* edited by W. Persson and S. Svanberg (Springer-Verlag, New York, 1987), p. 26.

2. "Antihydrogen Production with Cold Trapped Plasmas,"
   (with G. Gabrielse, S.L. Rolston, and W. Kells)
   Phys. Lett. **A129**, 38 (1988).

3. "Electrical Resistivity and Thermopower of the Liquid Alloy MgZn,"
   (with M. Walhout and J.B. Van Zytveld)
   J. Phys: Condens. Matter **1**, 2923 (1989).

4. "Open-endcap Penning Traps for High Precision Experiments,"
   (with G. Gabrielse and S.L. Rolston)
   Int. J. of Mass Spectrom. and Ion Proc. **88**, 319 (1989).

5. "Cylindrical Penning Traps and Self-Shielding Superconducting Solenoids for High Precision Experiments,"
   (with W. Jhe, D. Phillips, J. Tan, and G. Gabrielse)
   in *Proc. of the Workshop on Physics with Penning Traps*, Lertopet, Sweden. Physica Scripta **46**, 264 (1992); RPS **20**, 44 (1993).

6. "Extremely Cold Antiprotons for Mass Measurement and Antihydrogen,"
   (with G. Gabrielse, W. Jhe, D. Phillips, W. Quint, C. Tseng, K. Abdullah, J. Gröbner, and H. Kalinowsky)
   in *Atomic Physics 13, Thirteenth International Conference on Atomic Physics*, (American Institute of Physics, New York, 1993), p. 85.

7. "A Single Trapped Antiproton and Antiprotons for Antihydrogen Production,"
   (with G. Gabrielse, W. Jhe, D. Phillips, W. Quint, K. Abdullah, H. Kalinowsky, and J. Gröbner)
   in *Proceedings of Workshop of Traps for Antimatter and Radioactive Nuclei*, (TRIUMF), Vancouver, British Columbia, Canada (in press).

8. "Extremely Cold Positrons for Antihydrogen Production,"
   (with G. Gabrielse and K. Abdullah)
   Hyperfine Interactions **76**, 143 (1993).

9. "Extremely Cold Antiprotons for Antihydrogen Production,"
   (with G. Gabrielse, W. Jhe, D. Phillips, W. Quint, C. Tseng, K. Abdullah, J. Gröbner, and H. Kalinowsky)
   Hyperfine Interactions **76**, 81 (1993).

10. "Trapped Positrons for Ion Cooling and Antihydrogen,"
    (with G. Gabrielse and K. Abdullah)
    (in press).

11. "Successful Accumulation of Positrons for Antihydrogen Production and Ion Cooling"
    (with G. Gabrielse and K. Abdullah)
    (to be published).

List of Figures

Chapter 1

Introduction

1.1 Motivation

Positrons were first captured in a Penning trap more than ten years ago at the University of Washington in an apparatus designed for precision measurements on positrons [1,2,3]. The loading rate into their trap was only a few positrons per hour (compared with 10^7 positrons per second which were supplied by their 0.5 milli-Curie radioactive source), since the range of energies with which the positrons entered their trap (hundreds of keV) was much greater than the range of energies which could be captured (a few meV).

During the last decade, great progress has been made in producing slow, nearly monoenergetic positron beams through the use of positron moderators [4,5,6,7]. A carefully prepared moderator can produce positron beams which have energy spreads of less than 100 meV, at an efficiency of nearly one slow positron per thousand fast incident positrons. This experiment utilizes such a moderator to increase by orders of magnitude the rate at which positrons are accumulated in vacuum [8,9].

Antiprotons were recently captured in a Penning trap [10], raising the possibility of using trapped positrons to make antihydrogen at low temperatures [11]. Antiprotons from the Low Energy Antiproton storage Ring (LEAR) at CERN

were slowed from their storage energy of 5 MeV via collisions with matter in a degrader foil [10,12], and the Penning trap electrodes were biased shortly after the arrival of the antiproton pulse. Those which emerged from the degrader foil in the energy range 0 to 3 keV were trapped. The antiprotons were further cooled to liquid helium temperatures by collisions with trapped electrons [13] and by coupling their motion to a damping circuit. By stacking several pulses of approximately 10^8 antiprotons from LEAR, as many as 2×10^5 antiprotons have been held at one time in a trap with a volume of about 1 cm^3 and a temperature of 4 K [14]. A cryogenically cooled Penning trap allows antimatter to be stored for long periods of time. The antiproton lifetime in this trap has been demonstrated to be at least several months, setting an upper limit of 5×10^{-17} Torr for the background pressure in the trap [15].

Antihydrogen could be formed at a high instantaneous rate by merging cold, trapped clouds of positrons and antiprotons in the same volume [11]. Since the antihydrogen would already be localized in space and quite cold, this raises the possibility of trapping the antihydrogen in a superimposed magnetic dipole trap, as has been done with hydrogen [16,17,18]. Spectroscopic comparisons of hydrogen and antihydrogen could provide extremely sensitive measurements of CPT invariance. Therefore, with the success of the antiproton trap, it became desirable to build a trap which could accumulate a sufficient number of positrons in a high vacuum at a sufficiently high rate to make antihydrogen production feasible. The design of that trap, and its performance, are the primary focus of this thesis.

Other uses for trapped positrons include the cooling of highly stripped ions in the same way that electrons are used to cool trapped antiprotons [13]. In addition, a limit on the positron lifetime can be measured by monitoring a large cloud of trapped positrons. In the same way, monitoring the loss of positrons from a Penning trap could provide a means of measuring the background gas density at pressures below which ion gauges do not operate ($\sim 10^{-12}$ Torr).

The most precise measurements of the properties of positrons [3] and electrons

were made in Penning traps under ultra-high vacuum conditions at 4 K. Plans are currently in progress to improve these measurements on electrons by utilizing a dilution refrigerator. The positron trap described here could easily be adapted to operate at dilution refrigerator temperatures, which would allow more precise measurements of the positron's magnetic moment and charge-to-mass ratio as additional tests of CPT invariance. Moreover, its relatively high trapping efficiency would allow it to operate with a much smaller radioactive source—assuming the experimenter only wants to study one or two positrons at a time—which would reduce the frequency of positrons "spontaneously" loading into the trap, which was occasionally a problem in earlier experiments [3]. Such a trap could also be used to measure the properties of positron moderators at temperatures below 4 K, which has not yet been explored experimentally. Antihydrogen formation and other potential uses of trapped positrons are discussed in more detail in Chapter 7.

1.2 Design constraints

It should be possible to trap and accumulate positrons in the same way as antiprotons, by using an accelerator facility to produce and deliver pulses of positrons to a Penning trap. However, this would not be convenient for initial attempts to make antihydrogen insofar as both the antiproton source and the positron source must be located at the same facility. Currently, the only source for antiprotons at energies below 100 MeV is LEAR at CERN. Fortunately, several readily available radioactive nuclei produce positrons during the course of their decay. These sources are generally quite small physically (less than 1 cm^3) and therefore can be easily transported to the antiproton trap.

Radionuclei (for example, sodium-22) produce positrons continuously over a wide range of energies. Moderators (Chapter 3) can be used to slow the positrons to energies below 1 eV; however, additional energy must be extracted from the positrons while they travel through the trap volume in order for them to remain

in the trap.

One way to accomplish this is by periodically ramping the electrode voltages, accumulating positrons during each ramp cycle. Since positrons have high velocities even at these low energies (6×10^7 cm/sec at 1 eV), very rapid voltage ramping is required. Such a trap has been built by Conti *et. al.* at the University of Michigan [19]. A typical duty cycle for the Michigan apparatus is 100 to 1000 Hz, accumulating ~ 200 positrons per pulse from a 30 mCi ^{22}Na source. However, this technique is more suited to ***bunching*** than to long-term accumulation. (The Michigan trap is rapidly dumped at the end of each cycle.) For long-term accumulation of positrons, the duty cycle would need to be drastically reduced to allow time for the positrons to cool at the end of each upward ramping of the electrode voltages.

One way to extract energy from slow positrons ***continuously*** is by using a neutral buffer gas, as has been demonstrated by Surko *et. al.* at AT&T Bell Labs and U.C. San Diego [20]. Inelastic collisions with buffer gas atoms inside the trap cause a significant fraction of the positrons to remain trapped. However, the buffer gas (nitrogen) also limits the positron lifetime through annihilation. Background hydrocarbon molecules are also a concern with this design, since their positron annihilation cross-section can be orders of magnitude larger than for nitrogen [21]. The longest positron lifetimes achieved in this trap were of order ten minutes. This lifetime is unacceptably short, especially considering that antiprotons (which are much harder to obtain than positrons) will eventually share the same vacuum environment. It is unclear that it is possible to adapt this technique to the cryogenic, ultra-high vacuums required for antihydrogen study.

Therefore, we chose to use a resistive damping technique [1,8,22] to extract energy from the positrons. The positrons' motion through the trap induces currents in an LRC circuit which is connected to the trap electrodes; energy is dissipated in the resistor. This technique works even under cryogenic, ultra-high vacuum conditions. It also works continuously; there is no duty cycle to slow the over-

all accumulation rate. The trapping efficiency is high enough so that—in a few hours or a few days—a sufficient number of positrons can be accumulated to make antihydrogen production feasible [11], with a radioactive source small enough to ensure the safety of the experimenters. Finally, this technique meets the criteria of being easily portable and adaptable to the existing antiproton trap.

1.3 Overview of remaining chapters

The remaining chapters follow the positrons as they are emitted from the radioactive source, moderated, loaded into the trap, detected, and finally accumulated. Chapter 2 shows the overall design of the Penning trap and support apparatus, and calculates the fraction of positrons which reach the moderator from the radioactive source. Chapter 3 shows the effect of the moderator on the positron energy distribution. Chapter 4 starts with a quick review of the dynamics of a charged particle in a Penning trap, and proceeds to describe the mechanism by which positrons are trapped. An overall trapping efficiency is also calculated. The technique by which positrons are detected and counted is described in Chapter 5, and Chapter 6 shows examples of positron accumulation and storage. Finally, Chapter 7 explores potential applications.

Chapter 2

Positron flux on the moderator

Positrons from radioactive decay have an energy range of several hundred keV. Therefore, the first step in achieving a high positron trapping rate is to maximize the flux of high-energy positrons onto the positron moderator, where they are slowed to sub-eV energies. Because the Penning trap and moderator are in a high magnetic field (5.9 Tesla), the simplest way would be to mount the positron source very close to the moderator inside the trap's vacuum enclosure and allow the strong magnetic field to guide the positrons to the moderator. Unfortunately, the experimenters must spend a considerable amount of time in close proximity to the trap's vacuum enclosure (hereafter referred to as the "trap can") while they make vacuum seals and test electronics. Therefore, we designed a dewar and support system which can accept the radioactive source and position it *after* the trap can has been sealed, tested, and lowered into the magnet. This minimizes the experimenters' exposure to harmful gamma radiation. The entire apparatus is described in Section 2.2.

Once the radioactive source is properly positioned, positrons follow the strong magnetic field lines, as described in Section 2.3, all the way to the moderator, where their flux can be measured using the lock-in technique described in Section 2.4.

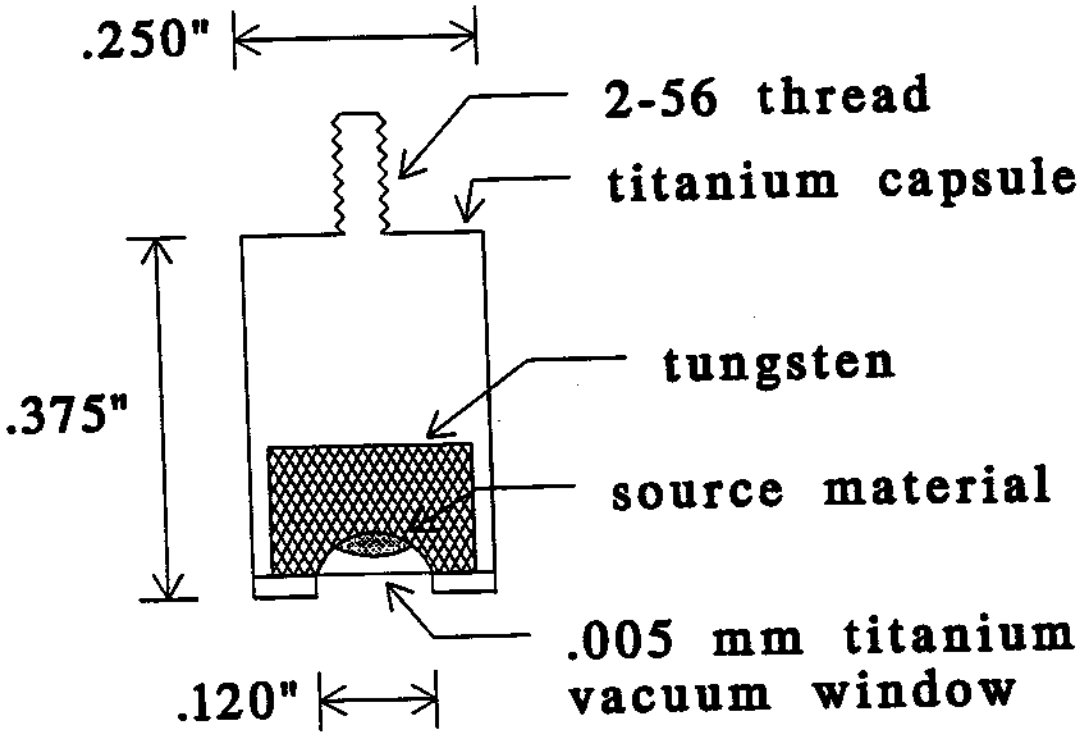

Figure 2.1: Cross section of ^{22}Na positron source capsule.

2.1 The positron source

There are only a few positron-producing radionuclei with half-lives sufficiently long to be useful in this application. The most promising are cobalt-58, which has a half-life of 72 days and a positron efficiency (*i.e.* the fraction of all decays which produce positrons) of 15 percent, and sodium-22, which has a half-life of 2.6 years and a positron efficiency of 90 percent. We also require a source which can safely withstand repeated cycling to high vacuum and liquid helium temperatures.

We contracted with New England Nuclear/Dupont to obtain a 20 milli-Curie ^{22}Na sealed source, pictured in Fig. 2.1. The radioactive material is in the form of a paste which has an active area with a radius $r_s \simeq 1.0$ mm. The capsule

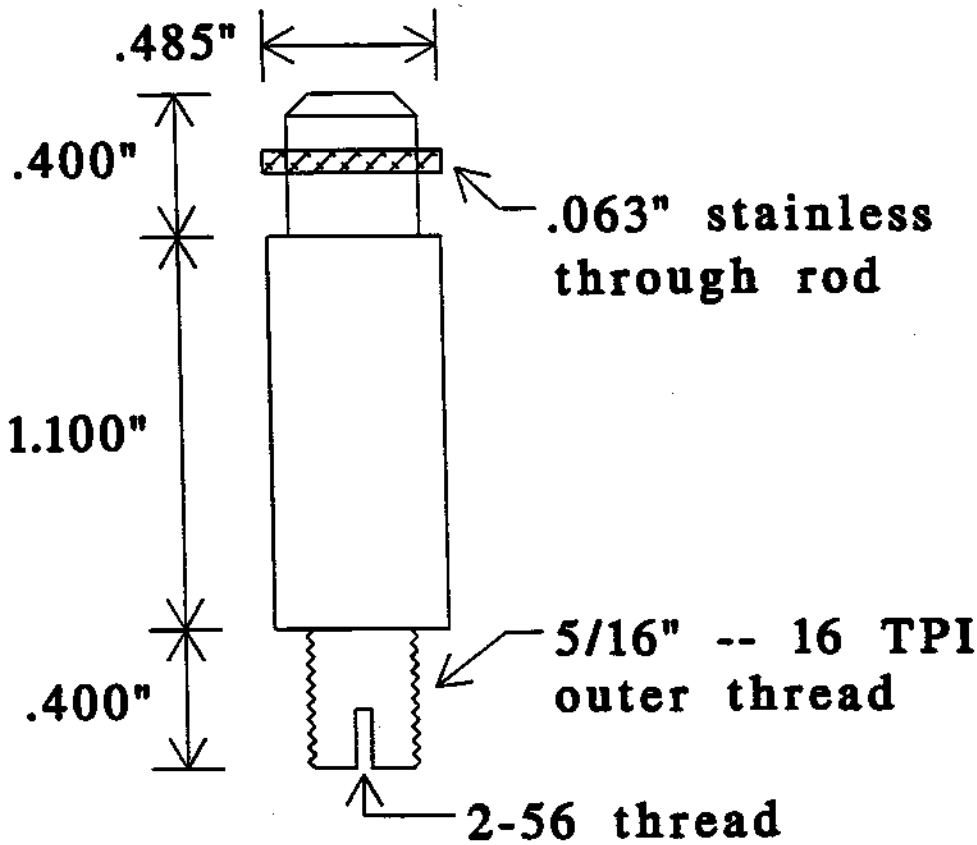

Figure 2.2: Elkonite plug used for loading and unloading the source capsule.

was sealed by electron beam welding a 5 μm titanium window over the mouth of the capsule. A tungsten backing plate increases positron back-scatter towards the window and thereby increases positron emission in the forward direction.

This source capsule is mounted onto the bottom of an Elkonite (90% tungsten, 10% copper) plug, shown in Fig. 2.2. The top of this plug has a 0.063 inch diameter horizontal through rod which allows it to be grasped by a spring-loaded "bayonet socket," shown in Fig. 2.3, at the end of a 1.5 meter rod. The outer threads on the Elkonite plug match threads inside a lead container used to store the source when it is not in use. When the radioactive source capsule was received, it was mounted "by hand" (actually, a pair of ten inch long tongs were used) into the 2-56 inner threads of the Elkonite plug. Thereafter, the source capsule and plug

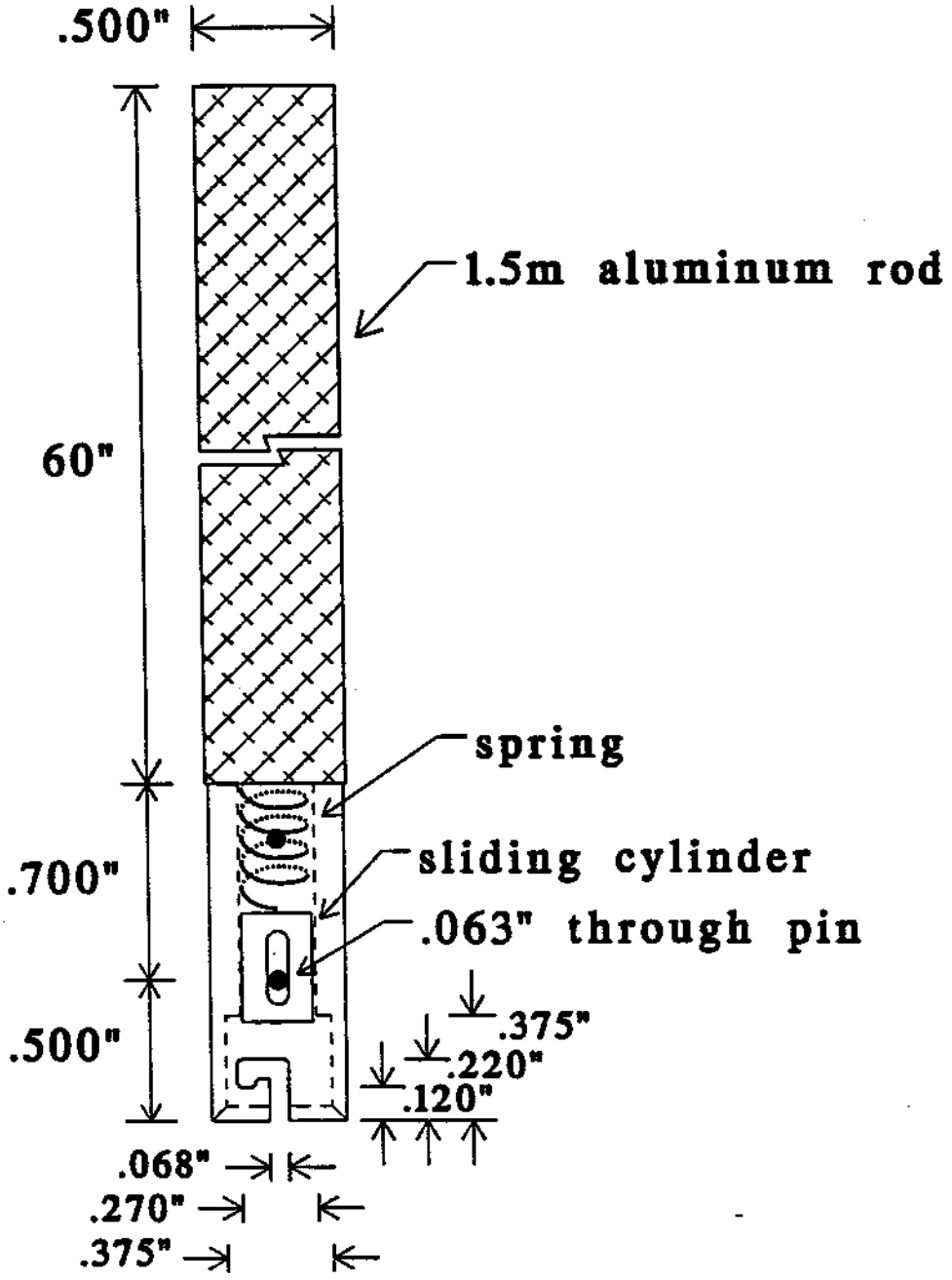

Figure 2.3: "Bayonet socket" attached (with internal spring) to the end of a 1.5 meter rod used for manipulating the source capsule and plug.

were manipulated exclusively by means of the 1.5 meter loading rod.

New England Nuclear estimates that, even if the source material is deposited properly into the capsule, 50% of the positrons emitted in the forward direction (towards the window) are absorbed within the capsule, due to the thickness of the source material. This is consistent with our measurements (Section 2.4). Therefore, increasing the source activity by increasing the source material thickness would cause little increase in positron emission. Increasing the active area of the source material would not increase the flux on the moderator because of beam collimation at the Penning trap entrance apertures (Section 2.3).

2.2 Apparatus design from source to moderator

The liquid helium dewar and overall support system for this positron trap is designed to be highly compatible with the existing apparatus used at CERN to capture and study antiprotons (described in Refs. [23] and [24]). Apart from the actual Penning trap electrodes, the components of the two systems are nearly identical. This will greatly facilitate the next stage of the experiment, when positrons and antiprotons are simultaneously captured in the same vacuum enclosure and merged to form antihydrogen.

2.2.1 Magnet, dewar, support system, and vacuum enclosure

A large-scale picture of the apparatus is given in Fig. 2.4. The superconducting solenoid made by Nalorac Cryogenics can produce a 5.9 Tesla field which is uniform to within one part in 10^8 over a volume of approximately 1 cm^3—roughly the volume of the interior of the Penning trap. The inner bore of the magnet's dewar has a diameter of 4 inches, and can be cooled via a connection to a liquid nitrogen reservoir. The Penning trap's support apparatus and vacuum enclosure

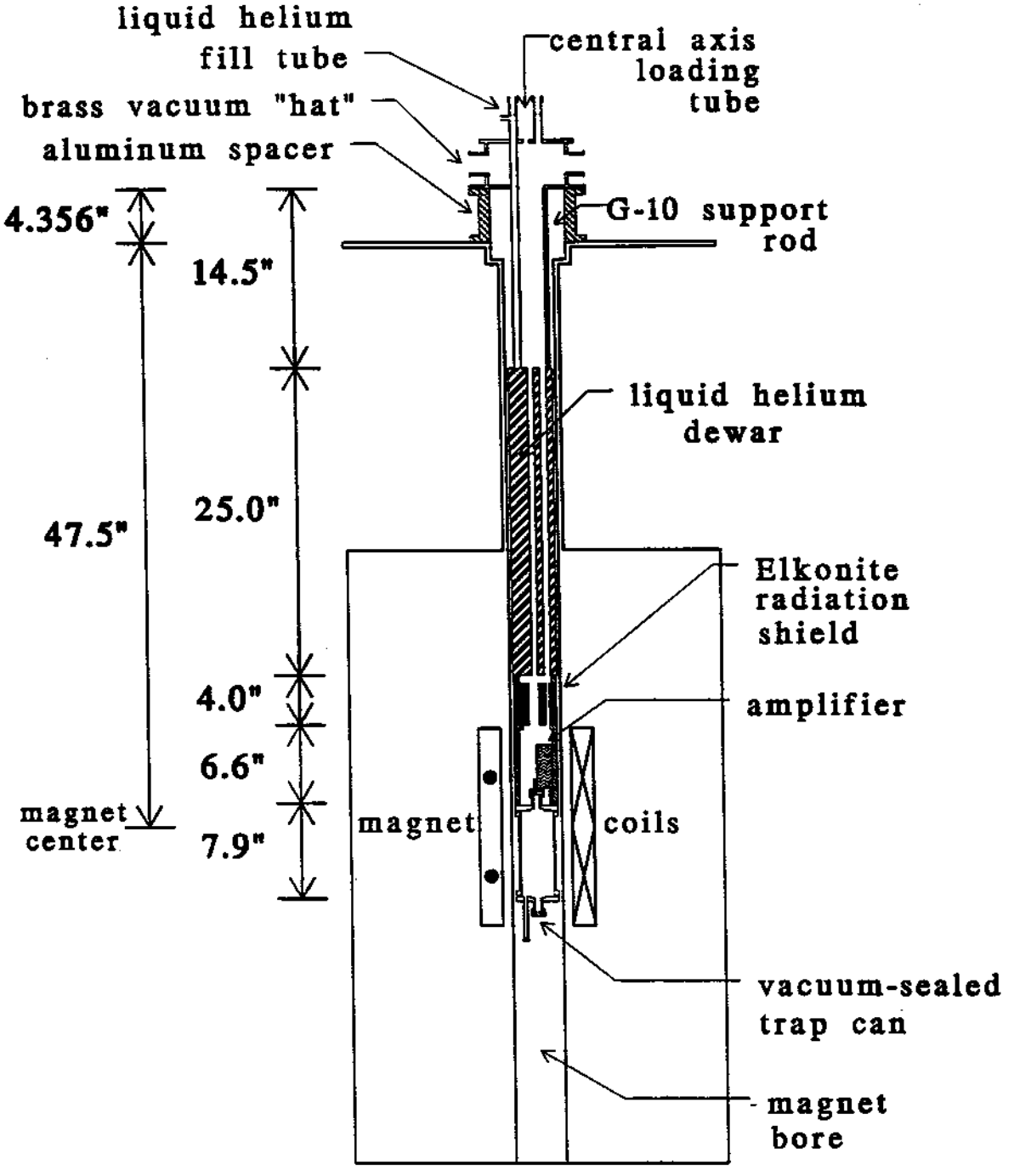

Figure 2.4: Scaled picture of superconducting magnet, liquid helium dewar, and support system for the positron trap.

have outer diameters of 3.5 inches or less so that they can easily be inserted into and withdrawn from the magnet bore. The magnet bore is evacuated to less than 10^{-6} Torr during normal operation.

The positron trapping apparatus has a liquid helium dewar, separate from the magnet's dewar, which has a volume of about 2.3 liters and a hold time of three days when the magnet's inner bore is evacuated and a thermal radiation shield (thermally connected to the cold helium exhaust gas) is installed between the dewar and the magnet bore wall. This helium dewar also has a 0.5 inch diameter tube down its center, through the entire length, which allows us to insert and extract the radioactive source without removing the apparatus from the magnet bore.

A 3.5 inch diameter Elkonite (90% tungsten, 10% copper) shield is bolted onto the bottom of the trap's liquid helium dewar. Approximately 0.8 inches was bored out of its center, and the radioactive source normally resides in the center of this shield, as is shown in Fig. 2.5. Elkonite has a density of about 19 g/cm^3, so this provides most of the gamma ray shielding required to protect the experimenters during normal operation. Care had to be taken in the choice of material, since some commercially available "heavy metal" materials are sintered and contain copper-nickel alloys which could undergo a ferromagnetic transition at temperatures between 77 K and 4 K [25], which would have been disastrous. With the additional shielding provided by the magnet itself, two inches of lead stacked onto the upper shoulder of the magnet dewar, a quarter inch of lead wrapped around the upper neck of the magnet, and eight inches of concrete stacked around the side of the magnet, the gamma radiation produced by the 20 mCi source is reduced to one or two times natural background measured outside the shielding.

A 7 inch long copper stand is bolted to the bottom of the Elkonite shield. This region between the Elkonite and the trap can allows easy access to the electrical feedthroughs on the top of the trap can. It provides space for the sensitive amplifier circuit described in Chapter 5 as well as other electronic components (low-pass

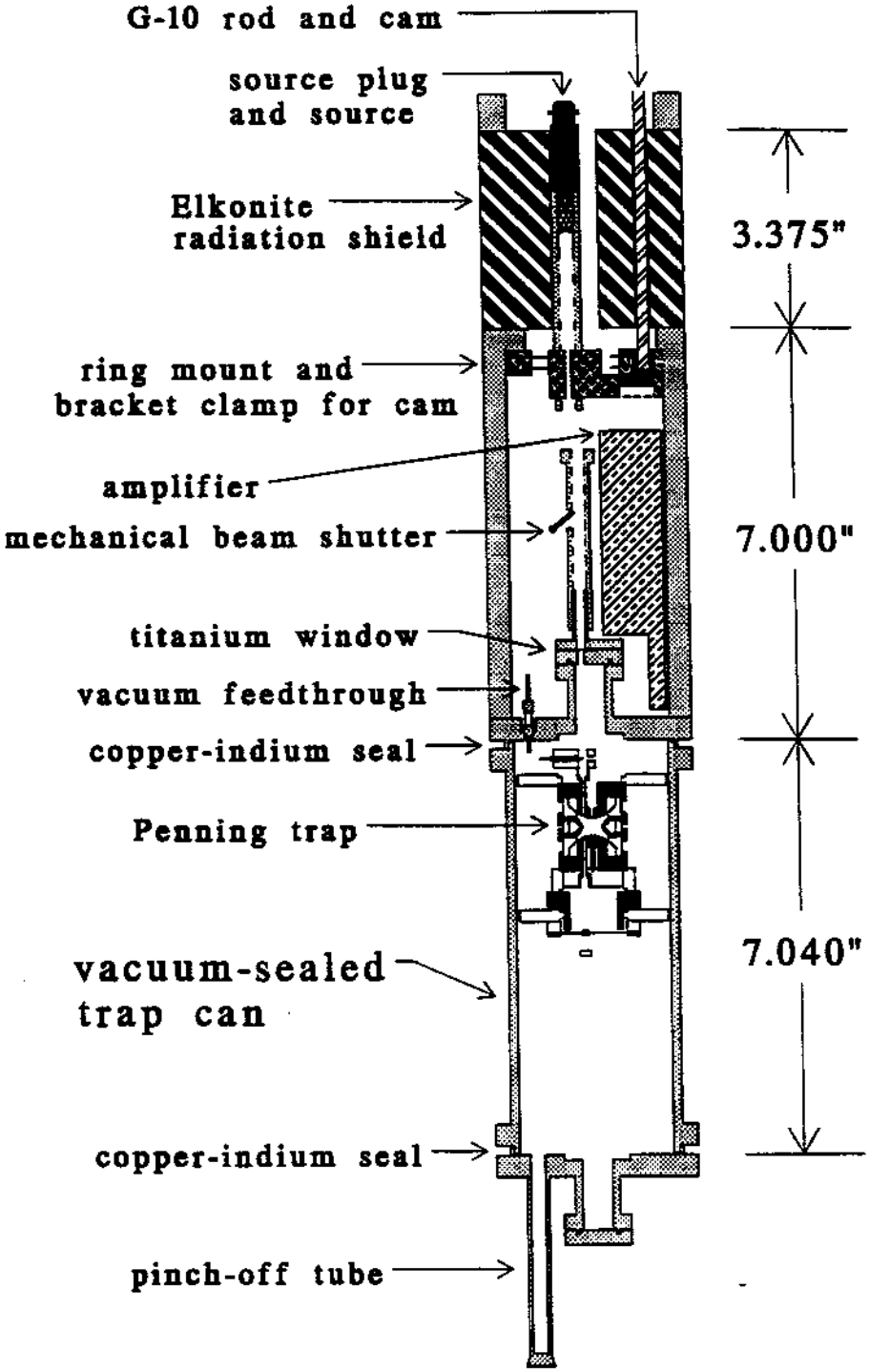

Figure 2.5: Close-up picture of the vacuum-sealed trap can, stand, and Elkonite radiation shield. The positions of the radioactive source and the Penning trap are also shown.

filters, etc.), and for the positron source positioner described in Section 2.2.2.

The Penning trap is contained a separate vacuum enclosure, the "trap can." After the Penning trap is assembled, the trap can is sealed with compressed indium o-rings located between the copper components of the trap can. It is evacuated at room temperature to about 10^{-7} Torr through a pinch-off tube, then sealed. When the apparatus is lowered into the magnet bore and the trap can is cooled to 4 K by thermal contact to the liquid helium dewar, the pressure inside the can drops to levels suitable for long-term storage of antimatter, a pressure below 5×10^{-17} Torr having been observed [15]. Energetic positrons from the ^{22}Na source enter the trap can through a 5 μm titanium window, which is held in place by another indium compression seal, as shown in Fig. 2.5.

The overall apparatus is designed so that, after thermal contraction following cooldown to liquid helium temperatures, the center of the Penning trap is located in the center of the magnetic field. Construction materials such as OFE copper were chosen with as small a magnetic susceptibility as possible in order to minimize field inhomogeneities.

2.2.2 Positioning the radioactive source

The radioactive source is inserted and removed along the central symmetry axis of the trap's helium dewar, which is also the central symmetry axis of the Penning trap. However, positrons must ultimately enter the Penning trap *off* its central symmetry axis (Chapter 4). Moreover, while the Penning trap is located in the center of the superconducting magnet's field, the positron source is located in the magnet's fringing field. It is therefore necessary to move the source radially across the magnetic field lines (from right to left in Fig. 2.5 and 2.6) after the source has been inserted so that the positrons travel along the curving magnetic field lines to the moderator. Figure 2.6 shows an exaggerated view of the magnetic field lines superimposed on the positron source, Penning trap, and moderator.

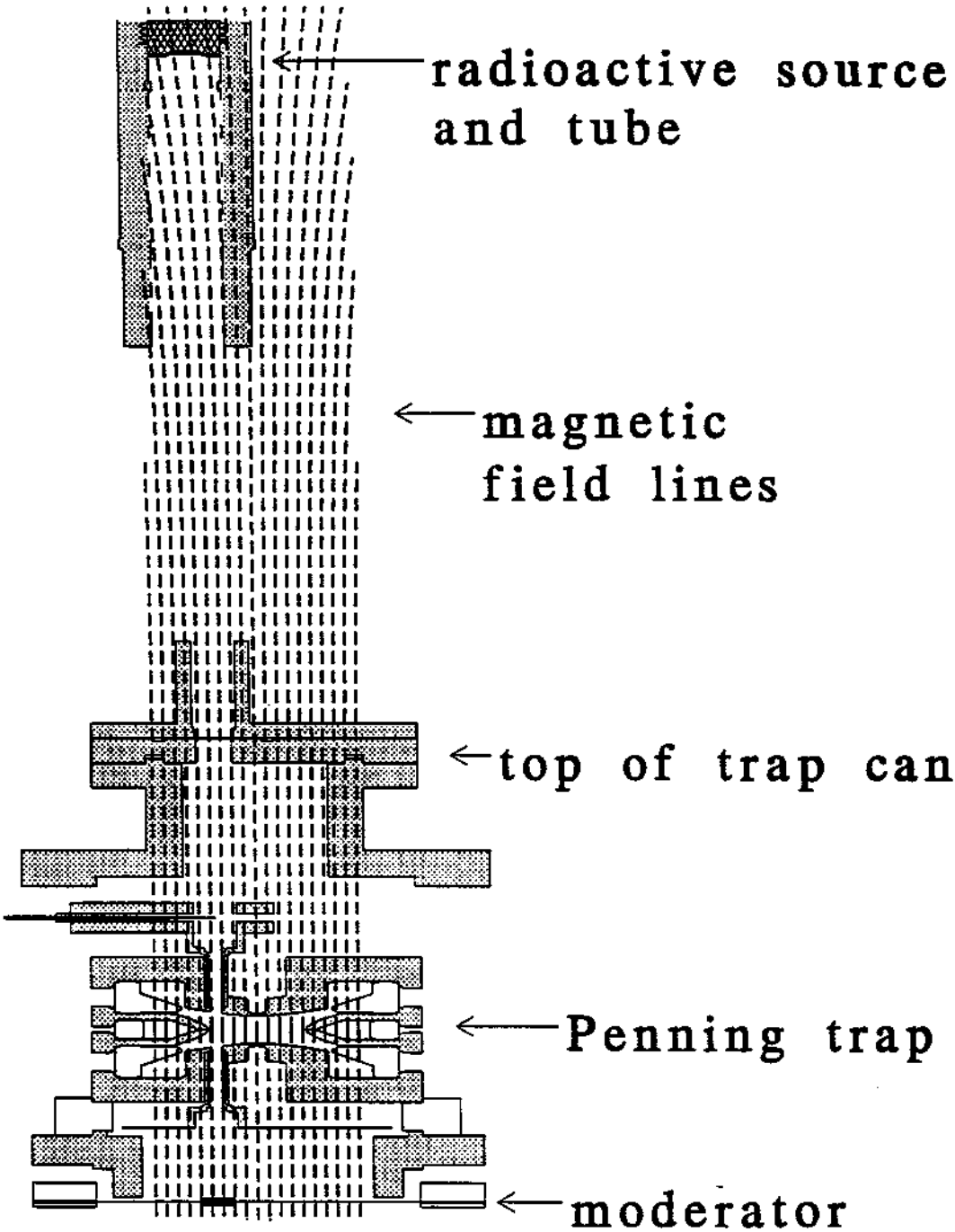

Figure 2.6: Positron source, Penning trap, and moderator. Curving magnetic field lines from the superconducting solenoid are superimposed. The horizontal scale is expanded by a factor of 3 compared to the vertical scale.

Angular alignment of the source with the small entrance holes into the trap relies on careful alignment during trap assembly. The radial adjustment of the source is accomplished by using the cam-and-shaft device (Fig. 2.7) which is mounted immediately below the Elkonite shield; it functions even when the magnet bore is evacuated and at liquid helium temperatures. The Elkonite source plug and the radioactive source are mounted via the 1.5 meter "bayonet" rod into the moving source holder, which is in turn held by the bracket clamp. When the cam rotates, the bracket clamp slides along rods which are held in place by the ring clamp. The cam consists of a 0.55 inch diameter copper disk mounted 0.125 inches off-center from the cam's central axis. A long (thermally insulating) rod made from G-10 (epoxy fiberglass) extends from the cam, through another clearance tube in the helium dewar (located 1 inch off the central symmetry axis) to a motional vacuum feedthrough in the magnet's brass "hat." As the cam rotates, the bracket clamp, source holder, and source move radially in the magnetic field.

Figure 2.9 shows a typical example of the positron flux on the moderator (and also the positron loading rate into the trap) as a function of the cam angle. In one position, chosen to be 0°, the source is located along the central symmetry axis of the dewar and trap. As the cam rotates through 180°, the source moves radially across the magnetic field lines $\sim$ 9 mm. When the source is located $\sim$ 6.6 mm off of the symmetry axis, corresponding to a cam position of 70°, it is in the proper position for positrons to follow the magnetic field lines all the way to the moderator. As the cam continues from 180° to 360° the source moves back to the central axis; therefore, there are two positions in angle which maximize the flux of positrons incident on the moderator.

The entire apparatus was carefully shimmed so that it hung true to vertical, from the brass hat to the bottom of the trap can, to within 0.02°. Even so, because the superconducting solenoid is not properly aligned with its own dewar, we found it necessary to rotate the entire apparatus within the magnet's bore, with certain orientations resulting in no positrons hitting the moderator.

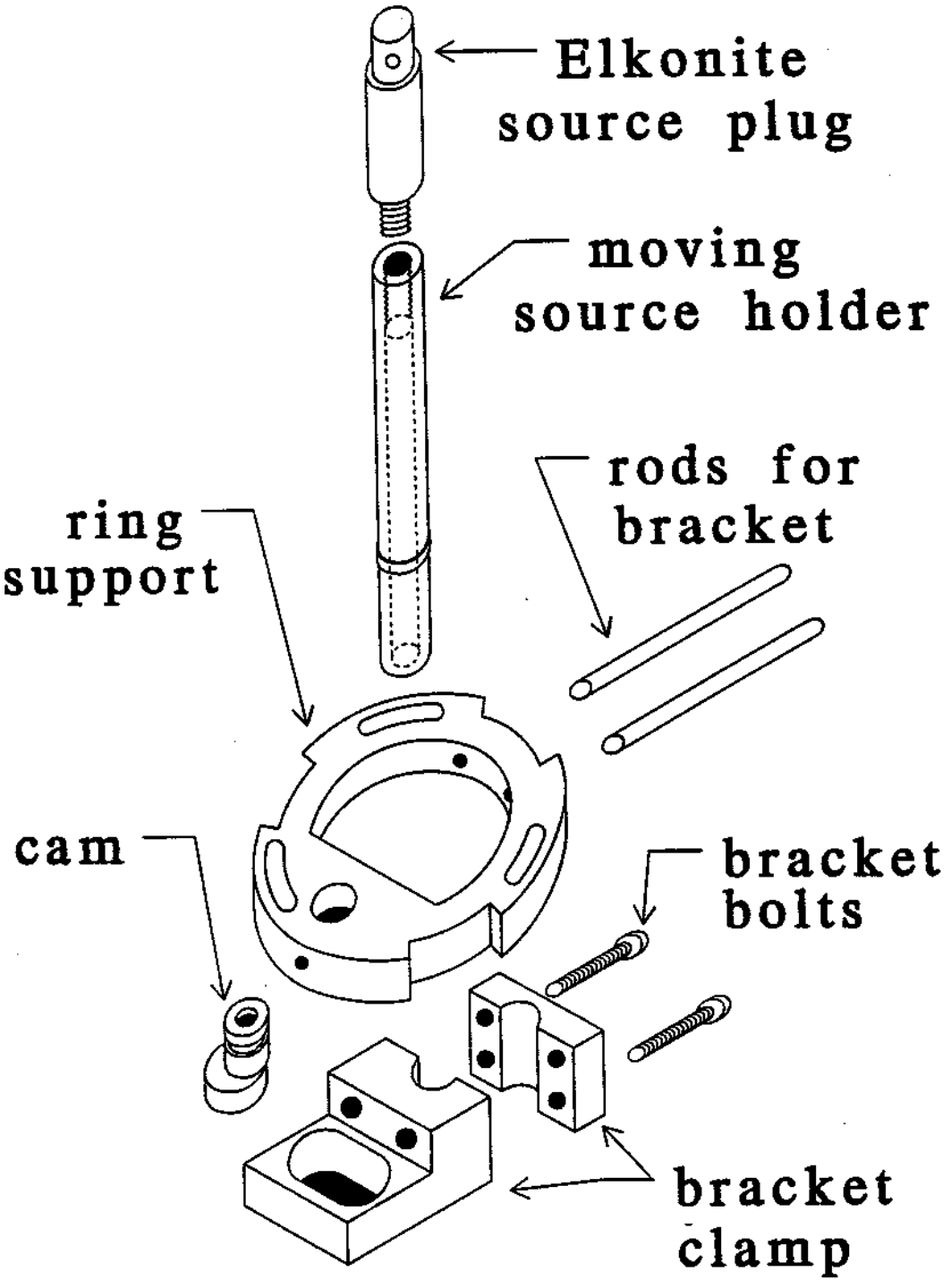

Figure 2.7: Three-dimensional view of the components of the cam-and-shaft device used to hold and position the radioactive source. The cam is held in the ring support by a set screw. As the cam rotates, the bracket clamp and source holder slide along the rods.

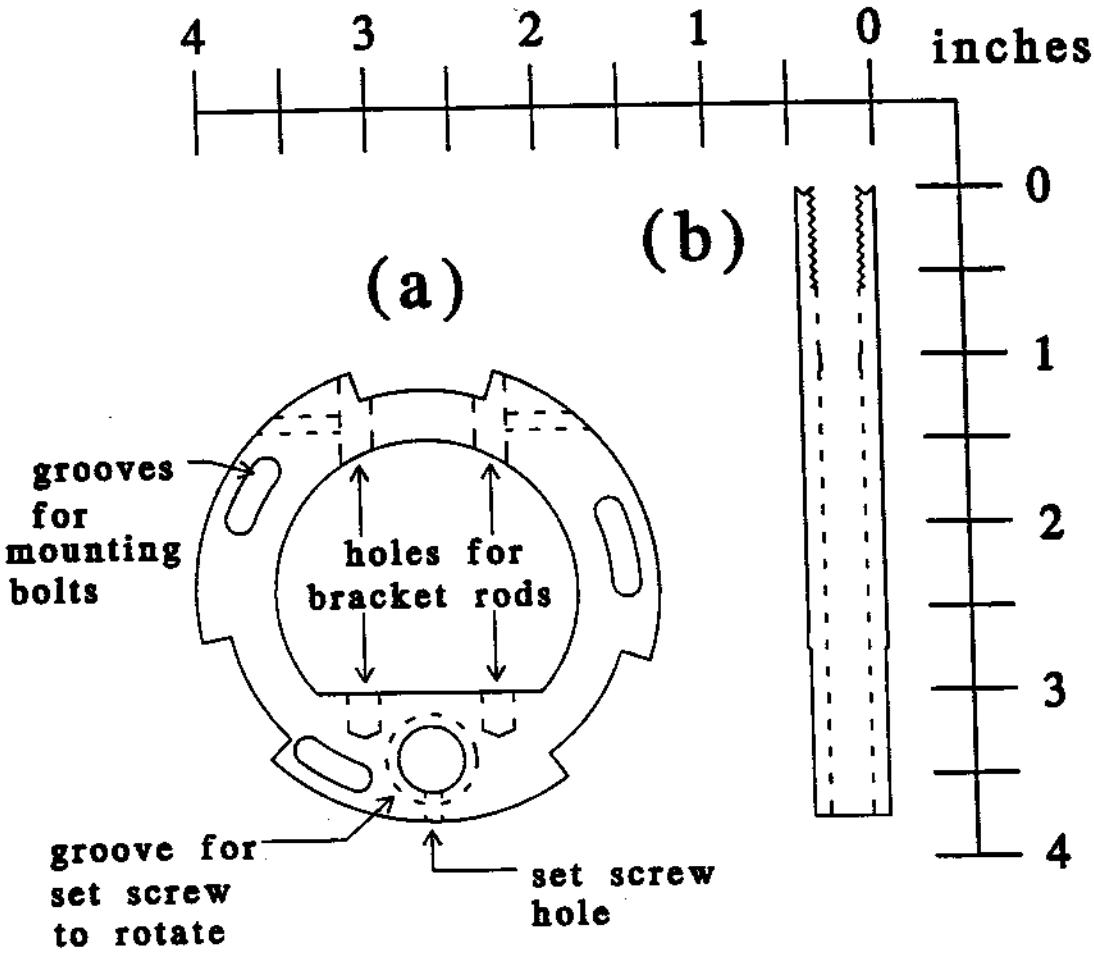

Figure 2.8: Cross-sectional view of (a) the ring clamp, and (b) the moving source holder.

In order to measure the flux of positrons on the moderator, we found it necessary to install a beam shutter between the positron source and the trap can, as shown in Fig. 2.5. This was achieved by attaching a small loop of wire to a flap of non-conductive material (G-10 in this case) thick enough to stop the positrons. Just as in an ordinary current meter, a small electric current through the loop causes it to feel a strong force due to the large magnetic field from the solenoid. The flap and coil are mounted on a hinge so that the flap pivots to block the

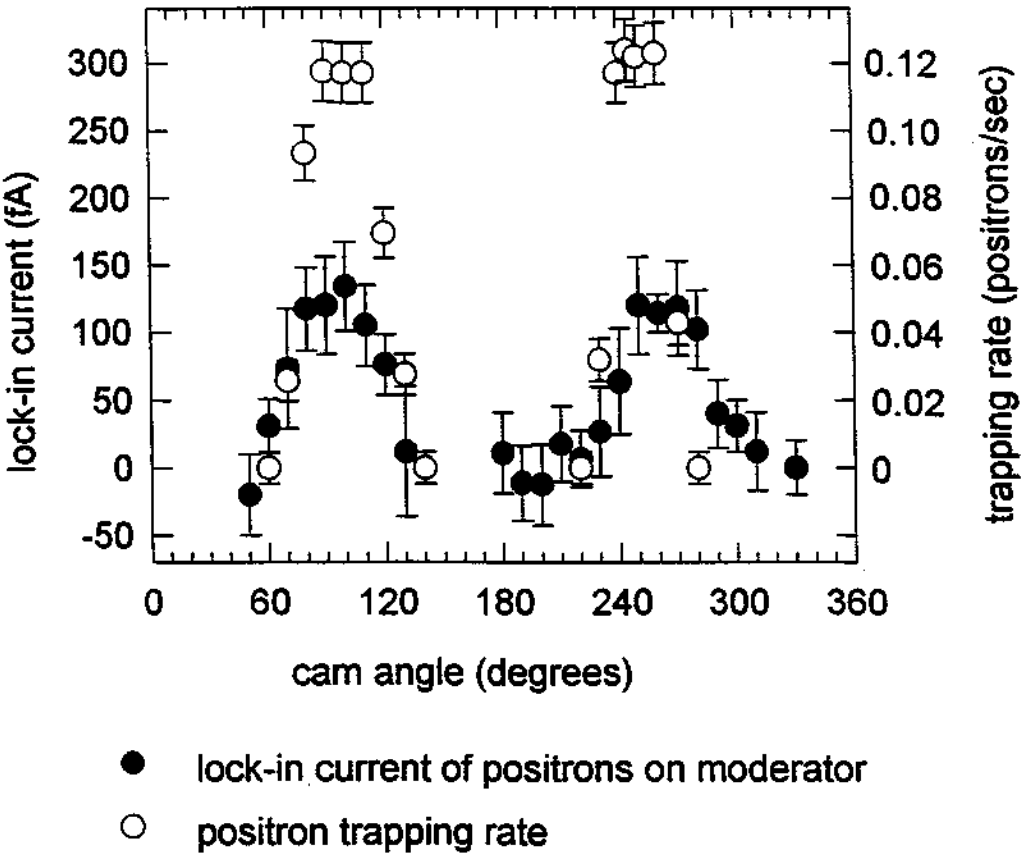

Figure 2.9: The positron trapping rate o, and the measured current of the lock-in detector • due to positron flux on the moderator, as a function of cam angle. The actual positron current into the moderator is 3 to 4 times the measured lock-in value.

positron beam when current flows in one direction, while allowing the positrons to pass when the current is turned off (or made to flow in the opposite direction).

2.2.3 Penning trap and moderator

The Penning trap is pictured in Fig. 2.10. It is very similar in design to Penning traps used for high precision measurements on electrons [22,26,27]. The endcap and ring electrodes are made from OFHC copper; their inner surfaces are machined

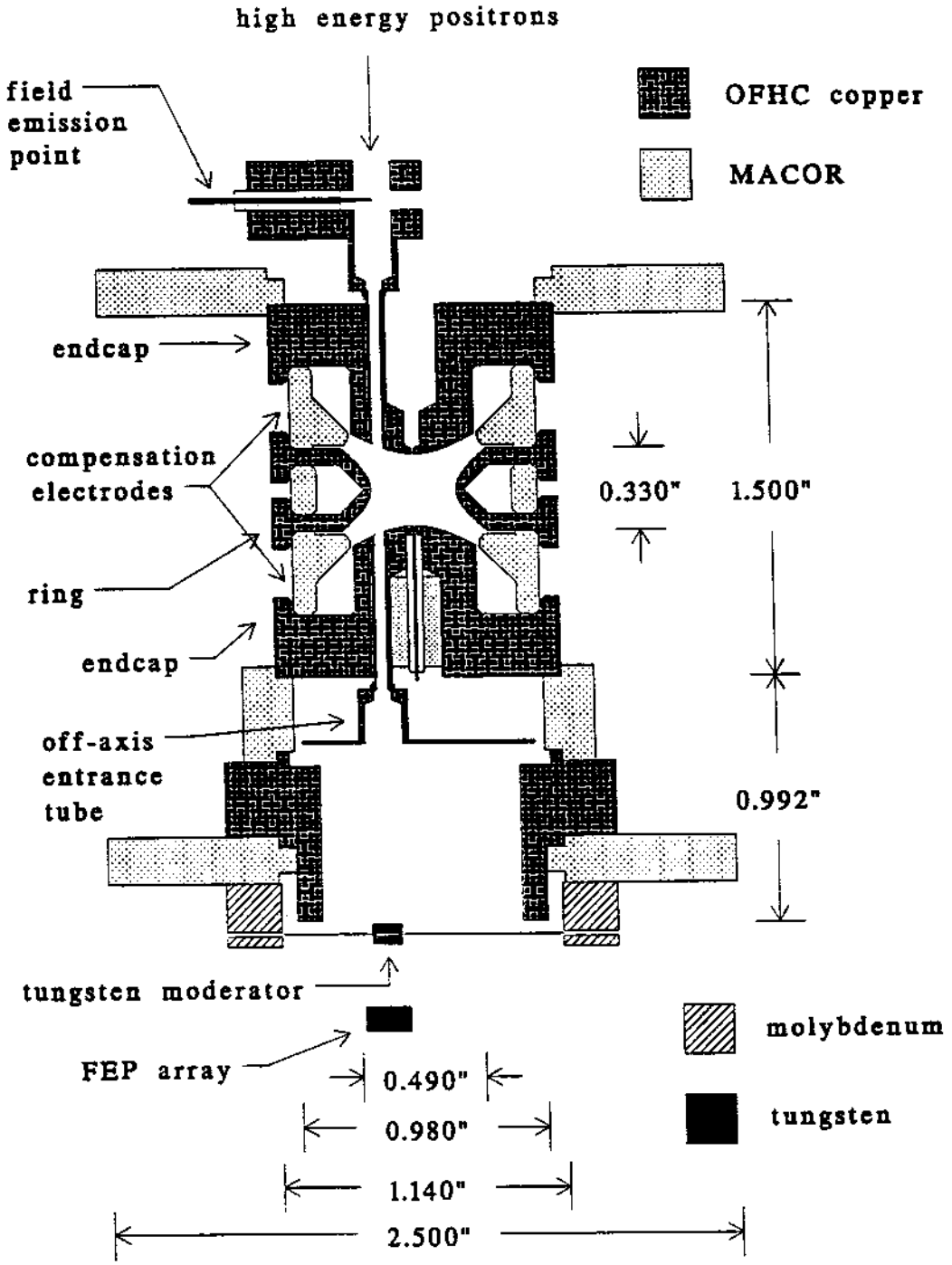

Figure 2.10: Cross section of Penning trap and moderator used for continuous loading of positrons. The entrance tubes are located 0.14 inches from the trap's central symmetry axis.

along hyperbola of revolution around the $\hat{z}$ axis. This hyperbolic geometry insures that the electric potential experienced by the positrons during their first orbits inside the trap volume—when they are still energetic and travel very near to the inner surfaces of the electrodes—is as nearly as possible a pure quadrupole. Other possible electrode geometries (*e.g.* cylindrical) create electrostatic potentials which depart significantly from a quadrupole near the electrode surfaces. The resistive circuit we use to extract energy from the positrons (described in Section 5.1) works most efficiently when the positrons experience a purely quadrupole potential throughout their entire motion (Section 4.3).

The inner surfaces of the endcap and ring electrodes are coated with a thin layer of Aquadag (graphite) to reduce electric field inhomogeneities due to patch effects. The diameter of the ring electrode is $\rho_0 = 0.168$ inches, and the distance between the two endcap electrodes at closest approach is $2z_0 = 0.288$ inches. The endcap electrodes have small holes (0.5 mm diameter) through their centers. Field emission points mounted in these apertures allow us to directly load electrons into the center of the trap. The off-axis apertures in the endcap electrodes are located $\rho_h = 0.140$ inches from the central axis. The apertures themselves have a diameter of 1.0 mm, although the holes drilled into the electrodes have a 2.0 mm diameter which only narrows to 1.0 mm within the last millimeter before the inner surface.

The compensation electrodes are made of MACOR (a machineable ceramic). Their surfaces near the trap's center are plated with copper so that particles inside the trap do not have a direct line-of-sight to a nonconductive surface. The copper plating on the bottom compensation electrode is split into four quadrants to allow for magnetron sideband cooling of the positrons (Section 5.3). The purpose of compensation electrodes is to allow an additional degree of control over the shape of the electrostatic potential inside the trap. Inevitably, the potential provided by the ring and endcap electrodes is not purely quadrupole due to machining uncertainties and truncation of the electrodes. The adjustable voltage applied to the compensation electrodes gives an extra degree of freedom with which to correct

some of those errors.

The entrance tubes are made of OFHC copper with a diameter of ~ 1.4 mm and a wall thickness of just a few tens of microns. They are insulated from the endcap electrodes by thin alumina sleeves.

A field emission point (FEP) is made by electrochemically etching the tip of a 0.5 mm diameter tungsten rod to a sharp point. Biasing the point to a few hundred volts results in an electron emission current which ranges from a few picoamps to hundreds of nanoamps. In addition to the one mounted in the center of the bottom endcap electrode, another FEP is mounted in the horizontal section of the upper entrance tube, with its tip located directly over the endcap's off-axis aperture. This is an important diagnostic feature since it allows us to easily load electrons in the same off-axis position as the positrons are initially loaded.

The moderator is a single tungsten crystal 0.08 inches thick and 0.12 inches in diameter with its surface along the (110) crystal plane. Two small holes were drilled through its side (taking care not to mar the crystal surface) with an EDM machine. It is mounted with the crystal surface perpendicular to the magnetic field lines via 0.07 mm diameter tungsten wires strung through the holes, connecting it to a molybdenum ring. The moderator is mounted in this fashion to allow it to be heated in thermal isolation from the rest of the trap via electron bombardment from the field emission point array. The field emission point array, described in more detail in Section 3.3, is mounted directly below the moderator. Naturally, great care was taken to align the loading tubes with each other, the moderator, and the thin titanium vacuum window.

2.3 Calculated positron flux on the moderator

The expected positron flux on the moderator is determined by the activity of the source, the fraction of positrons which successfully traverse the fringing magnetic field, and the fraction of these which make it through the small apertures in the

endcap electrodes. During most of the measurements reported here the source was at 10 mCi. Only 90% of the decays produce positrons, only half of which travel in the forward direction towards the source window. Factoring in the additional 50% self-absorption of forward-emitted positrons within the source capsule itself, this yields a total source activity $A = 8.3 \times 10^7$ positrons per second.

Fermi's theory of beta decay [28] gives the positron energy spectrum

$$\begin{aligned} N(\gamma) &= CF_+(Z,\gamma)\gamma(\gamma_e - \gamma)^2(\gamma^2-1)^{1/2} \\ F_+(Z,\gamma) &= \frac{-2\pi Z\alpha(1-\gamma^{-2})^{-1/2}}{1-\exp(2\pi Z\alpha(1-\gamma^{-2})^{-1/2})} \end{aligned} \tag{2.1}$$

where γ is the usual relativistic energy factor, $N(\gamma)$ is the differential probability that a positron has energy γ, C is a normalization constant, γ_e is the endpoint energy of the beta decay spectrum, Z is the atomic number of the final state, α is the fine structure constant, and $F_+(Z,\gamma)$ is the Fermi function for positive charges, which includes the effects of the Coulomb interaction between the positron and the nucleus. The source material, and the thin window which seals the source capsule, moderate and shift this energy spectrum slightly, but the effect is small enough to be unimportant for these calculations. (See for example Ref. [1] pages 21–25 and also Ref. [29].) The pressure in the magnet bore is kept below 10^{-6} Torr and therefore has no effect on the positrons.

The strong magnetic field controls the trajectory of the positrons so that they essentially travel along the field lines while executing cyclotron motion. The cyclotron motion radius is given (in S.I. units) by

$$r_c = \frac{mc}{eB}(\gamma^2-1)^{1/2}\sin\theta \tag{2.2}$$

where m is the positron mass, e the electric charge, c the speed of light, B the magnetic field strength, and the positron is emitted at angle θ with respect to the magnetic field lines. We use Eq. 2.1 and the assumption of isotropic emission

to calculate the expected distribution of cyclotron radii for a ^{22}Na source, shown in Fig. 2.11. We expect that positrons do not emerge exactly isotropically from the source capsule, since those emitted at large angles with respect to the magnetic field lines are preferentially absorbed within the capsule. This has the effect of reducing the large-radius tail of the distribution.

Because the cyclotron frequency

$$\nu_c = \frac{eB}{2\pi\gamma m} \tag{2.3}$$

is so rapid (ν_c = 165 GHz when B = 5.9 Tesla and $\gamma = 1$), the magnetic field which the positrons experience changes very little in the course of one cyclotron orbit, even at these relativistic energies. This makes calculation of the positron trajectories much easier insofar as the ratio of the cyclotron energy and magnetic field strength is an adiabatic invariant. Two important effects are noted. First, the active area of the positron beam—which initially has $r_s \simeq 1.0$ mm—shrinks by B_s/B_t, where $B_s = 1.9$ Tesla is the field strength at the source and $B_t = 5.9$ Tesla is the field strength at the trap. Second, kinetic energy in the positrons' cyclotron motion increases by a factor of B_t/B_s. This additional cyclotron energy must be taken out of their "axial" kinetic energy (*i.e.* parallel to the magnetic field lines). Positrons emitted at a forward angle greater than a "critical" angle, given by

$$\sin\theta_c = \sqrt{B_s/B_t}, \tag{2.4}$$

thus do not have sufficient axial energy to reach the moderator. They magnetically "bounce" off of the compressing magnetic field lines and return to the source. After this magnetic compression the total positron beam flux is reduced by a factor of $(1 - \cos\theta_c)$. The calculated distribution of cyclotron radii after magnetic compression is shown in Figure 2.11.

The final loss of positron flux occurs because the active area of the beam is larger than the effective aperture size in the endcap electrodes. The off-axis holes in the endcaps have radius $r_h = 0.5$ mm. Positrons with large cyclotron radii

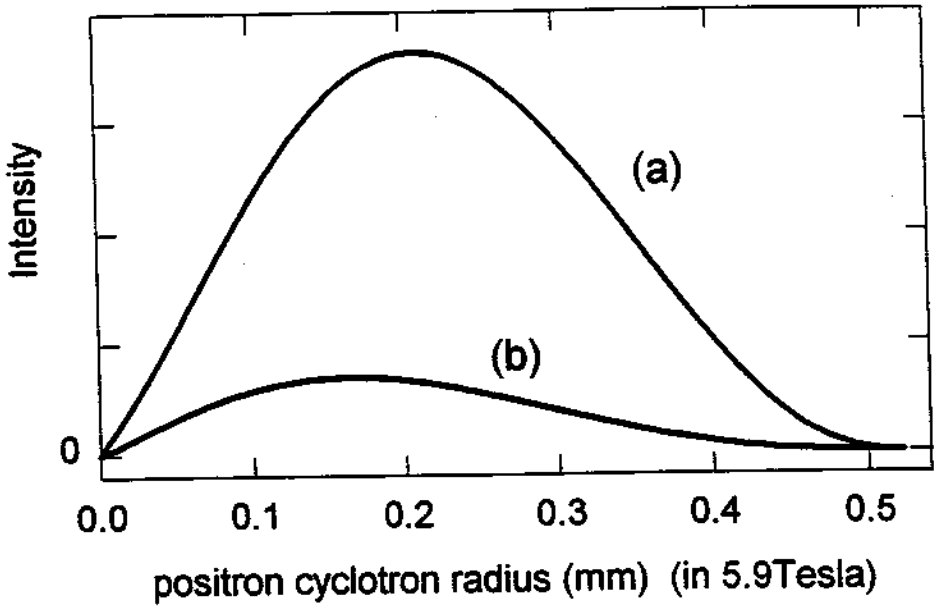

Figure 2.11: Sodium-22 positron cyclotron radii distribution in a $B_t = 5.9$ Tesla field, (a) without magnetic compression, area normalized to 1. (b) with magnetic compression after emission in $B_s = 1.9$ Tesla, area normalized to $(1 - \cos\theta_c)$.

traveling near the edges of the hole impact the sides of the aperture and are lost. The effective aperture radius for these energetic positrons is therefore reduced by their average cyclotron radius from r_h to $r_e \approx 0.27$ mm, and the flux is reduced by a factor of

$$\frac{\text{Effective area of holes}}{\text{Active area of beam after magnetic compression}} = \frac{\pi r_e^2}{\pi r_s^2 (B_s/B_t)}. \tag{2.5}$$

Combining the factors of magnetic bouncing and beam collimation at the apertures yields a total expected flux on the moderator

$$F = A\frac{r_e^2}{r_s^2}\frac{B_t}{B_s}\left[1 - \sqrt{\left(1 - \frac{B_s}{B_t}\right)}\right] \approx 3 \times 10^6 \text{ e}^+/\text{s}. \tag{2.6}$$

The flux can be calculated more carefully by integrating the "effective aperture radius" over the distribution of cyclotron radii given in Fig. 2.11, and this gives nearly the same result as Eq. 2.6 using $r_e \approx 0.27$ mm.

2.4 Measuring the positron flux

The flux of positrons into the moderator given in Eq. 2.6 corresponds to a continuous electrical current of 480 fA. We were able to measure this by connecting the moderator directly to the small-current input of a lock-in amplifier and driving the mechanical beam shutter at 1 Hz. This is an important diagnostic tool because it allows us to test the apparatus alignment and to maximize the positron flux without relying on any knowledge of the moderator's condition or the trapping efficiency.

In order to average out the 1 Hz steps, and to obtain an accurate measurement with a signal greater than the Johnson noise, it was necessary to use a lock-in integration time constant of at least 10 seconds. It was also necessary to rotate the cam back and forth (between the "beam on" and "beam off" positions) many times, subtracting the values of neighboring measurements, to eliminate long-term drifts in the signal.

Another possible concern in this measurement was the slow, secondary electrons (typically of a few eV in energy) released when positrons impact a surface. Secondary electrons knocked free from the high vacuum side of the trap can's thin titanium window and from the entrance hole boundaries travel with the positrons to the moderator, where they cause a systematic underestimation of the positron flux. Conversely, electrons released from the moderator by the positrons' impact cause a systematic overestimation of the flux. To eliminate both these concerns, the bottom entrance tube was kept at −50 Volts during this procedure. This is sufficient to reflect most secondary electrons from *either* direction. (The tube bias was reversed once every minute—for one second—to drive out any charged particles which might have accumulated in the region.)

The lock-in amplifier routinely measured a difference of 120 ± 20 fA between the "beam on" and "beam off" cam positions. Unfortunately, we do not know the exact shape of the input signal produced as the beam shutter chops the positron

beam. The lock-in amplifier operates by mixing the input signal (in this case, whatever lineshape is produced by the beam chopping) with a reference signal (in this case, a sine wave which was also used to drive the beam shutter) and gives the d.c. component. We tested the lock-in amplifier and found that when the reference input was given a sine wave and the input signal was a sine wave of the same frequency, the conversion factor from peak-to-peak to d.c. current was 0.33. When the input signal was a triangle wave, the conversion factor was 0.25. Therefore we conclude that the measured lock-in signal of 120 fA corresponds to a continuous positron beam current between 350 and 480 fA, which is consistent with the expectations outlined in Section 2.3.

Chapter 3

Positron emission from the moderator

Positron moderators have been developed and studied for more than a decade. They are now used to produce slow, nearly monoenergetic beams of positrons for a variety of applications in atomic and solid state physics. (There is a great deal of literature on this subject. For a review see Ref. [7].) Single crystals of various metals are generally the material of choice for positron moderators.

When a high energy positron from a radioactive decay impacts a solid, it rapidly thermalizes near the surface. The positron lifetime in a solid is typically several microseconds. During this time the positron diffuses randomly over many microns if the material is a well-ordered single crystal. Vacancies, impurities, and other defects in the crystal trap positrons and prevent further diffusion. Those positrons which diffuse to the crystal surface see a positive work-energy function ϕ_+ due to the lattice of positive ions, causing them to be ejected nearly monoenergetically if their thermal energy spread is small compared to ϕ_+ [7,30].

A high-quality moderator is critically important for slowing and trapping large numbers of positrons. The first important factor is that the the moderator efficiency η (the fraction of slow positrons emitted per fast incident positron) be as large as possible; the positron trapping rate is directly proportional to η. The

second factor is that ΔE, the spread of kinetic energies around ϕ_+ with which the positrons are emitted, be as small as possible. (We define ΔE as the spread of kinetic energies along a direction normal to the crystal surface, which in this case corresponds to kinetic energy *parallel* to the magnetic field lines. The positron kinetic energy which is *transverse* to the magnetic field lines is in the form of cyclotron motion and is unimportant for our calculations.) The trapping rate is typically inversely proportional to ΔE, as explained in Chapter 4. It is worth noting that, for all moderators, some fraction of the emitted positrons scatter off surface contaminations or quantum bound surface states; this tends to increase ΔE. Other positrons are ejected in the form of positronium, which reduces the measured efficiency η.

We use a single crystal tungsten (110) moderator because this material has been demonstrated to achieve efficiencies as high as $\eta \approx 10^{-3}$ and energy spreads as small as $\Delta E \leq 65$ meV at temperatures near 4 K [31,32,33]. Tungsten moderators are widely used and considered reliable and relatively easy to use [34,35]. One potential drawback is a measurement [36] indicating that their efficiency η drops dramatically when cooled to 4 K due to quantum reflections of positrons at the surface. However, earlier results [32,33] show a constant or increasing efficiency as the crystal temperature nears 4 K. The disparate results may be due to the different procedures used to prepare the crystal surfaces [34]. Fortunately, we can control the temperature of our crystal using a field emission point array (Section 3.3), allowing us to measure changes in η as a function of temperature and also to heat the crystal should quantum reflections become a problem.

We considered using a copper (111) crystal as a moderator. Copper has the advantage of a much lower annealing temperature compared to tungsten. Unfortunately, the annealing temperature is within 50 degrees of the melting temperature [34,35], requiring an accurate thermometer and a high degree of control over the electron beam heating current. The difficulties in thermometry and temperature control in our 4 K environment, combined with the difficulties of replacing a

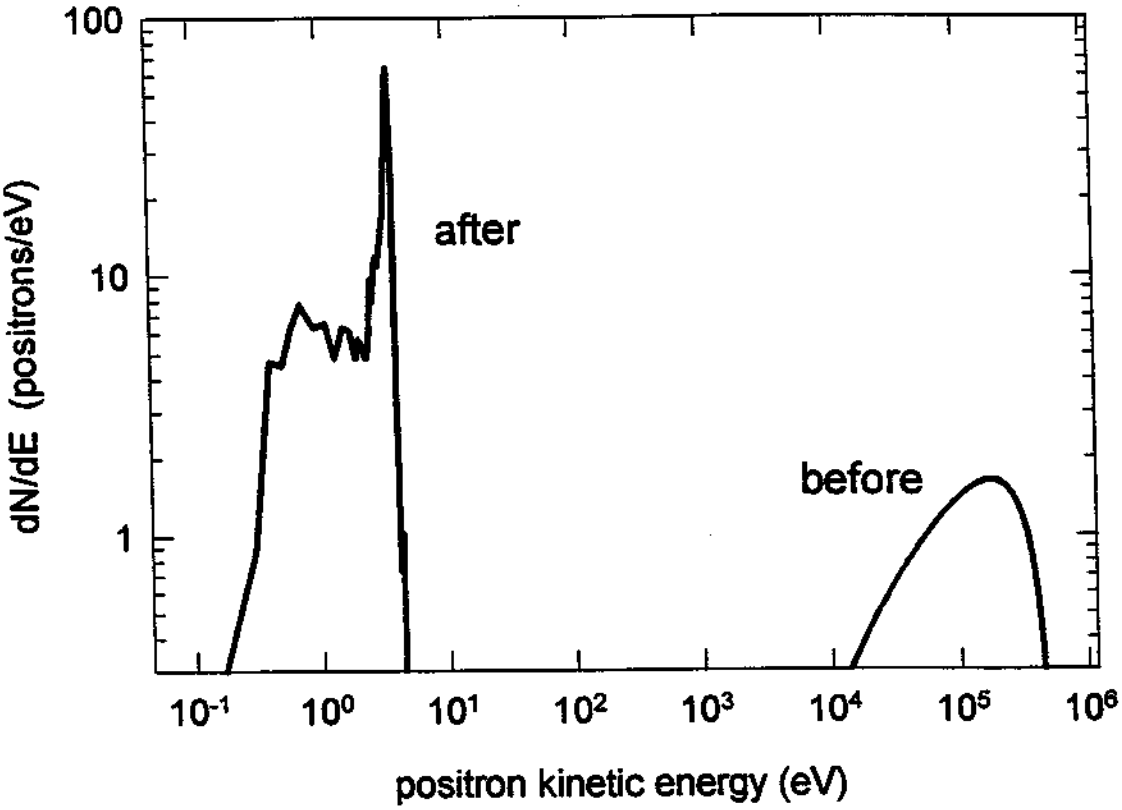

Figure 3.1: Energy distribution of positrons before and after moderation. The area of the "before" curve is normalized to 1. The "after" curve is for $\eta = 10^{-4}$.

crystal should it be damaged, made the tungsten moderator more attractive.

3.1 Positron energy spectrum before and after moderation

The advantages of using a positron moderator are illustrated in Fig. 3.1, which compares the energy distribution of positrons before moderation (as calculated from the Fermi decay theory for ^{22}Na) and after moderation (using the results of Section 3.4 and a conservatively assumed $\eta = 10^{-4}$.) While moderators decrease the number of positrons in the beam by a factor of η, they dramatically increase

the beam brightness dN/dE—that is, the number of positrons per eV of kinetic energy. The positron trapping rate is proportional to dN/dE.

3.2 Initial moderator treatment

We purchased three W (110) crystals from Goodfellows Corporation, each with a diameter of 0.12 inches and a width of 0.08 inches. In addition, each had small holes (less than 0.01 inches diameter) electron-beam drilled through the side. As shown in Fig. 3.2, thin tungsten wires (0.07 mm diameter) through these holes connect the crystal to a molybdenum ring. This mounting scheme—used inside the trap can and also when the crystal is annealed in a separate vacuum chamber—provides a high degree of thermal isolation and helps avoid contamination of the crystal from other materials since only tungsten wires contact the tungsten crystal.

We used three different crystals during the course of the measurements reported in this thesis. The first crystal we used was poorly prepared (described below) and did not function as a moderator. The second and third crystals were prepared more carefully; both moderated positrons with roughly equal efficiencies. (The data in Fig. 3.5 and 3.6 were taken with the second crystal, and the data in Fig. 3.7 with the third.) The second and third crystals were prepared in the following manner: First, their surfaces were mechanically polished for a few minutes with 1 μm Al_2O_3 grit suspended in distilled water on a silk polishing cloth (polishing grit and cloth purchased from Buehler Ltd.) to remove all surface features larger than 1 μm. (After polishing, fine scratches estimated to be slightly under 1 μm deep were visible under a microscope at 30 times magnification.) Next, they were electrochemically etched in a solution of 4–5 NaOH "PELLETEs" (total weight 0.8 grams) per 50 cc of water at a current density of 0.3 A/cm^2, which removes surface material at a rate of $\sim$ 18μm per minute. Care was taken to use only glass or stainless steel in the solution, and the solution was agitated by bubbling

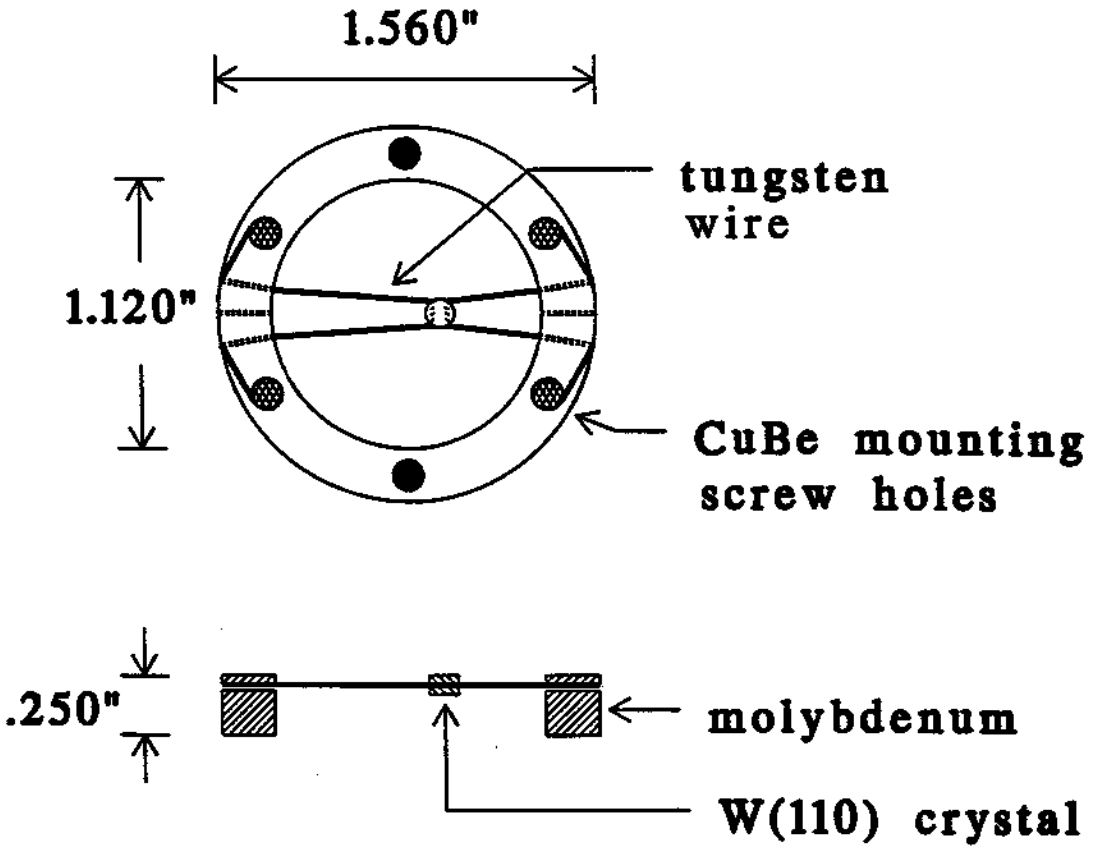

Figure 3.2: Top view and side view of tungsten crystal and mounting jig.

helium gas directly onto the crystal surface during etching. (This removed tiny bubbles which form on the crystal during etching and mar the surface.) An ethanol rinse left no noticeable residue. The second crystal, which had been etched for 12 minutes, had nine or ten "bumps" of an estimated 1 to 3 μm in size scattered over its surface. The third crystal, which had been etched for only 2 minutes, had only one such bump. In both cases, aside from the bumps, the surfaces appeared mirror-like under the microscope, almost uniformly smooth and without polishing scratches.

The crystals were then annealed for 1-2 hours at temperatures estimated in

excess of 2300 K—the second crystal in a vacuum of 4×10^{-7} Torr and the third crystal at 1×10^{-8} Torr. The crystals were heated by electron bombardment from a hot filament which supplied up to 40 mA of electron beam current. The filaments were 0.5 mm diameter thoriated tungsten wire heated by 0–6 Volts, 0–20 amps alternating current and radiated at about 100 Watts when delivering 40 mA beam current. The crystals were biased 1000 Volts positive with respect to the filament and appeared white hot throughout the annealing process. The uncertainty in the annealing temperature is ±200 K due to uncertainty in the crystal emissivity (between 0.1 and 0.2).

After annealing, the second and third crystals were held at 900 K in an atmosphere of 10^{-6} Torr oxygen for three hours. The purpose of this procedure is to remove interstitial carbon—which inevitably contaminates these crystals—from near the surface [34,35,37]. They were given one final heating to 2200 K in high vacuum, then brought up to atmosphere and immediately mounted in the trap can, which was then pumped to $\sim 10^{-7}$ Torr (for about 12 hours) and sealed via its pinch-off tube.

By contrast, the first crystal we installed—which had an efficiency η too low to be measured by our methods—was not etched electrochemically, and we relied upon the supplying company's mechanical polishing of the surface rather than our own. It was annealed for only a few seconds in the trap can at 10^{-6} Torr shortly before pinch-off without any treatment to remove interstitial carbon.

3.3 Heating the moderator "white hot" in a 4 K environment

When the moderator is transfered from the annealing chamber to the trap can, oxygen and other molecules inevitably contaminate the surface. This has two undesirable effects. First, contamination sites trap positrons, preventing re-emission

and lowering η. Second, emitted positrons scatter from these surface molecules. While elastic scattering at the surface does not change the positron's *total* kinetic energy, it preferentially transfers some of that energy from longitudinal (parallel with the magnetic field lines) into transverse (cyclotron) motion, which increases ΔE. It is desirable to clean the crystal's surface *after* it has been installed in the trap can. Once the surface is clean, the ultra-high vacuum in the trap can prevents the surface from being recontaminated.

Electron-bombardment heating is a common means for cleaning and annealing metal crystals. Usually, the electron source is a thoriated tungsten filament operated at up to 100 watts of power; however, it is not convenient to use such a filament in our trap can during normal operating conditions. The large heat load would boil off large amounts of liquid helium, and the local heating would probably raise the background pressure inside the sealed trap can to undesireable levels. There are the additional complicating factors of constructing a filament which can withstand the strong forces it would experience in the 5.9 Tesla magnetic field, and attaching lead wires from the filament to the magnet hat's vacuum feedthroughs which can handle the large current load without also increasing the thermal conduction load from the room temperature hat to the liquid helium dewar.

The Spindt-type field emission point array is an alternative electron beam source more compatible with our sealed, cryogenic environment. We mounted such an array directly underneath the moderator inside the trap can. These devices, produced by SRI International, consist of an array of $\sim 10,000$ field emission points of a type shown in Fig. 3.3 [38]. Field emission points do not generate much heat during operation and so they do not add to the overall heat load on the system. The arrays require only a few milliamps of input current so they do not require high-current leads and do not experience strong forces in the magnetic field. When the cathode is biased to -120 Volts with respect to the gate, the array produces more than 5 mA of electron beam current. These electrons follow the magnetic field lines and strike the moderator, which we biased 600 or 1200 volts positive

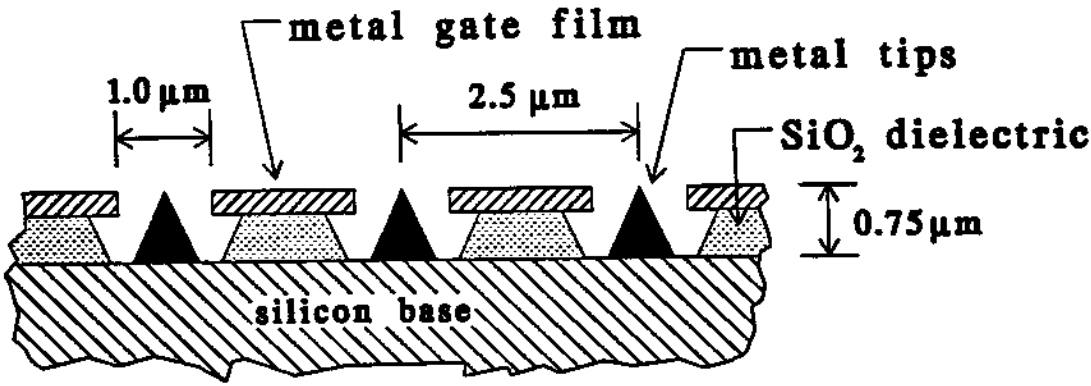

Figure 3.3: Cross section of Spindt-type field emission point array.

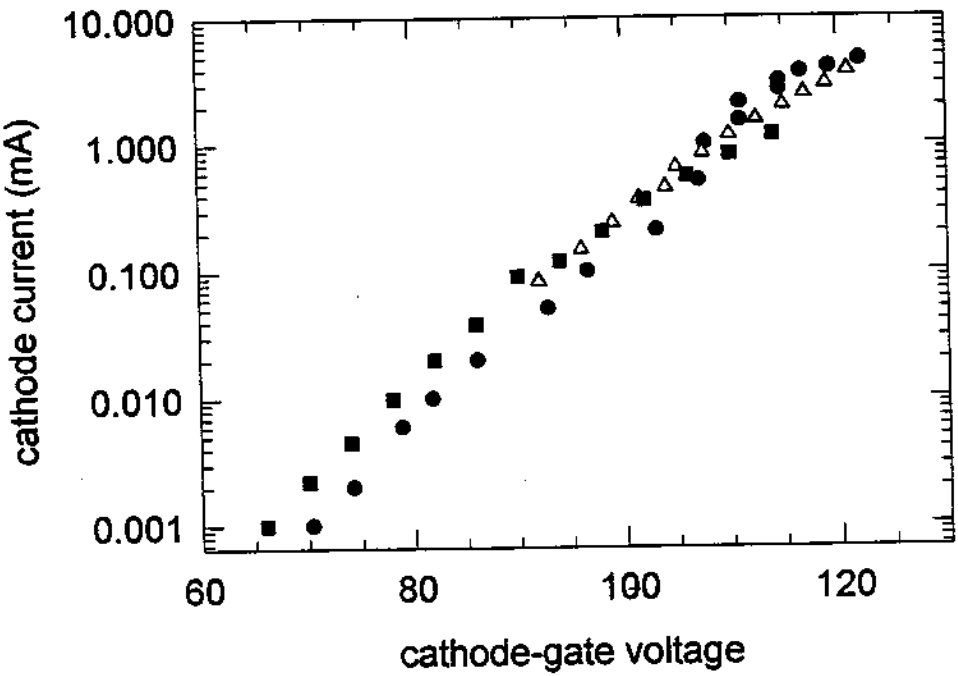

Figure 3.4: Typical voltage-current curve for a Spindt-type field emission point array. Data are shown for three separate runs.

with respect to the array. In this way, we heat the moderator to temperatures exceeding 2000 K for many minutes while the rest of the trap and the trap can walls remain cold, heat sunk to liquid helium, and under high vacuum. The effects of cleaning the crystal in this fashion are shown in the next section. It has been recommended [34] that, when we heat the crystal in this fashion, we cool it slowly ($\leq$ 100 degrees per minute) since rapid cooldown can quench vacancies into the crystal lattice.

Although the manufacturer of the field emission point arrays experiences long-term reliability with these devices when operating under high vacuum at room temperature, the arrays have proven to be less robust in our 5.9 Tesla, 4 K environment than we had initially hoped. Three of them failed during operation thus far. The first was lost when a bias of -200 Volts was mistakenly applied between the cathode and the gate. This caused an electric arc which permanently shorted the cathode to the gate, rendering the device unusable. We now regularly employ resistors in the gate- and cathode-biasing circuits to protect against sudden voltage or current surges. (10 kΩ for the gate, and from 5 kΩ to 2 MΩ for the cathode.) The second array was also destroyed by an electric arc between the cathode and the gate. In this case the device had been operating normally for nearly an hour and had just reached a cathode current of 1 mA when it failed. Since the cathode had operated at 1.6 mA for several minutes some weeks previously, the failure was unexpected. It may have been caused by a local pressure surge due to outgassing of the array as the cathode current increased [38].

In order to minimize this problem, the cathode current on the third array was increased extremely slowly—always keeping the cathode current low enough so that it did not fluctuate more than 1 to 2 percent, requiring at least two full days to increase the cathode current from 1 μA to 1 mA—to give the device plenty of time to outgas. (We believe that fluctuations in the cathode current are indicative of local pressure surges.) During this procedure, the moderator was biased only +50 Volts relative to the array to reduce the heat load on the system and to

reduce the energy with which ions could return to the array. Unfortunately, a new problem developed. The isolation resistance between the cathode and the gate, which initially was more than $10^{10}\Omega$, gradually decreased so that by the fourth day of use the isolation resistance had dropped to nearly $10^5\ \Omega$. Since it appeared at this point that the array would only be useable for a few more hours, we decided to increase the speed with which the cathode current was increased, hoping that the device had already outgassed sufficiently. Unfortunately, it experienced another electric arc (when it reached 1.1 mA) which destroyed the array. We are hopeful that the problem of isolation resistance degradation can be solved by "baking" the array clean before operation—either by increased baking of the trap and trap can under vacuum before it is sealed, or by heating the array *in situ* with a small resistive element while the trap can is sealed at 4 K.

3.4 Moderator performance

The process by which moderated positrons are loaded into the trap is described in Chapter 4; the procedure for counting the trapped positrons is described in Chapter 5. We use those results now to analyze the performance of our moderators.

Figure 3.5 shows the energy-analyzed positron trapping rate as a function of the bias potential applied to the moderator. (This data set was taken with our first working moderator—the second crystal we installed in the trap can.) Before the moderator was cleaned using the field emission point array, positrons emerged with a spread of (longitudinal) energies $\Delta E \approx 3$ eV. After the moderator was heated to ~1600 K for a few minutes and cooled, the energy distribution changed dramatically. The energy spread of the peak became $\Delta E \approx 700$ meV, with a low-energy tail of approximately twice the area of the peak. The loading rate at the peak increased while the overall yield η (propotional to the area under the peak) remained about the same. This result is consistent with moderator performance noted in the literature [31,39]. In particular, oxygen has been shown [37] to increase

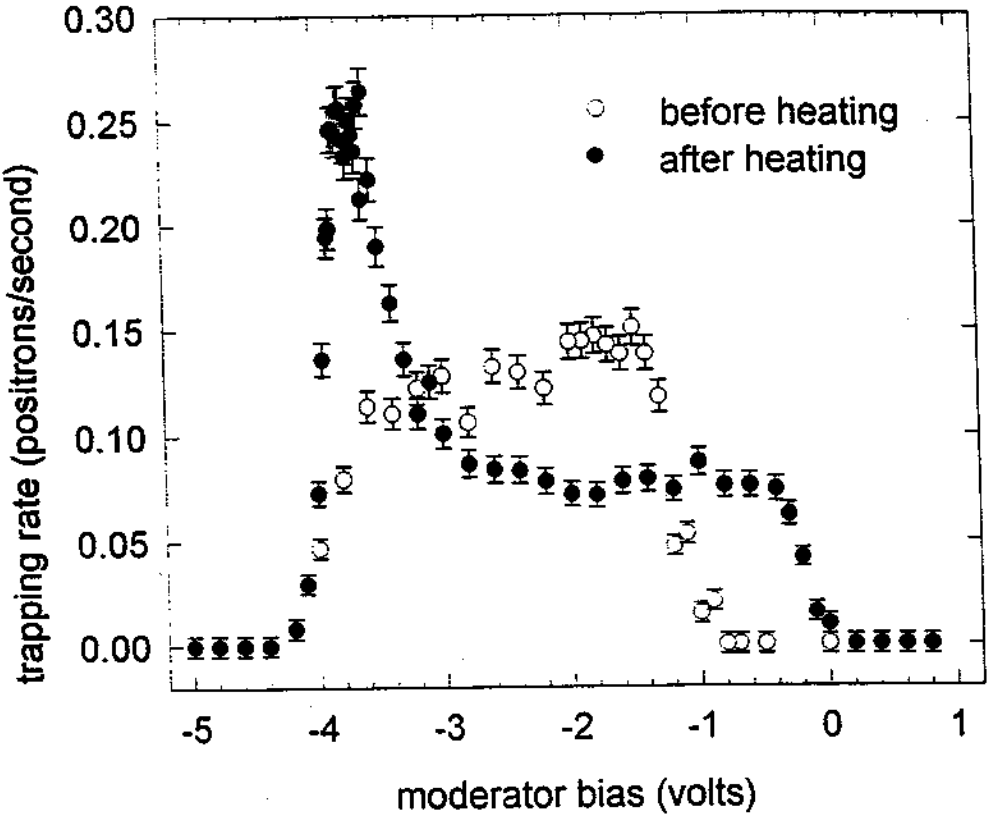

Figure 3.5: Positron loading rate measured before o and after • the moderator was cleaned by heating to $\sim$ 1600 K *in situ* for three minutes, while the rest of the trap remained cold and under high vacuum.

ΔE on tungsten moderators unless the crystals are cleaned by heating to at least 1600 K in vacuum.

A clean crystal surface can be recontaminated if the surrounding vacuum is inadequate. Monolayers of contaminants build over time, degrading moderator performance. However, this is not a problem inside our cryogenically cooled trap can. After the first cleaning cycle shown in Fig. 3.5, the moderator and trap remained cold (4 K) for six weeks while other measurements were made. At the end of those six weeks, no change was measured in either η or ΔE.

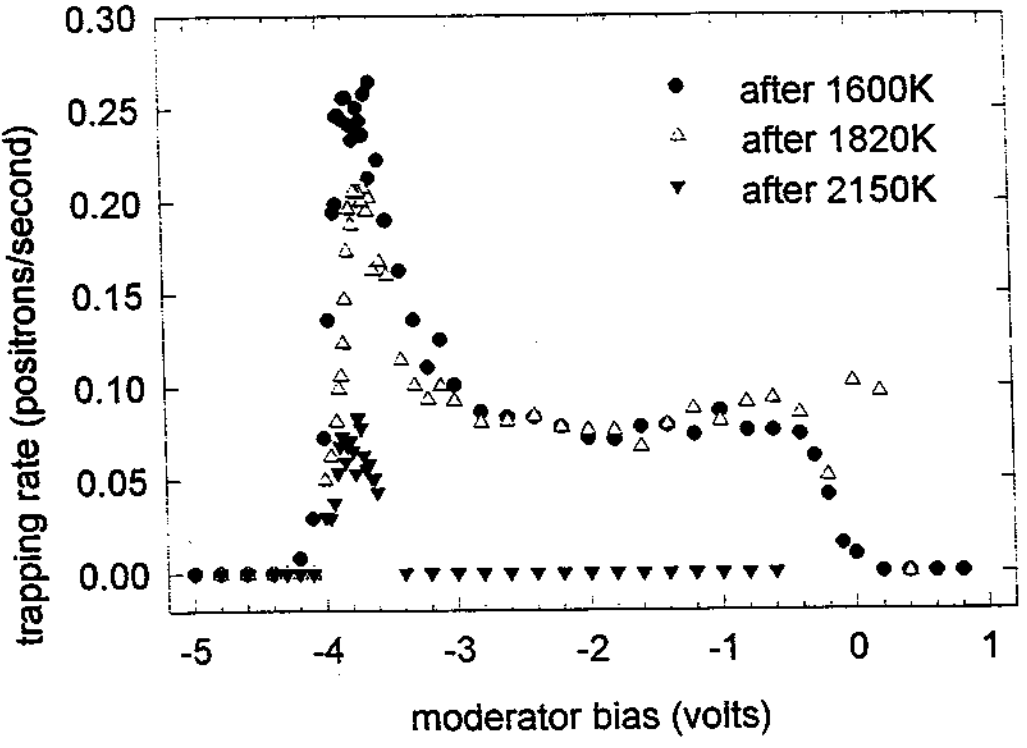

Figure 3.6: Moderator performance (a) after first heating cycle to 1600 K, (b) after second heating cycle to 1820 K, (c) after third heating cycle to 2150 K.

In an effort to improve the performance of this moderator, it was heated a second time, this time to ~1820 K. The results are shown in Fig. 3.6. Little change was noted. The moderator was heated a third time to ~2150 K, after which we experienced a field emission point array failure. This time there was a dramatic and unfortunate change in moderator performance. While the positron emission energy spread decreased to $\Delta E \approx 400$ meV, the overall yield η dropped dramatically. We believe this happened because the moderator cooled too quickly and allowed vacancies in the crystal surface to quench into place. Alternatively, interstitial carbon may have moved from the bulk of the crystal to near the surface. After the data set for Fig. 3.6 was taken, we replaced both the crystal and the

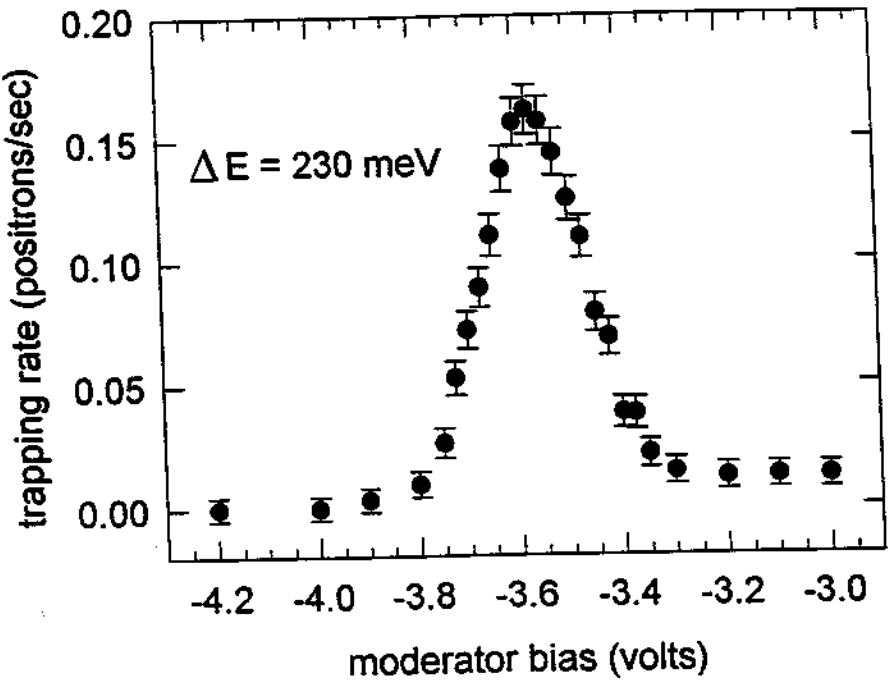

Figure 3.7: Narrowest positron energy distribution achieved to date.

array.

The positron energy distributions in Fig. 3.5 and 3.6 show a low-energy tail from the peak at ϕ_+ to ~ 0 Volts. (The reason the loading rate does not drop to zero precisely at 0 Volts is presumably due to contact potentials.) This is consistent with published moderator behavior [31,33,34,35,37,39], which always shows a low energy tail with an area of at least 50% of the area under the peak.

The third moderator crystal we used also had an initial positron energy spread of $\Delta E \approx 3$ eV before it was cleaned. After the first heating cycle it gave results very similar to Fig. 3.5. After several more heating cycles it produced the narrowest energy spread achieved to date, shown in Fig. 3.7, with $\Delta E = 230$ meV and a maximum loading rate of ~ 0.2 positrons per second. The third field emission point array failure occured after the heating cycle which produced Fig. 3.7. Further

moderator studies are planned, with hopes of achieving narrower energy spreads and higher positron trapping rates, with a new electron beam source.

3.5 Possibilities for improved moderator performance

There are several possibilities which might yield better moderator performance in future experiments [34,35,40]. New tungsten crystals could be purchased from a company which is better able to control the purity of their samples and better able to insure that the surface is cut precisely along the crystal plane. Initial annealing in a much improved vacuum ($< 10^{-9}$ Torr) might prevent contaminating molecules from imbedding in the crystal. There is, however, no published literature of which we are aware which demonstrates this to be a factor.

We have clearly shown that the efficiency of our moderators does not drop dramatically below 10^{-4} at 4 K, as had been suggested [36]. When we obtain a field emission point array or other electron beam source which can operate continuously in our environment, we will use it to heat the crystal continuously, while maintaining the trap electrodes at 4 K, to measure η and ΔE as a function of crystal temperature.

Chapter 4

Capturing slow positrons

Slow positrons emitted from the moderator travel back through the bottom entrance tube, following the strong magnetic field lines, and re-enter the trap through the small off-axis aperture in the bottom endcap electrode (see Fig. 2.10). However, they do not *remain* trapped unless they dissipate some energy while inside the trap volume. This chapter explains the details of how positrons lose sufficient energy to be captured in the Penning trap, and how four important bias voltages (the voltage applied to the ring electrode V_{ring}, the voltage applied to the compensation electrodes V_{comp}, the voltage applied to the moderator V_{mod}, and the voltage applied to the entrance tube V_{tube}) directly affect the loading rate R_L.

4.1 Penning trap dynamics

The dynamics of a charged particle (*e.g.* a positron) in a Penning trap are well understood, and are reviewed briefly here. (For a detailed review, see Ref. [22].) The equations in this chapter make use of the fact that the moderated positrons are no longer moving at relativistic energies.

A positron with mass m and charge e in a uniform magnetic field $\mathbf{B}$ moves circularly in the familiar cyclotron motion with a frequency given (in S.I. units)

by

$$2\pi\nu_c = \omega_c = \frac{eB}{m} \tag{4.1}$$

and a radius of

$$r_c = \frac{\sqrt{2E_c m}}{eB}, \tag{4.2}$$

where E_c is the energy in the cyclotron motion. The positron's cyclotron energy comes into thermal equilibrium with the walls of the trap at 4 K by synchrotron radiation damping. The Larmor formula (for example, see Ref. [41]) gives the damping rate for cyclotron motion as

$$\gamma_c = \frac{4r_0\omega_c^2}{3c} \tag{4.3}$$

where $r_0 \simeq 2.8 \times 10^{-13}$ cm is the classical electron radius and c is the speed of light. In 5.9 Tesla the cyclotron frequency $\nu_c \simeq 165$ GHz and $\gamma_c^{-1} \simeq 8 \times 10^{-2}$ sec. Thus, the positron's cyclotron energy after leaving the moderator equilibrates to 4 K in just a few seconds.

The positron's "axial" motion (parallel to the magnetic field lines) is governed by the electrostatic potential produced by the Penning trap electrodes. Figure 4.1 shows an idealized picture of the trap electrodes, along with the electric and magnetic field lines. The endcap and ring electrodes are machined along hyperbola of revolution

$$z^2 = z_0^2 + \rho^2/2 \tag{4.4}$$

and

$$\rho^2 = \rho_0^2 + 2z^2 \tag{4.5}$$

respectively, where ρ_0 and z_0 are the minimum radial and axial distances from the center of the trap to the electrodes. This configuration produces a nearly uniform quadrupole electric potential of the form

$$V(\rho, z) = V_0 \frac{z^2 - \rho^2/2}{2d^2} \tag{4.6}$$

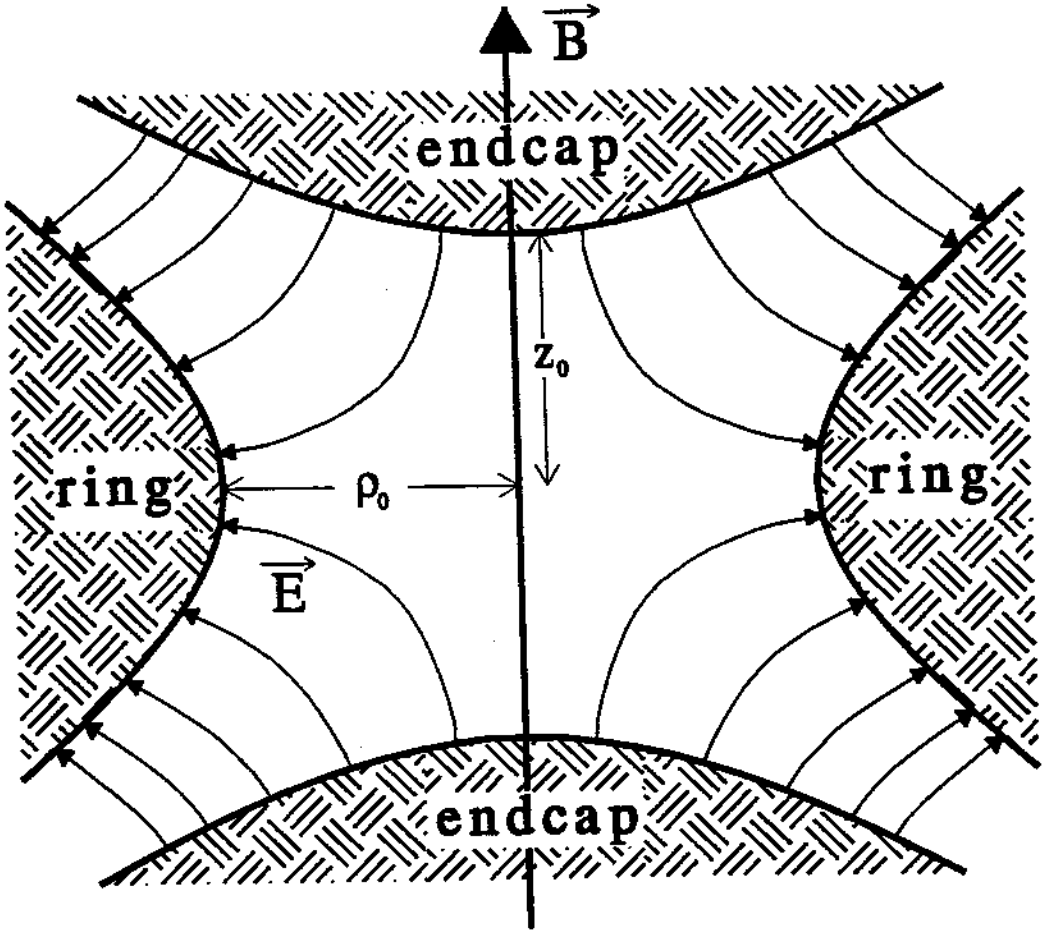

Figure 4.1: Electric and magnetic fields inside a Penning trap.

where V_0 is the voltage applied between the ring and endcaps, and the characteristic trap dimension d is defined by

$$2d^2 = z_0^2 + \rho_0^2/2. \tag{4.7}$$

In practice, machining uncertainties and the truncation of the electrodes cause the electrostatic potential to depart slightly from a pure quadrupole. The voltage applied to the compensation electrodes V_{comp} (see Fig. 2.10) allows us to adjust the electric potential to more closely resemble a pure quadrupole [42], a procedure which is often necessary when performing precision measurements on small clouds

of trapped particles. The trap used in this experiment has $\rho_0 = 0.168$ inches and $z_0 = 0.144$ inches. This ratio of ρ_0/z_0 was chosen to "orthogonalize" the trap electrodes [26,43]. In an "orthogonalized" Penning trap, adjustments in $V_{\rm comp}$ cause little or no shift in ν_z, the frequency of the particle's axial motion, for particles near the center of the trap.

The motional coupling between a positron's cyclotron and axial motion is inconsequential in these traps. Axial motion in the quadrupole electrostatic potential is simple harmonic motion with frequency given by

$$\omega_z^2 = \frac{eV_0}{md^2}. \tag{4.8}$$

The potential between the endcap and ring electrodes is typically $V_0 \simeq 12$ Volts, which gives an axial frequency $\nu_z \approx 69$ MHz. The radiative damping time is too long to be of consequence, so the axial motion is undamped unless it is coupled to a resistive circuit, as described in Section 4.3 and Section 5.1.

The third motion in a Penning trap is typically referred to as "magnetron" motion, and it is caused by the combined magnetic field $\mathbf{B}$ and the radial part of the quadrupole electric field, $\mathbf{E_{rad}}$. The details of the motion are derived elsewhere (see Ref. [22]). Magnetron motion can essentially be thought of as an $\mathbf{E} \times \mathbf{B}$ drift with constant velocity $\mathbf{v} = c\mathbf{E} \times \mathbf{B}/B^2$. Since $|\mathbf{E_{rad}}|$ is proportional to ρ, the magnetron drift has a constant frequency

$$\nu_m = \frac{\nu_z^2}{2\nu_c} \tag{4.9}$$

for all ρ. Assuming $\nu_c = 165$ GHz and $\nu_z = 69$ MHz gives $\nu_m = 14.4$ kHz. The magnetron motion is energetically unstable; that is, as the positron loses magnetron energy, its radius of orbit ρ_{mag} increases. However, the radiative damping time is extremely long ($\gamma_m^{-1} \simeq 3 \times 10^{14}$ sec) and ρ_{mag} can be reduced by applying appropriate radio frequency fields (Section 5.3).

The three motions are pictured in Fig. 4.2. The motions are separable in an ideal quadrupole potential aligned with a uniform magnetic field. Even in a not-

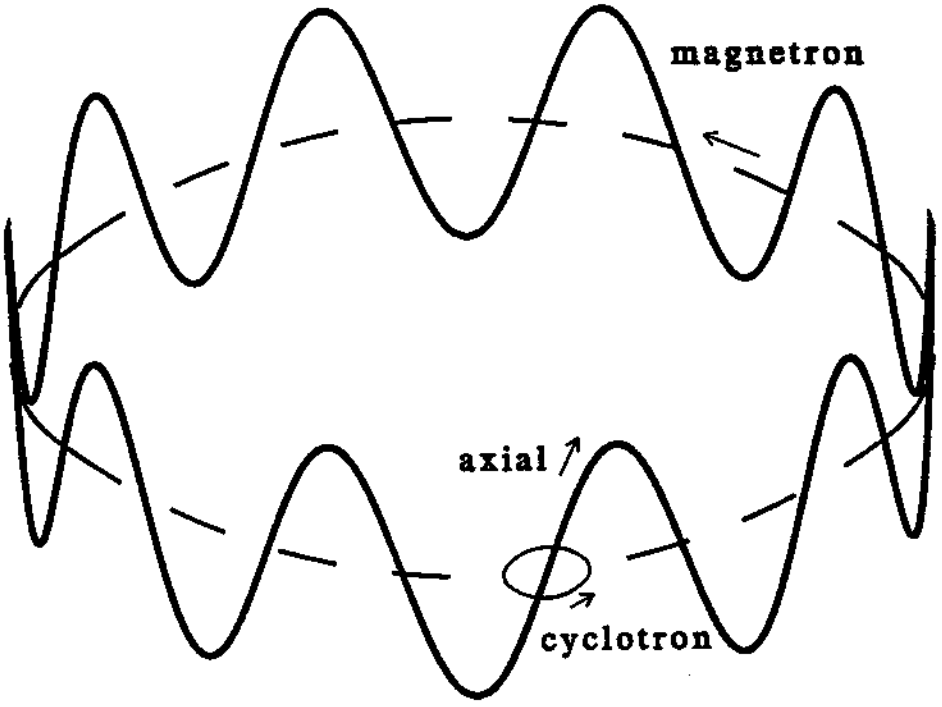

Figure 4.2: Motions of a positron in a Penning trap. The dashed circle is the slow magnetron motion. The solid line shows the axial motion superimposed. The cyclotron motion is much faster with typically a much smaller radius of motion.

quite-ideal trap such as this, the motions can be treated independently for all our calculations.

4.2 Electrostatic potentials in the entrance tubes

The shape of the electrostatic potential in the endcap's off-axis aperture is important for calculating the expected positron loading rate (Section 4.4). A close-up of the area around the off-axis aperture in the bottom endcap is shown in Fig. 4.3. The hole in the endcap has a radius of $r_h = 0.5$ mm and is centered $\rho_h = 0.140$ inches from the central symmetry axis of the trap. The copper entrance

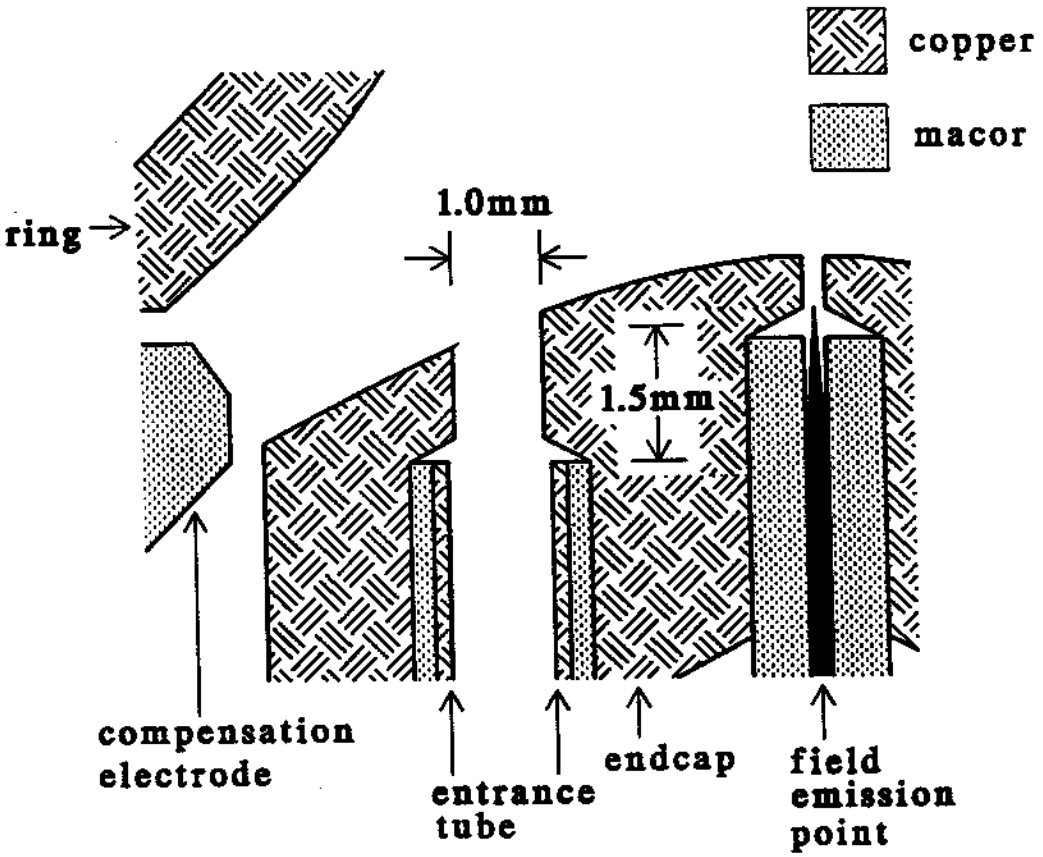

Figure 4.3: The off-axis aperture and entrance tube in the bottom endcap electrode.

tube has a radius $r_{\text{tube}} = 0.7$ mm, and is designed to terminate at a distance of $z'_{\text{tube}} = 1.5$ mm from the point where the center of the entrance aperture intersects with the hyperbolic surface defined by the endcap electrode. (Throughout this chapter, z signifies the (axial) distance from the center of the Penning trap and z' signifies the (axial) distance from the intersection point of the tube's central axial with the bottom endcap electrode surface.)

For positron trapping, the endcaps are grounded, $V_{\text{ring}} \simeq -12$ Volts, and a large negative potential is applied to the bottom entrance tube ($V_{\text{tube}} \simeq -100$ Volts).

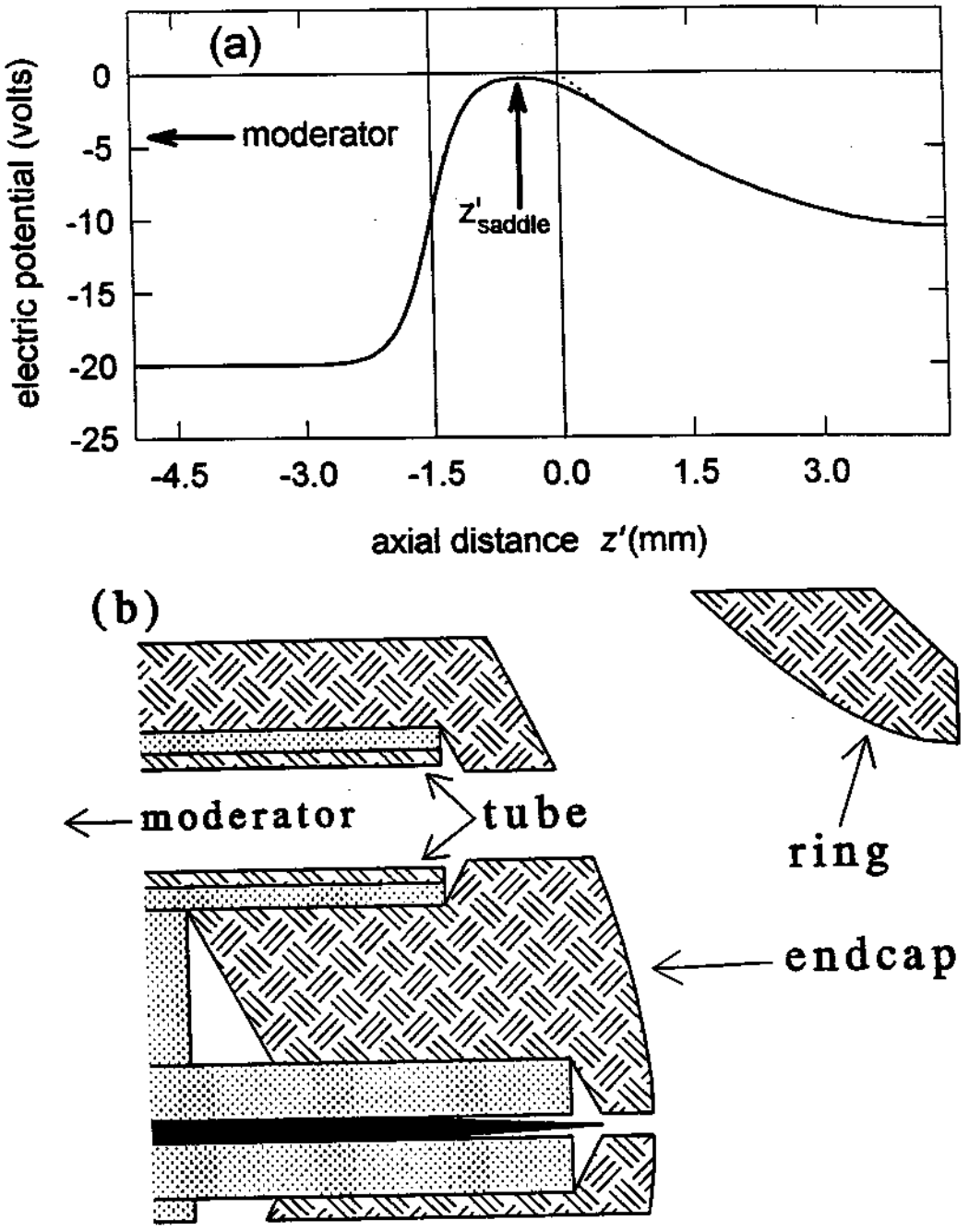

Figure 4.4: (a) Electric potential along the central axis of the loading tube. In this case, $V_{\text{tube}} = -20$ V and $V_{\text{ring}} = -12$ V with the endcaps grounded. The electric potential inside the trap volume ($z' > 0$) is essentially quadratic (dotted line) except in the region near the entrance hole. (b) Corresponding electrode surfaces. The end of the loading tube is located $z'_{\text{tube}} = 1.5$ mm from the hyperbolic surface of the endcap electrode at $\rho = \rho_h$.

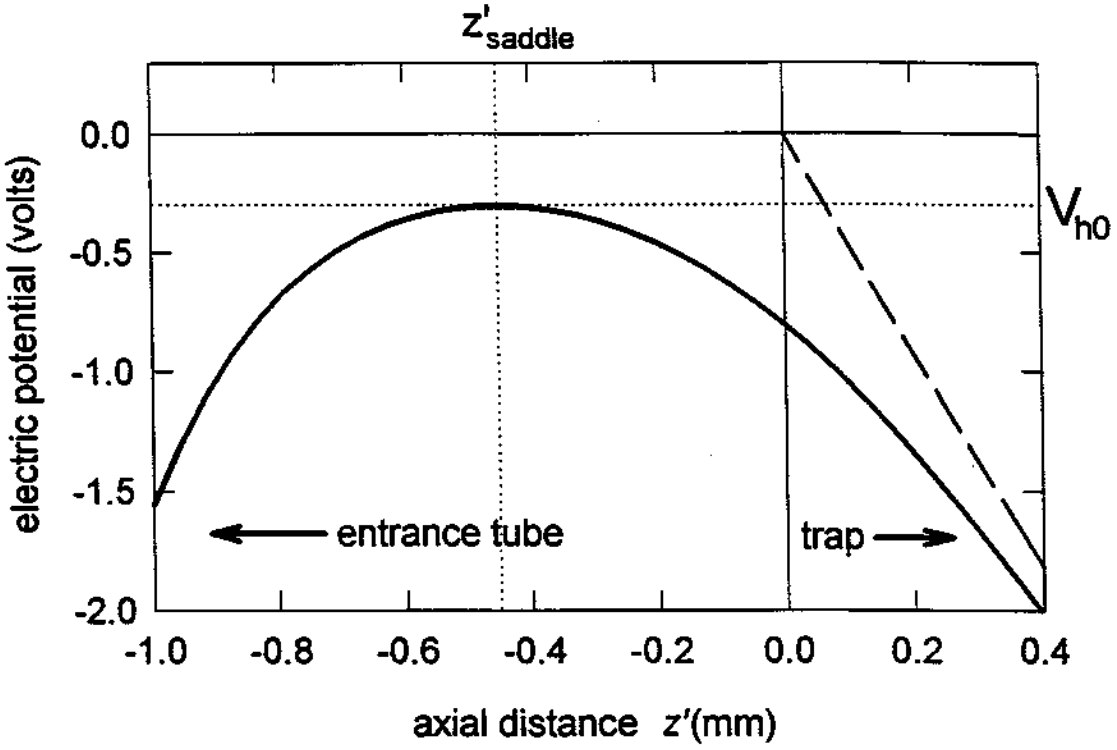

Figure 4.5: Close-up view of electric potential (dark line), as calculated by relaxation technique, along the central axis of the loading tube in the region of the saddle point. V_{h0} and $z'_{\mathbf{saddle}}$ are shown. The dashed line shows a pure quadrupole potential inside the trap ($z' > 0$).

We calculated the electrostatic potential in the region near the entrance aperture in the bottom endcap in two different ways which gave nearly identical results: (1) using a relaxation technique to solve Laplace's equation numerically; (2) solving analytically in three separate regions (inside the trap volume where $z' > 0$. inside the loading tube volume where $z' < -1.5$ mm, and between the tube and trap entrance where -1.5 mm $\leq z' \leq 0$) and matching boundary conditions. The results of these calculations are shown in Figures 4.4 – 4.6. Within the 1.5 mm region *between* the entrance tube and the trap, where the walls of the entrance hole

are grounded, the electric potential $V_h(r, z')$ is best described by a saddle point of the form [1,9]

$$V_h(r, z') = V_{h0}\left(\frac{r_h^2 - r^2 + 2(z' - z'_{\text{saddle}})^2}{r_h^2}\right) \tag{4.10}$$

where $r_h = 0.5$ mm is the radius of the hole, r is the radial distance from the tube's center axis, z'_{saddle} is the (axial) location of the saddle point, and V_{h0} is the potential at the saddle point. Note that $V_{h0} < 0$. The exact values of V_{h0} and z'_{saddle} are given by the calculations and depend upon V_{ring}, V_{tube}, r_{tube}, z'_{tube}, and the electrode geometry. Figure 4.5 shows a close-up of the electrostatic potential along the central axis of the loading tube in the region of the saddle point for the conditions of Fig. 4.4. (The potential departs somewhat from the form of Eq. 4.10 for $z' \neq z'_{\text{saddle}}$ and $r \approx r_h$, but this is not important for our calculations.)

Slow positrons traveling from the moderator (from the left in Fig. 4.4) experience a potential hill at $z' = z'_{\text{saddle}}$. The maximum value of the potential they experience is between V_{h0} and 0, depending upon their radial location r in the tube. Figure 4.6 shows a radial cross-section of $V_h(r, z')$ at $z' = z'_{\text{saddle}}$.

4.3 Damping the axial motion

Once positrons have traveled past the saddle potential and entered the trap, their axial motion can be damped. A positron's axial motion inside the trap induces image charges in the endcap electrodes which oscillate at ν_z. The ring electrode, compensation electrodes, and bottom endcap electrode are all shorted to ground at ν_z through capacitors. The upper endcap, however, is connected to ground through an inductor L which also has a small series loss resistance. On resonance for the LRC circuit, this resistance can be represented as a large parallel resistance R, as shown in Fig. 4.7. The endcap electrode itself contributes to the total capacitance of the circuit. The positron's axial motion causes an oscillating current I to flow

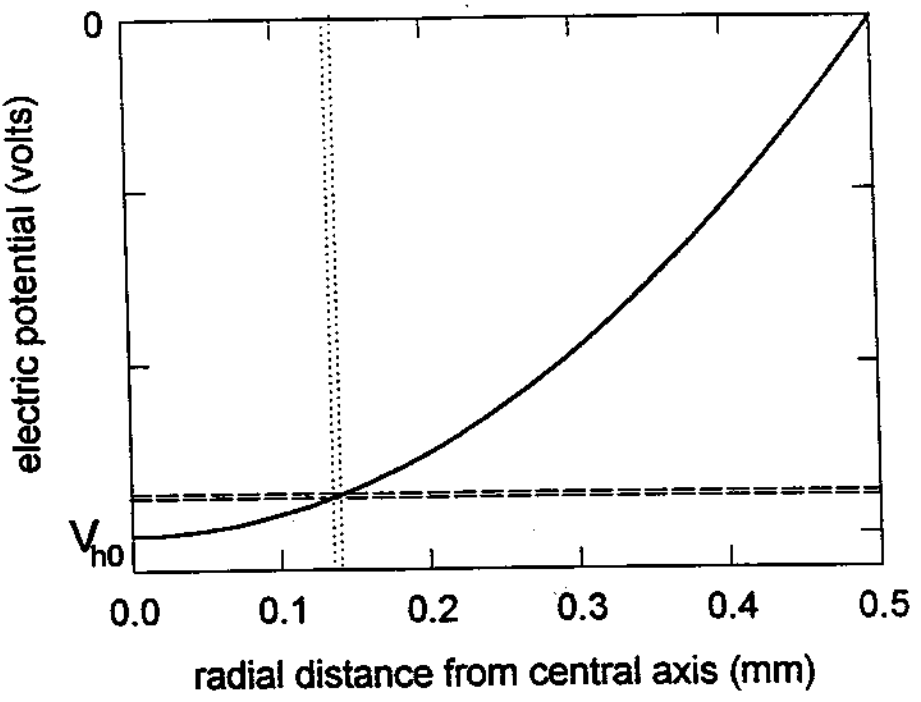

Figure 4.6: The electric potential $V_h(r, z' = z'_{\text{saddle}})$ near the saddle point, as calculated by numerical relaxation (solid curve), is essentially a quadratic function of r. The central axis of the entrance hole corresponds to $r = 0$ and the hole radius is $r_h = 0.5$ mm. The dotted lines are a distance δ_{mag} apart, showing the distance the positron drifts radially during its first axial orbit in the trap. The dashed lines show the corresponding "energy window," which determines the fraction of positrons which "survive" their first axial orbit and remain trapped for a complete magnetron orbit.

through L and R. When V_{ring} and V_{comp} are adjusted so that

$$\omega_z = \omega_{LC} \equiv \sqrt{1/LC}, \tag{4.11}$$

the axial motion is damped at a rate given by [44,45]

$$\gamma_z = \left(\frac{e\kappa}{2z_0}\right)^2 \frac{R}{m}, \tag{4.12}$$

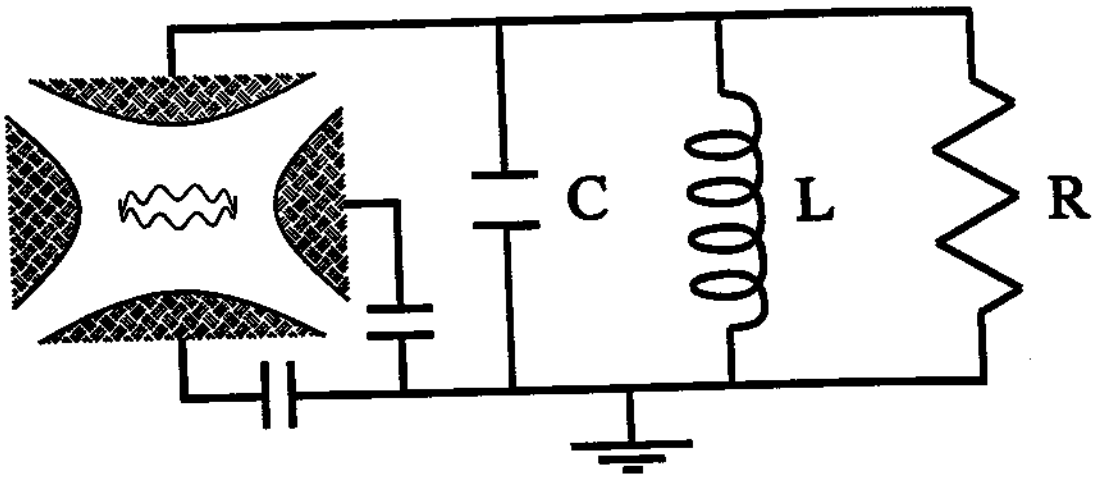

Figure 4.7: Idealization of the circuit connected to the upper endcap. The bottom endcap and ring electrode are shorted to ground at ω_{LC} through large capacitors. The positron's motion induces oscillating current in the resistor, where the energy is dissipated.

where κ is a dimensionless constant of order unity which depends upon the geometry of the trap electrodes. For this trap, $\kappa \simeq 0.8$ has been calculated [26]. We can rewrite Eq. 4.12 as

$$\gamma_z = \left(\frac{\kappa^2 \pi r_0 c}{z_0^2}\right) \frac{R}{\Omega_0} \tag{4.13}$$

where $r_0 = 2.8 \times 10^{-13}$ cm as before and

$$\Omega_0 = \frac{1}{\epsilon_0 c} \simeq 377\,\Omega \tag{4.14}$$

is the familiar "impedance of free space" [22].

A useful number when considering the damping circuit is its quality factor

$$Q = \frac{R}{\omega_{LC} L}. \tag{4.15}$$

The damping constant for a positron's axial motion γ_z scales linearly with Q. In this experiment we used an inductor with $L \simeq 0.27\mu$H. During most of the measurements reported here, $Q \simeq 1000$, with some data taken at $Q \simeq 750$. A quality

factor of 1000 yields $\gamma_z/2\pi \simeq 6.3$ Hz. As we will see in Section 5.4, both γ_z and Q can be measured directly.

We can adjust $V_{\rm mod}$ so that the lowest-energy positrons in the energy spread ΔE have just enough energy to get over the saddle point, so that positrons enter the trap with a range of energies (kinetic plus potential) between V_{h0} and $V_{h0} + \Delta E$. Recall that $V_{h0} < 0$ and that the endcaps are grounded; thus, the moderated positrons do not have sufficient energy to hit the endcaps or escape out the (grounded) upper entrance tube. We also assume that $V_{\rm ring}$ and $V_{\rm comp}$ are adjusted so that the positron's axial motion is resonant with the damping circuit ($\nu_z = \nu_{LC}$).

During the positron's *first* axial orbit in the trap, before returning to the bottom entrance aperture, it loses energy to the damping circuit equal to

$$\delta E_1 = eV_{\rho_h}\frac{\gamma_z}{\nu_z}, \tag{4.16}$$

where V_{ρ_h} is the depth of the axial well at $\rho = \rho_h$. Using Eq. 4.4 and 4.6 we see that $V_{\rho_h} = 0.88V_0$ for this trap. Using the typical values of $V_0 = 12$ Volts, $\nu_z = 69$ MHz, and $\gamma_z/2\pi = 6$ Hz we get $\delta E_1 = 6\,\mu$eV. The fraction of positrons trapped by this mechanism is only $\delta E_1/\Delta E$, which is too small to be significant.

During their first axial orbit, however, positrons also drift laterally in their magnetron orbit [1] a distance

$$\delta_{\rm mag} = 2\pi\rho_{mag}\left(\frac{\nu_m}{\nu_z}\right) \simeq 5\,\mu{\rm m}, \tag{4.17}$$

where $\rho_{mag} = \rho_h = 0.14$ inches is the radius of the magnetron orbit. If $\delta_{\rm mag}$ were larger than the hole radius r_h, all of these positrons would return to the bottom endcap after their first axial orbit sufficiently far from the entrance hole that they would be unable to escape. Because $\delta_{\rm mag} < r_h$, most positrons *do* escape back down the bottom entrance tube after their first axial orbit, annihilating at the moderator; however, a fraction of positrons are captured because of the shape of the electrostatic potential near the saddle point. Recall from Eq. 4.10 and Fig. 4.6

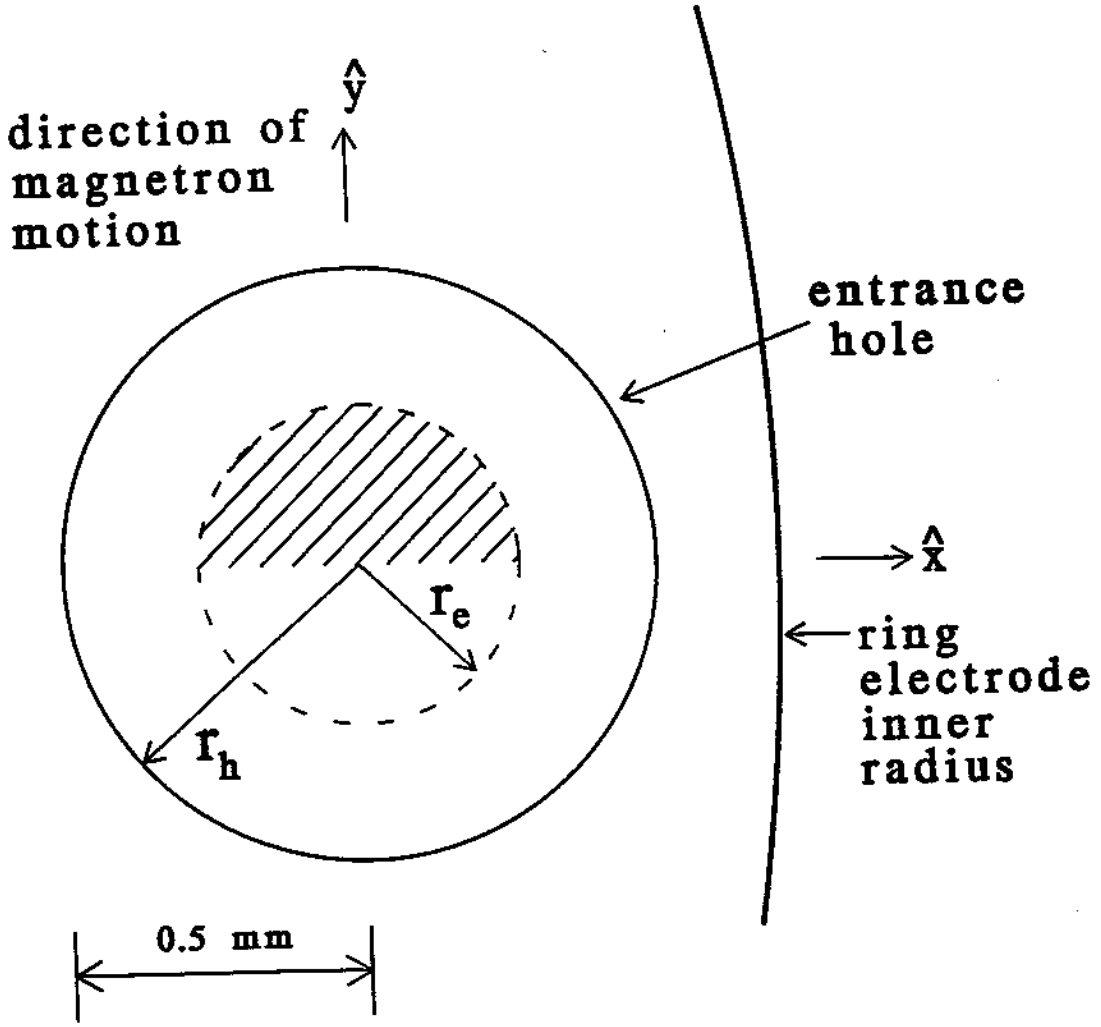

Figure 4.8: Cross-section of the off-axis entrance hole in the bottom endcap showing the active area (shaded region) over which positrons can "survive" their first axial orbit due to magnetron drift and remain in the trap. Note that the positron beam radius is shrunk from $r_h = 0.5$ mm to $r_e \simeq 0.27$ mm due to the average cyclotron radius of the unmoderated positrons, as described in Chapter 2.

that the saddle point of the electric potential is along the entrance tube's central axis. Therefore, if the positron's magnetron drift carries it *away* from the entrance tube's central axis, as shown in Fig. 4.8, the positron essentially "climbs a potential hill." Positrons which fall inside of a narrow energy window, pictured in Fig. 4.6, have insufficient energy to overcome this potential barrier and therefore remain

in the trap after their first axial orbit, for at least one complete magnetron orbit. The fraction of positrons so captured is calculated in Section 4.4. During this first magnetron orbit in the trap the positrons lose axial energy to the damping circuit of

$$\delta E = eV_{\rho_h}\frac{\gamma_z}{\nu_m} \simeq 28\,\mathrm{meV}. \tag{4.18}$$

This is now a significant fraction of ΔE.

4.4 Calculating the expected loading rate

Positron loading into the trap is understood in two nearly independent steps. First, we calculate the fraction of positrons which remain in the trap after their first axial orbit due to magnetron drift. Second, we calculate the total fraction which dissipate sufficient energy to remain in the trap when they return to the entrance tube after their first magnetron orbit.

Consider the x-y plane of the entrance tube at $z' = z'_{\mathrm{saddle}}$. We can rewrite Eq. 4.10 as

$$V_h(x, y, z' = z'_{\mathrm{saddle}}) = V_{h0}\left(\frac{r_h^2 - x^2 - y^2}{r_h^2}\right) \tag{4.19}$$

where (x, y) are defined relative to the entrance hole's central axis and $x^2 + y^2 \leq r_h^2$. Positrons enter the trap with a range of possible (x_i, y_i) such that $x_i^2 + y_i^2 \leq r_e^2$. (Recall from Chapter 2 that r_e, the effective radius of the positron beam when it hits the moderator, is less than r_h due to the cyclotron radius of the unmoderated positrons.) To simplify the following calculations, we assume that positrons enter the trap uniformly over an active area πr_e^2. We also make the simplifying assumption that the positron energies are distributed uniformly over ΔE. which is good for broad energy distributions ($\Delta E > \delta E$).

We define ϵ as the fraction of slow (moderated) positrons which are permanently trapped. A positron entering the trap at $(x_i, y_i, z'_{\mathrm{saddle}})$ magnetron drifts

in its first axial orbit and return to the position $(x_i, y_i + \delta_{\rm mag}, z'_{\rm saddle})$, where we have arbitrarily chosen the entrance tube to be in the $\hat{x}$ direction from the trap's central symmetry axis so that the initial magnetron drift is in the $\hat{y}$ direction. For each (x, y) the fraction of positrons which remain trapped after their first axial orbit is the difference in the potential energy of the positron before and after the first axial orbit, divided by the initial energy spread [9],

$$\epsilon_{init}(y) = \frac{eV_h(x, y+\delta_{\rm mag}) - eV_h(x,y)}{\Delta E} \approx \frac{2e|V_{h0}|\,\delta_{\rm mag} y}{r_h^2 \Delta E} \tag{4.20}$$

for $y > 0$, with no positrons trapped in the $y < 0$ region. We can integrate over $(x^2 + y^2) \leq r_e^2$ to obtain

$$\epsilon_{init} = \frac{4 r_e \delta_{\rm mag} e|V_{h0}|}{3\pi r_h^2 \Delta E}. \tag{4.21}$$

A positron which enters the trap at $(x_i, y_i, z' = z'_{\rm saddle})$ and remains in the trap after its first axial orbit will, after one magnetron orbit, return to the entrance tube having lost $\delta E \approx 28$ meV of axial energy to the damping circuit. When it reaches the position $(x_i, y = 0, z' = z'_{\rm saddle})$ it encounters a minimum in the electric potential along its trajectory. If the positron's initial kinetic-plus-potential energy upon entering the trap was δE *greater* than its potential energy at $(x_i, y = 0, z' = z'_{\rm saddle})$, it escapes down the entrance tube and is lost. Conversely, if the positron's initial kinetic-plus-potential energy was *less* than δE plus its potential energy at $(x_i, y = 0, z' = z'_{\rm saddle})$, it remains trapped. (Since the range of *kinetic* energies which are initially trapped is small—that is, $\Delta E \cdot \epsilon_{init}(y) \ll e|V_{h0}|$ in general—we can restrict our attention to the potential energies involved.) This restricts the "active area" for positron trapping to $0 \leq y_i \leq y_D$, where

$$y_D^2 = r_h^2 \left(\frac{\delta E}{|V_{h0}|} \right). \tag{4.22}$$

Positrons which enter the trap with $y_i > y_D$ do *not* remain in the trap after their first magnetron orbit because

$$V_h(x_i, y = y_i, z' = z'_{\rm saddle}) - V_h(x_i, y = 0, z' = z'_{\rm saddle}) > \delta E. \tag{4.23}$$

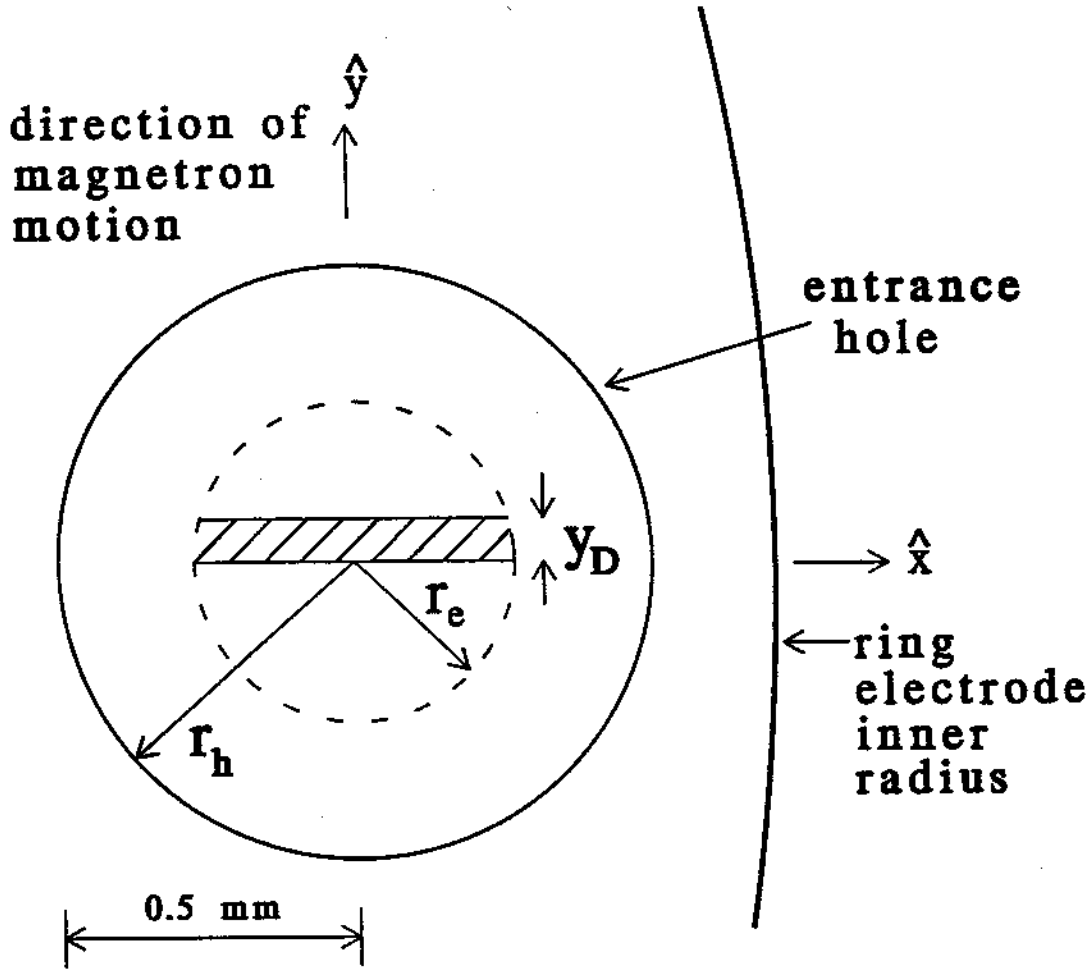

Figure 4.9: Cross-section of the entrance hole showing the active area over which positrons can be *permanently* loaded into the trap. The distance y_D is given by Eq. 4.22.

Figure 4.9 shows the active area over which positrons can enter and remain *permanently* trapped.

Once a positron has "survived" its first magnetron orbit, it continues to lose energy to the damping circuit until it comes into thermal equilibrium (at 4 K). After that, it should remain trapped indefinitely. Other possible mechanisms for positron loss from the trap are discussed in Section 6.2. We expect no loss of

positrons during a normal accumulation cycle.

If we assume that $\delta E < \Delta E$, which is the case for all the damping circuits and moderators we have used to date, we calculate the total trapping efficiency for moderated positrons, ϵ, by integrating Eq. 4.20 over the active trapping window, giving

$$\begin{aligned}
\epsilon &= \frac{4r_e\delta_{\rm mag}e|V_{h0}|}{3\pi r_h^2\Delta E}, && e|V_{h0}|(\tfrac{r_h^2}{r_e^2}) < \delta E < \Delta E; \\
&= \frac{2\delta_{\rm mag}\delta E}{\pi r_e\Delta E}, && \delta E < e|V_{h0}|(\tfrac{r_h^2}{r_e^2}) < \Delta E; \\
&= \frac{2r_h\delta_{\rm mag}\delta E}{\pi r_e^2\Delta E}\sqrt{\frac{\Delta E}{e|V_{h0}|}}, && \delta E < \Delta E < e|V_{h0}|(\tfrac{r_h^2}{r_e^2}).
\end{aligned} \tag{4.24}$$

When $|V_{h0}|$ is small (first condition of Eq. 4.24), $y_D > r_e$ and the active trapping window includes the entire shaded area of Fig. 4.8. For larger $|V_{h0}|$, we obtain the second condition of Eq. 4.24 and the active trapping window is the shaded region of Fig. 4.9. The third condition of Eq. 4.24 holds when

$$V_h(r = r_e, z' = z'_{\rm saddle}) - V_h(r = 0, z' = z'_{\rm saddle}) > \Delta E, \tag{4.25}$$

in which case the "trapping window" shown in Fig. 4.9 covers a region of potential energies larger than ΔE, which reduces the trapping efficiency.

The analysis of Eq. 4.24 is slightly modified when $\Delta E < \delta E$ with the result

$$\begin{aligned}
\epsilon &= \frac{4r_e\delta_{\rm mag}e|V_{h0}|}{3\pi r_h^2\Delta E}, && e|V_{h0}|(\tfrac{r_h^2}{r_e^2}) < \Delta E < \delta E; \\
&= \frac{2r_h\delta_{\rm mag}}{\pi r_e^2}\sqrt{\frac{\Delta E}{e|V_{h0}|}}, && \Delta E < e|V_{h0}|(\tfrac{r_h^2}{r_e^2}).
\end{aligned} \tag{4.26}$$

We can calculate ϵ more accurately by integrating Eq. 4.24 over the distribution of cyclotron radii shown in Fig. 2.11; however, this yields the same result as using $r_e \approx 0.27$ mm.

We can adjust $V_{\rm tube}$ to obtain the second condition of Eq. 4.24, which is optimal. Using $r_e = 0.27$ mm, Eqs. 4.17 and 4.18, and a measured $\Delta E = 230$ meV, we

estimate a capture efficiency $\epsilon \simeq 1.5 \times 10^{-3}$. If we can reduce ΔE to 65 meV, we will obtain $\epsilon \simeq 5 \times 10^{-3}$.

The expected positron loading rate R_L is the product of the (fast) positron flux on the moderator F, the moderator efficiency η, and the slow positron trapping efficiency ϵ (which is itself a function of of the moderated positrons' energy spread ΔE). Combining Eq. 2.6 and the second condition of Eq. 4.24 gives

$$R_L = \eta A \frac{B_t}{B_s}\left[1 - \sqrt{\left(1 - \frac{B_s}{B_t}\right)}\right]\left(\frac{2r_e\delta_{\mathrm{mag}}}{\pi r_s^2}\right)\left(\frac{\delta E}{\Delta E}\right), \tag{4.27}$$

where A is the source activity in positrons per second, and B_s and B_t are the magnetic fields at the source and trap, respectively. If $\eta = 1 \times 10^{-4}$ and $\Delta E = 230$ meV we expect a total loading rate of $R_L \approx$0.5 e^+/s. If $\eta = 1 \times 10^{-3}$ and $\Delta E = 65$ meV we expect $R_L \approx 15$ e^+/s.

There is a complicating factor which could reduce the loading rate from our calculated value. The axial motion damping term δE calculated in Eq. 4.18 and the trapping efficiency ϵ calculated in Eq. 4.24 are valid only when the positron's axial motion is harmonic (or very nearly so) and at a frequency matched to the frequency of the LRC damping circuit ($\nu_z = \nu_{LC}$.) The positron's axial motion should be harmonic (that is, the axial frequency is independent of the amplitude) so long as the electric potential it experiences $V(\rho, z)$ is purely quadrupole. Penning traps of this geometry (shown in Fig. 2.10) are known [26,43] to produce electrostatic potentials which are very nearly quadrupole in the center of the trap ($\rho \approx z \approx 0$). Near the electrode surfaces, however, the potential can depart significantly from the quadrupole form, primarily due to the truncation of the electrodes—although hyperbolically shaped electrodes cause less anharmonicity near the electrode surfaces than other possible geometries (*e.g.* cylindrical). The positron's first axial and magnetron orbits take place very near the edges of the trap ($\rho = \rho_h \approx \rho_0$ and $z_{\mathrm{max}} > z_0$), where any anharmonicities in the potential are the greatest. This decreases coupling between the large-amplitude axial motion and the damping circuit. Therefore, the actual damping term δE and loading rate

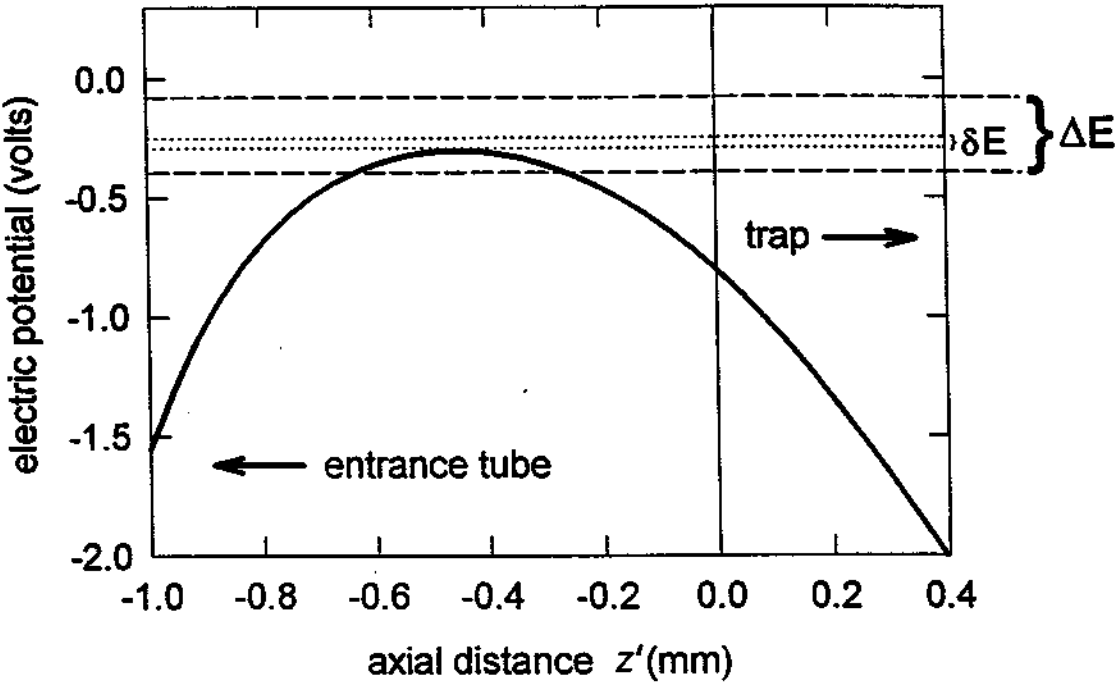

Figure 4.10: Energy window for trapping positrons along the entrance tube's central axis.

R_L may be somewhat lower than what we calculate in Eq. 4.27.

4.5 Measured loading rate

The calculations of previous section allow us to determine how the loading rate R_L should depend upon the four important bias voltages: V_{ring}, V_{comp}, V_{tube}, and V_{mod}. We now compare those expectations with our experimental results.

4.5.1 Loading rate dependence on tube and moderator bias

In order to trap positrons, V_{mod} must be adjusted to nearly cancel the kinetic energy with which positrons leave the moderator, ϕ_+. Ideally, V_{mod} is adjusted so that the spread of positron energies ΔE completely covers the "energy window" over which positrons can be trapped, which is between V_{h0} and $V_{h0} + \delta E$ for positrons entering along the tube's central axis, as shown in Fig. 4.10. When δE and $|eV_{h0}|$ are considerably less than ΔE, measuring the positron loading rate R_L as a function of V_{mod} allows us to sensitively measure the energy distribution of moderated positrons. There are several examples of R_L measured *vs.* V_{mod} in Chapter 3. All of those graphs were taken at a constant V_{tube}.

The loading rate depends upon V_{tube} only insofar as adjusting V_{tube} changes V_{h0}. As Eq. 4.24 shows, for small $|V_{h0}|$ we expect the loading rate R_L to increase linearly with $|V_{h0}|$; for large $|V_{h0}|$ the loading rate R_L should decrease slowly as $|V_{h0}|$ increases. Moreover, we expect that the value of V_{mod} which gives the maximum loading rate will shift with V_{tube} equal to the change in V_{h0}, since the loading rate is maximized when $\phi_+ + eV_{\text{mod}} = eV_{h0}$.

Figure 4.11 shows the measured loading rate *vs.* V_{mod} for nine different values of V_{tube}. As expected, the location of the V_{mod} peak shifts as V_{tube} is varied. By plotting the peak loading rates of Fig. 4.11 *vs.* V_{h0} (Fig. 4.12), we see exactly the dependence which we expect from Eq. 4.24. Note also from Fig. 4.11 that the apparent width of the positron energy distribution ΔE grows for large values of $|V_{h0}|$. This is because positrons are trapped whenever some portion of ΔE overlaps the "energy window" corresponding to the "active trapping window" shown in Fig. 4.9. When this "energy window" is greater than ΔE, we should expect the measured energy distribution to be broadened. We obtain an accurate measurement of ΔE only when $|V_{h0}| < \Delta E$.

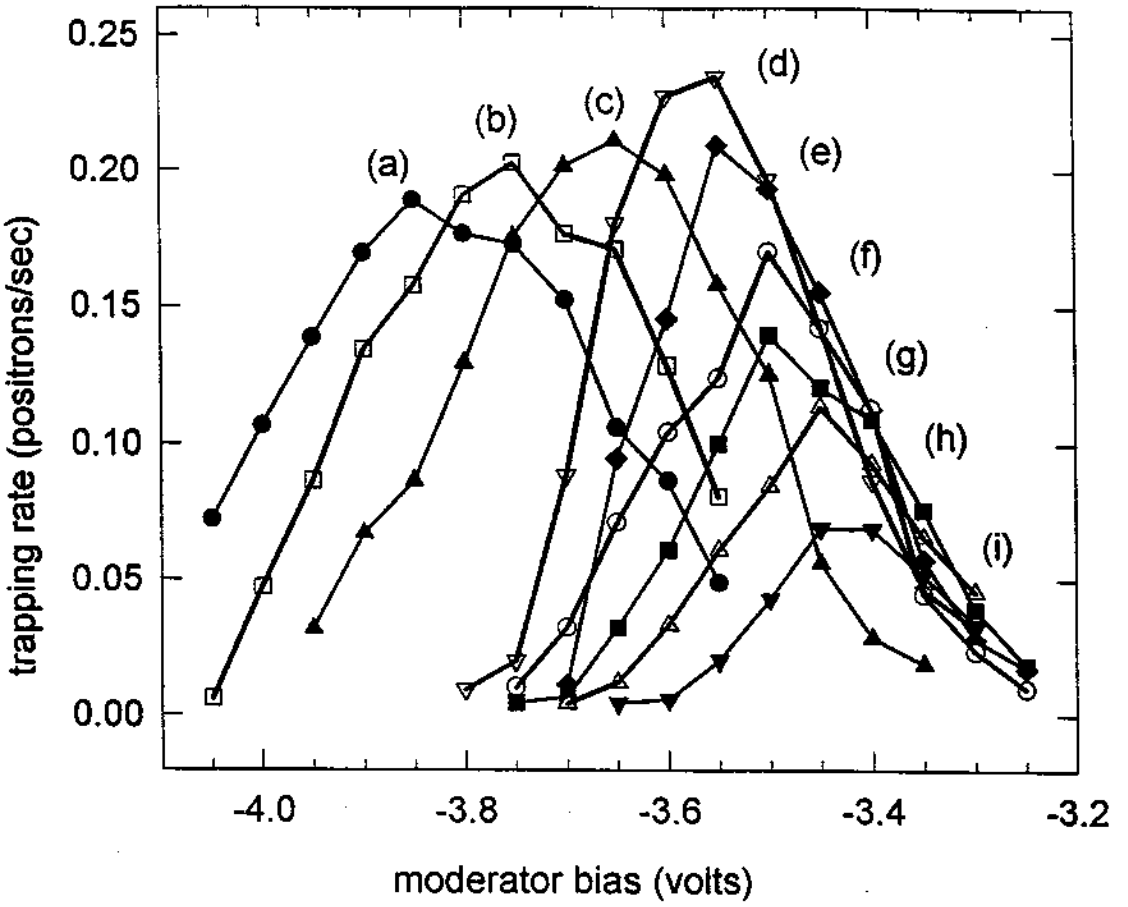

Figure 4.11: Positron trapping rate *vs.* moderator bias (using the moderator which gave the narrowest positron energy spread) for several different loading tube potentials. (a) V_{tube} = –250 Volts; (b) V_{tube} = –200 Volts: (c) V_{tube} = –150 Volts; (d) V_{tube} = –100 Volts; (e) V_{tube} = –60 Volts; (f) V_{tube} = –50 Volts; (g) V_{tube} = –40 Volts; (h) V_{tube} = –30 Volts; (i) V_{tube} = –20 Volts.

4.5.2 Loading rate dependence on ring and compensation bias

Adjusting V_{ring} causes the positron's axial frequency ω_z to shift an amount given by Eq. 4.8. As ω_z shifts away from ω_{LC}, the positron's axial motion is damped less effectively, causing the positron loading rate to decrease. This is demonstrated

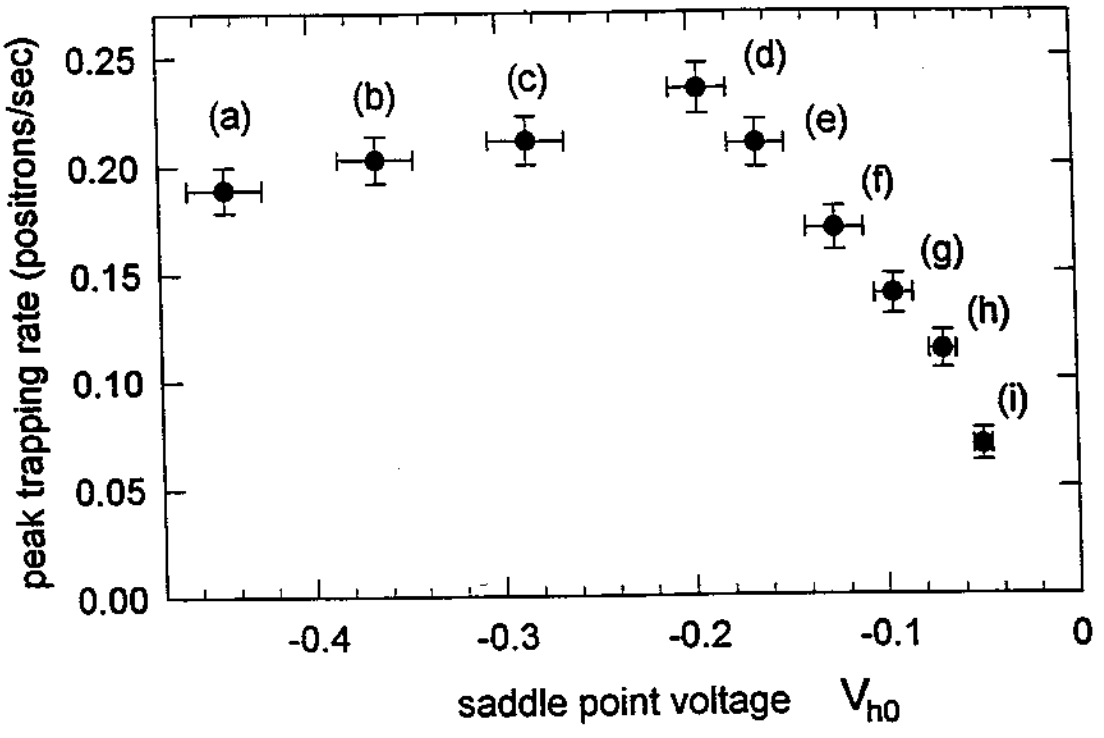

Figure 4.12: Peak trapping rate *vs.* the saddle point potential V_{h0} for the nine different values of V_{tube} shown in the previous figure.

in Fig. 4.13, which shows the measured positron loading rate *vs.* V_{ring} for three fixed values of $V_{\text{comp}}/V_{\text{ring}}$. We also note from Figure 4.13 that the peak loading rates for curves (a) and (c) are smaller than the peak loading rate for curve (b). When V_{comp} is adjusted too far positive or too far negative, the electric potential $V(\rho, z)$ inside the trap becomes increasingly anharmonic, which decreases the loading rate.

Figure 4.13 also shows that the value of V_{ring} which maximizes positron loading changes as V_{comp} is adjusted. This is better illustrated in Fig. 4.14, which shows a three-dimensional plot of loading rate (vertical axis) versus ring and compensation voltage simultaneously. The loading rate is highest along a "ridge" in the V_{ring}—V_{comp} plane. We interpret this ridge to correspond to voltages which

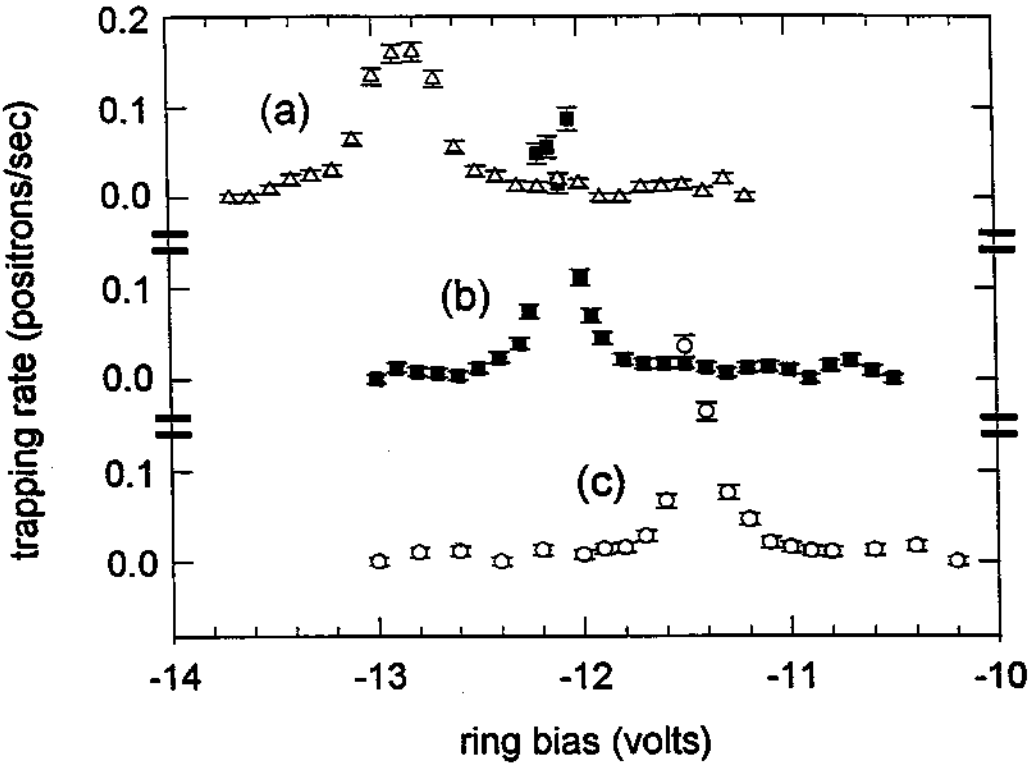

Figure 4.13: Positron trapping rate *vs.* ring bias for three values of $V_{\rm comp}$. (a) $V_{\rm comp}/V_{\rm ring} = -2.5$; (b) $V_{\rm comp}/V_{\rm ring} = +0.5$; (c) $V_{\rm comp}/V_{\rm ring} = +3.5$.

cause $\omega_z = \omega_{LC}$. We see that, as expected, ω_z depends much more strongly on $V_{\rm ring}$ than on $V_{\rm comp}$, and that the height of the ridge falls off somewhat, though not dramatically, for large (negative or positive) values of $V_{\rm comp}/V_{\rm ring}$.

The electric potential inside this hyperbolic Penning trap has been computed using a relaxation technique to solve Laplace's equation numerically [26,43]. This allows us to calculate the actual shape of the electric potential which the positron experiences during its axial orbits at $\rho = \rho_h$, which in turn allows us to compute the expected dependence of ω_z upon $V_{\rm comp}$, as a function of the amplitude of the axial motion. The results are shown in Fig. 4.15. Also shown is our *measured* frequency shift for damping the large-amplitude axial motion of our positrons—

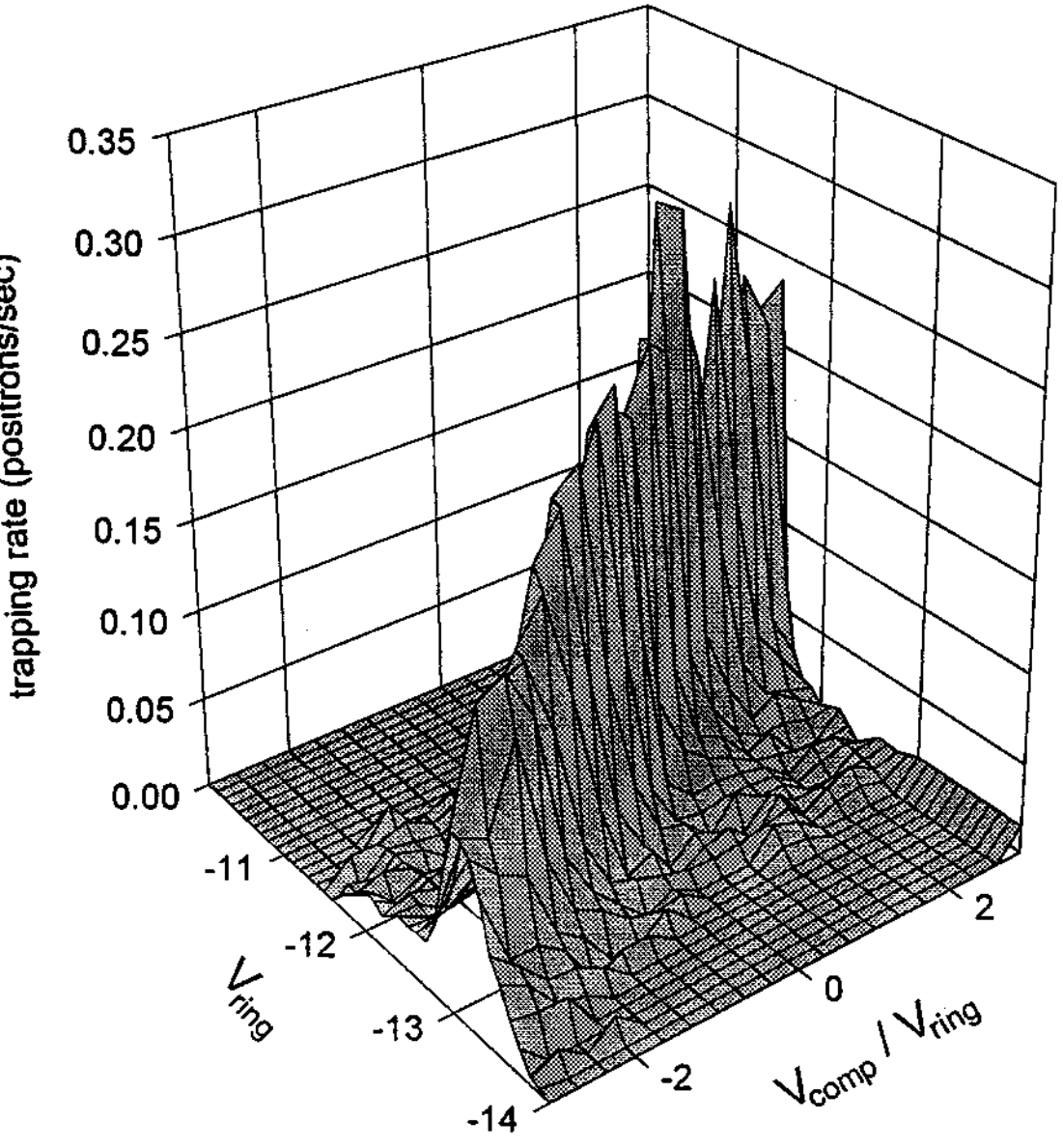

Figure 4.14: Positron trapping rate (vertical axis) *vs.* V_{ring} and the degree of compensation, $V_{\text{comp}}/V_{\text{ring}}$.

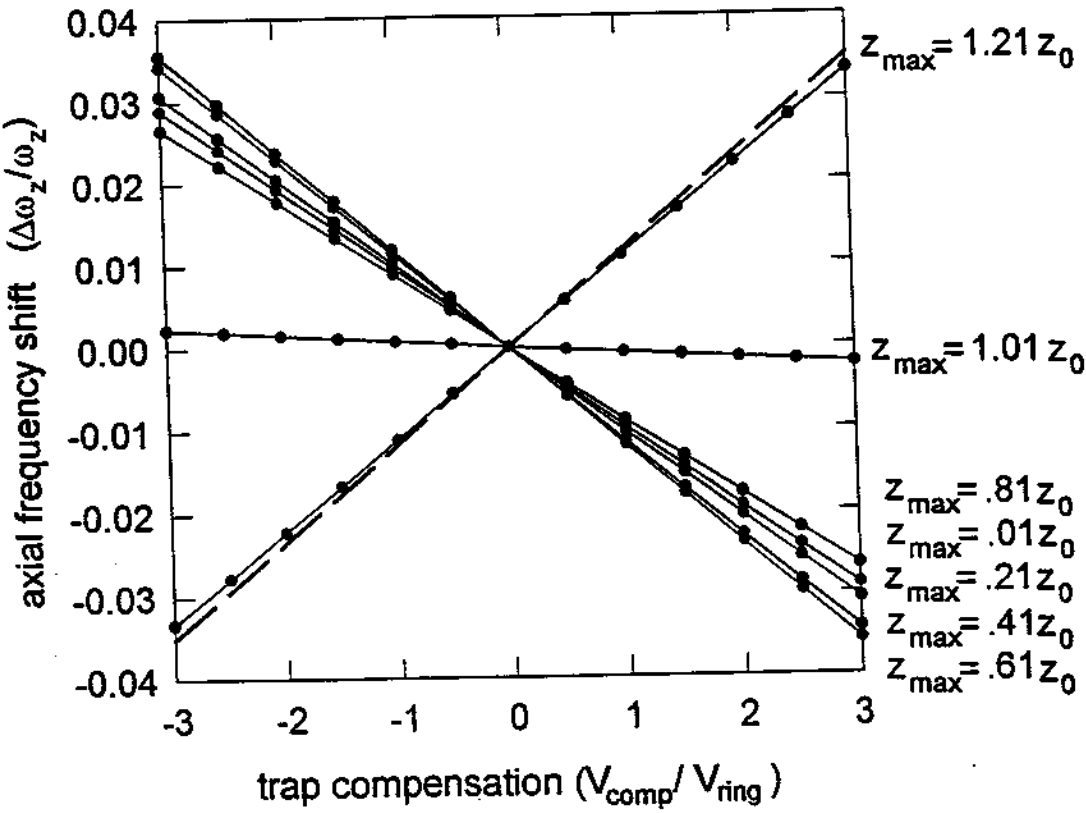

Figure 4.15: Expected shift in the positron axial frequency due to trap compensation, for several values of axial motion amplitude at $\rho = \rho_h$. The points are from computer simulations using the results of the relaxation calculation. During a positron's first magnetron orbit in the trap its axial amplitude is large, with $z_{max} = \sqrt{z_0^2 + \rho_h^2/2} = 1.21\ z_0$. The dashed line corresponds to the measured location of the "ridge" in Fig. 4.14.

which corresponds to the direction of the "ridge" in Fig. 4.14. We see that the measured "ridge" matches our calculated values for large-amplitude axial orbits at $\rho = \rho_h$. The relaxation calculation was performed for a trap without entrance apertures. The excellent agreement between calculation and experiment suggests that the positron's axial frequency is not greatly affected by the apertures during

most of its magnetron orbit.

The slopes of the lines in Fig. 4.15 can be understood qualitatively in the following way: for orbits with a large magnetron radius ($\rho_{mag} = \rho_h \approx \rho_0$) and a small axial amplitude ($z < .8\, z_0$), the compensation electrodes behave more like endcap electrodes to the positrons—that is, they are farther from the positrons in the axial direction than in the radial direction. Since we would expect a positive voltage on the endcap electrodes to *increase* ω_z (and conversely, a negative endcap voltage to decrease ω_z), we would also expect a positive $V_{\rm comp}$ to increase ω_z for small-amplitude orbits. (Recall that $V_{\rm ring} < 0$.) As the axial amplitude becomes large ($z_{\rm max} > z_0$), the positrons spend a large fraction of their orbits *between* the endcap and the compensation electrode. In this region, we would expect the compensation electrodes to behave more like the ring electrode in its effect; and we would expect the axial frequency dependence on $V_{\rm comp}$ to change its sign. These expectations are confirmed by both the simulation and by experimental results.

Figure 4.16 shows the frequency spectrum of the (4 K) thermal noise in the LRC damping circuit when the trap is empty of positrons, which reveals a typical Lorentzian shape with a center frequency of 69.780 MHz and a full width at half-maximum (FWHM) of $\sim$ 90 kHz. According to Eq. 4.8, a shift in the positrons' axial frequency of 90 kHz corresponds to a shift in $V_{\rm ring}$ of 30 mV. (We routinely verify Eq. 4.8 for small-amplitude orbits near the center of the trap, where the electrostatic potential is nearly a pure quadrupole.) Note from Fig. 4.13 that the full width at half maximum of the peak loading rate, as a function of $V_{\rm ring}$, is typically FWHM $\simeq$ 300 mV. This is approximately ten times larger than we would have expected, given a damping circuit quality factor of $Q = 780$ and harmonic axial orbits. This suggests that the large-axial-amplitude, large-magnetron-radius orbits of our positrons when they first enter the trap are somewhat anharmonic, and may also account for the fact that we typically measure a peak loading rate of $R_L \simeq 0.2\ e^+/s$, rather than the rates calculated in Eq. 4.27.

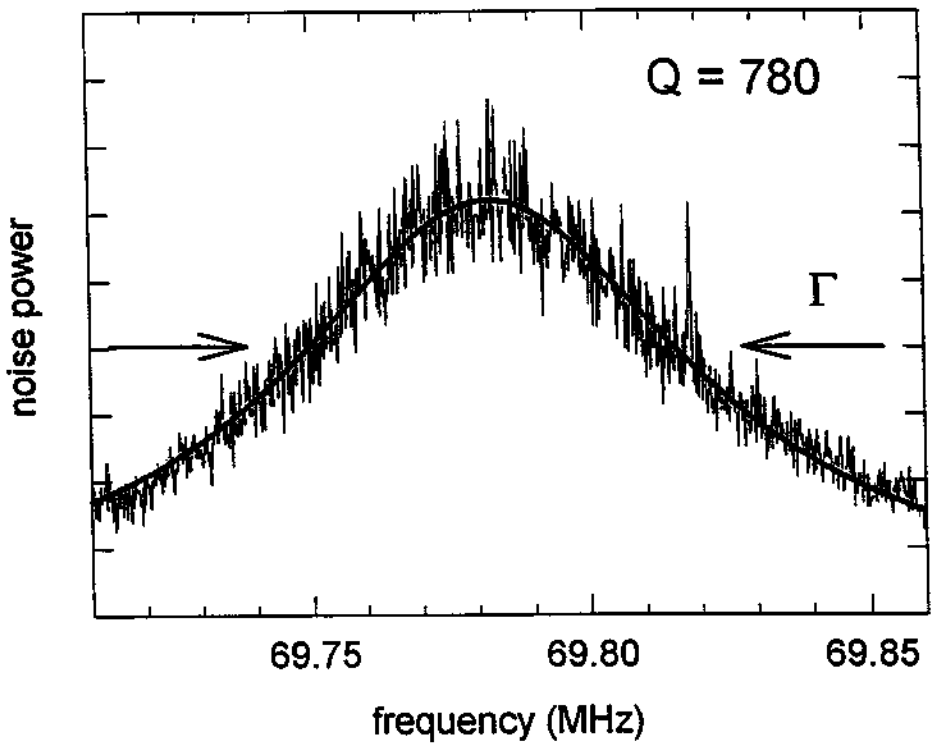

Figure 4.16: Frequency spectrum of the (4 K) thermal noise in the LRC damping circuit when the trap is empty. The darker line is a best-fit Lorentzian; the FWHM of the noise power gives the circuit's quality factor $Q = 780$. The small peak at 69.818 MHz comes from noise external to the apparatus.

4.6 Design changes to increase the loading rate

Having shown that our measured loading rate R_L is the same order of magnitude as our expectations, and that it depends upon the trapping parameters V_{ring}, V_{comp}, V_{mod}, and V_{tube} as predicted, we now consider possible design changes to the trap which could result in an increased loading rate. To facilitate this discussion, we rewrite Eq. 4.27 in terms of the physical parameters of the positrons, the Penning trap, the damping circuit, and the moderator (rather than using calculated terms

such as δE and δ_{mag}) by using Eq. 4.8, 4.12, 4.17, and 4.18, yielding

$$R_L = \frac{\eta A}{\Delta E}\left(\frac{2\pi r_e}{r_s^2}\right)\sqrt{\frac{m}{e^5}}\frac{B_t}{B_s}\left[1-\sqrt{\left(1-\frac{B_s}{B_t}\right)}\right]\left(\frac{\kappa^2\rho_h d}{z_0^2}\right)\sqrt{V_0}R. \tag{4.28}$$

Simply increasing or decreasing the physical size of the Penning trap has no large effect, since the term in parenthesis on the right side of Eq. 4.28 is approximately equal to one ($z_0 \approx \rho_h \approx d$).

The (unmoderated) positron flux on the moderator could be increased by moving the radioactive source closer to the trap (so that $B_s = B_t$) to eliminate "magnetic bouncing" (the term in brackets), while simultaneously increasing the size of the trap's entrance apertures so that $r_e \approx r_s$. This would increase the flux (proportional to r_e^2/r_s^2) by a factor of 28; however, the loading rate would only increase by a factor of 7 because R_L is proportional to the positron flux in the *active trapping window* shown in Fig. 4.9, which scales as r_e/r_s. One possible concern with this modification is that the increased apertures would adversely affect the harmonicity of the trap, causing decreased axial motion damping. This is not a serious problem once the positron's magnetron orbit carries it well away from the apertures (more than two hole radii for most of the orbit) where the effect of the apertures is small. The effective aperture radius r_e could also be increased by increasing the overall magnetic field strength, which would shrink the cyclotron radii of the unmoderated positrons.

Another way to increase the positron flux on the moderator—provided appropriate precautions are taken for the safety of the experimenters—is to increase the source activity A (without increasing its active area πr_s^2). The measurements reported in this thesis were taken when our source activity had decreased to between 10 and 12 mCi. Loading rates could be increased by a factor of 2 by purchasing a new source of the same design at 20 mCi. As noted in Section 2.1, our source self-absorbs an estimated 50% of its positrons due to the thickness of the source material. Therefore, increasing the source activity beyond 20 mCi by further increasing the source material thickness would cause little increase in positron flux.

Other positron-producing radionuclei (*e.g.* ^{58}Co) could produce more positrons over the same active area, but at the expense of a greatly reduced half-life.

If still higher loading rates are desired without further increasing the entrance apertures, it would be possible to place a more intense source (with larger active area) and moderator ***outside*** of the strong magnetic field and focusing the moderated beam onto a remoderator near the trap [9]. A 150 mCi ^{22}Na source such as is used at U.C. San Diego [46] would increase loading rates by a factor of 3 to 15, depending on the efficiencies of the moderator and remoderator.

The positron loading rate is directly proportional to the moderator efficiency η and inversely proportional to ΔE. The narrowest positron energy spread we have so far achieved is $\Delta E \simeq 230$ meV, which is considerably larger than the value $\Delta E \simeq 65$ meV reported in the literature [32,33]. This may be due to the difficulties of moderator preparation in a sealed, cryogenic environment, or due to the quality of the crystal itself. Achieving ΔE = 65 meV would increase our loading rate by a factor of 3.5.

The magnetic field strength does not directly affect ϵ, the capture efficiency for moderated positrons. An increase in B (while keeping V_0 fixed) would cause the the magnetron frequency ω_m to decrease. This would simultaneously cause $\delta_{\mathbf{mag}}$ to decrease and δE to increase proportionately, with no net change in the capture efficiency for $\delta E < \Delta E$.

Increasing V_0 (equal to $|V_{\mathbf{ring}}|$ when the endcaps are grounded) would increase the loading rate, but would also necessitate increasing the resonant frequency of the damping circuit to keep $\omega_{LC} = \omega_z$, which would have some effect on R. The effective parallel resistance R of the damping circuit (at ω_{LC}) is proportional to its quality factor Q,

$$R = \frac{Q}{\omega_{LC} C}. \tag{4.29}$$

The capacitance of the LRC circuit is usually fixed by the size of the endcap electrodes, and Q typically scales with the square root of ω_{LC} for these circuits.

Therefore, the net increase in the positron loading rate effectively scales only as the fourth root of V_0. Increasing the trapping voltages to 1000 Volts (and scaling the LRC circuit appropriately) would give us only a factor of 3 increase in loading rate. Still higher voltages would be impossible without substantially redesigning the apparatus (vacuum feedthroughs, transmission lines, filter capacitors, and the trap electrodes themselves).

It is also possible to increase Q (without changing ω_{LC} or V_0) by modifying the LRC circuit. Quality factors as high as $Q = 1450$ have been achieved on a similar Penning trap at similar frequencies [47]. This would increase our loading rate by a factor of 2, since R_L scales linearly with Q so long as $\delta E < \Delta E$.

It may be possible to improve the harmonicity of the positron's large-axial-amplitude, large-magnetron-radius motion (when it first enters the trap) by adding one or more additional sets of compensation electrodes. We know that the full-width half-maximum of our measured loading rate dependence upon V_{ring} is 10 times larger than expected (from the Q of the damping circuit), and we suspect this is due to anharmonicity in the positron's axial motion (Section 4.5.2). The additional electrodes would provide better control over the shape of the electrostatic potential. It is difficult to know whether this would increase the loading rate (by at most a factor of 10) without performing detailed relaxation calculations of the type done in Refs. [26] and [43].

Finally, it may be possible to increase the positron's magnetron drift distance during its first axial orbit δ_{mag}—without changing the magnetron frequency ω_m—by splitting the *upper* entrance tube. We expect that biasing the (unsplit) upper entrance tube (see Fig. 2.10) should cause little or no change in the loading rate, and this has been verified experimentally. If, however, the upper entrance tube were split into four quadrants, the quadrant of the tube closest to the central symmetry axis of the trap could be biased positively with respect to its opposite quadrant, creating a strong *radial* electric field in the same direction as the quadrupole radial electric field inside the trap, causing a magnetron drift which

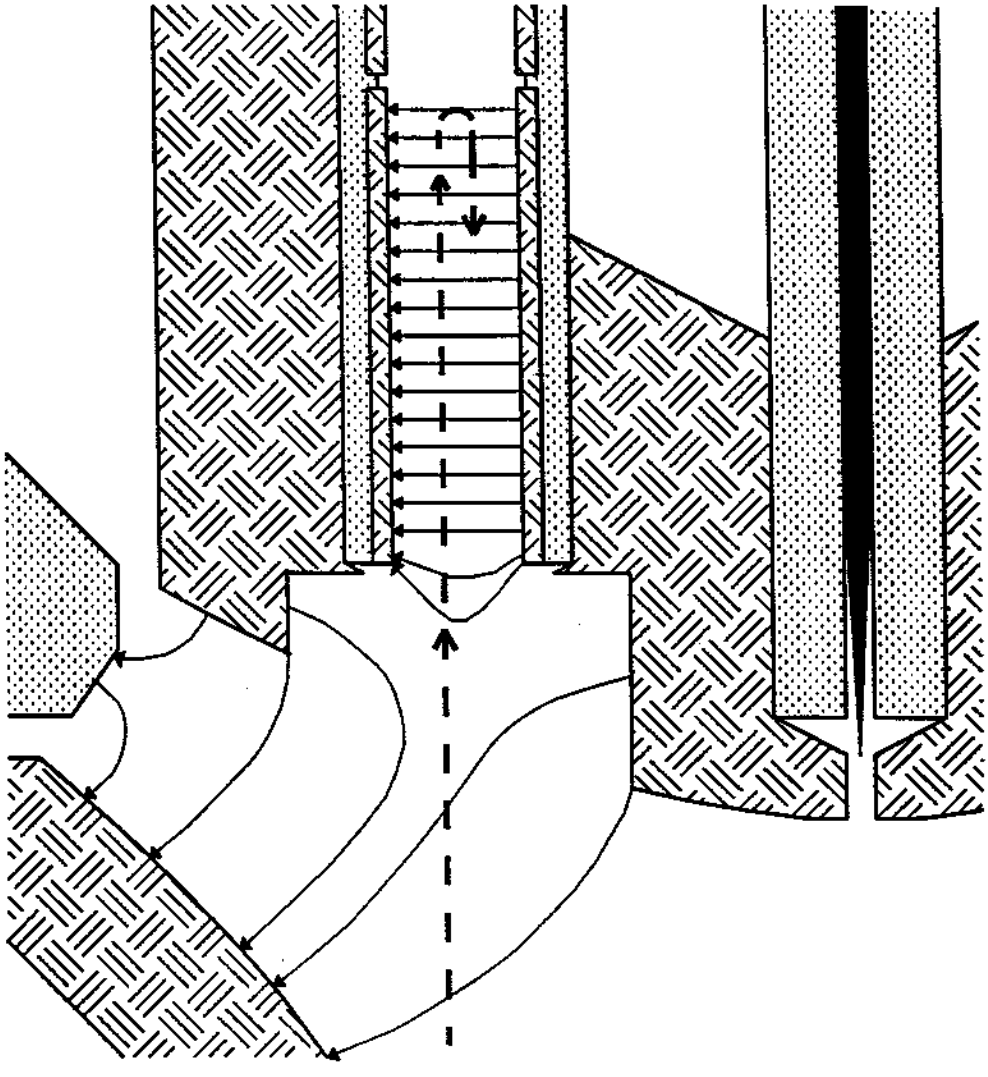

Figure 4.17: Proposed modification of the upper endcap aperture and upper entrance tube. Electric field lines are superimposed. The dashed line shows the trajectory of the positron. The upper tube is split into quadrants, allowing a strong radial electric field to be applied to increase $\delta_{\mathbf{mag}}$ locally.

is increased locally. The tube quadrants could be biased with a net negative potential (with respect to the endcaps) to insure that all moderated positrons would reach the upper tube interior; positrons could be prevented from leaking out the top end of the upper tube by adding a small, positively biased cylinder. The radial electric field inside the Penning trap during typical operating conditions is about 1 V/mm. The radial field inside the split upper tube could easily be about 1000 V/mm. This could virtually eliminate the factor of $(\delta_{\mathbf{mag}}/r_e)$ from Eq. 4.24, which would increase the loading rate R_L by a factor of ten or more. (To calculate this factor more precisely requires the solution to Laplace's equation in a split entrance tube, analogous to the calculations used in Section 4.2 for unsplit tubes. We have not yet undertaken this task.) It would be necessary to insure that positrons, having entered the (split) upper entrance tube and undergone magnetron drift, would be able to exit the tube and return to the trap volume. This could be done by grounding the remaining two tube quadrants and widening the entrance hole in the endcap electrode, as shown in Fig. 4.17. (The positrons' $\mathbf{E} \times \mathbf{B}$ motion would carry them towards a grounded tube segment, which they are energetically incapable of contacting.)

The modifications proposed in this section, along with the expected increases in R_L, are summarized in Table 4.1.

4.7 Useful electrons, unexpected positrons, and unwanted ions

There are a great many "free parameters" which must be set properly during the course of loading, accumulating, and detecting positrons. The radioactive source must be positioned so that positrons strike the moderator (Section 2.4). $V_{\mathbf{ring}}$, $V_{\mathbf{comp}}$, $V_{\mathbf{tube}}$, and $V_{\mathbf{mod}}$ must be set to accumulate positrons efficiently. After accumulating positrons for some time, $V_{\mathbf{ring}}$ and $V_{\mathbf{comp}}$ must be reset to allow

modification	parameter	current value	target value	expected gain
beam collimation	$\left(\frac{B_t}{B_s}\right)\left(\frac{r_e}{r_s}\right)$	$\sim .83$	1	1.2
magnetic "bounce"	$1-\sqrt{1-\left(\frac{B_s}{B_t}\right)}$	$\sim .17$	1	6
slow positron energy spread	ΔE	230 meV	$<$ 65 meV	3 to 4
moderator efficiency	η	1×10^{-4} (?)	10^{-3}	1 to 10
trapping voltage	$\sqrt[4]{V_0}$	$V_0 = 12$ V	1000 V	3
axial motion damping	$R = Q\omega L$	$Q = 750$	$Q = 1450$	2
magnetron drift distance	$\left(\frac{\delta_{\mathrm{mag}}}{r_e}\right)$	$\sim .02$	1	10 to 50
source activity	A	10 mCi	20 mCi	2

Table 4.1: Summary of proposed modifications to Penning trap which could increase in the positron loading rate.

for magnetron sideband cooling of the positrons, and the cooling drive strength. frequency, and sweep rate must be chosen to move positrons from their off-axis loading position to their on-axis detection position (Section 5.3). Fortunately, we were able to learn a great deal about most of these parameters by trapping electrons.

The on-axis field emission point mounted in the bottom endcap electrode (see Fig. 2.10) allows us to directly load electrons into the center of the trap, which in turn lets us test the detection and counting independently of how particles are loaded. The field emission point (FEP) emits a few nanoamps of current when it is

biased negatively by a few hundred volts. An electron beam current of 1 nA results in of order 10 electrons per second loaded into the center of the trap ($\rho \approx z \approx 0$), where they are detected and counted using their interaction with the damping circuit (Section 5.1). This technique is also used (at much lower electron beam currents) to load a single electron (or a very small number) into the center of the trap to measure the damping rate γ_z (Section 5.4).

Before we trapped any positrons, we perfected our magnetron cooling technique for moving particles from their off-axis loading position to the center of the trap ($\rho = 0$). We used the *off*-axis FEP to load (several hundred) electrons at $\rho = \rho_h$ and varied the magnetron cooling parameters until we found a technique which worked reliably. We later repeated this test with positrons (Section 5.3).

The dominant mechanism by which the FEP loads electrons into the trap is as follows: the energetic electron beam from the FEP (several hundred eV of energy) follows the magnetic field lines through the trap until it strikes a metal surface. The metal surface emits secondary electrons of about one percent of the primary beam. We measured that nearly all of these secondary electrons emerge with energies less than 3 eV. They return along the magnetic field lines, and some of them collide with the primary beam inside the trap volume. Some of these collisions result in electrons which transfer enough "axial" energy into cyclotron energy to be trapped. Once trapped, they rapidly cool to 4 K.

The measured loading rate of ~ 10 electrons per second from a 1 nA primary beam matches our expectations. Electrons emitted from the FEP with 500 eV energy have a range of cyclotron radii less than or equal to $r_c \approx 1.5 \times 10^{-3}$ cm and a velocity $v = 1.3 \times 10^9$ cm/sec. Because of the strong magnetic field, the electron beam area is $\sim \pi r_c^2$. Thus, the electron density in the (primary) beam at 1 nA (6.2×10^9 e^-/sec) is $n_{e^-} = 6.6 \times 10^5$ e^-/cm^3. Assuming a 1% emission efficiency of secondary electrons with 1 eV of energy, in a trap with length 1 cm, there is on average 1 secondary electron inside the trap volume at any given time when the primary beam is at 1 nA. Given a measured loading rate of $R = 10$ e^-/sec, the

calculated cross section for a trapping collision is $\sigma = R/vn_{e^-} = 1.1 \times 10^{-14}$ cm^2. This corresponds to an impact radius ($\sigma = \pi r_i^2$) of $r_i = 6 \times 10^{-8}$ cm. The Coulomb interaction energy between two charged particles at distance r_i is 2.4 eV, which is the expected order of magnitude for this process.

In the case of the off-axis FEP, the primary electron beam strikes is the moderator. When the moderator is biased positively ($V_{\text{mod}} \geq +5$ Volts) or the bottom entrance tube is biased negatively ($V_{\text{tube}} \leq -5$ Volts), the secondary electrons are energetically incapable of reaching the trap volume, and we detect no electrons (or very few) loaded into the trap. We know that it is possible to load positively charged ions into these traps via collisions between the primary electron beam and gas atoms released from the metal surfaces by the action of the electron beam. We would expect a few electrons to be loaded by this mechanism. The failure to detect trapped electrons when the moderator or tube are biased to prevent secondary electron return suggests that this mechanism is at least two orders of magnitude less efficient for this arrangement of electrodes.

The electron-electron collisional loading mechanism is quite different from the damping mechanism by which positrons are loaded into the trap. Electrons are loaded collisionally regardless of V_{ring} or V_{comp} (provided only that V_{ring} has the correct sign). Positrons are loaded via the damping mechanism only when the trap, tube, and moderator voltages are properly set within a fairly narrow region. Fortunately, we discovered that we could also trap (secondary) electrons via the damping mechanism by firing the off-axis FEP with the bottom entrance tube biased *positively* and the moderator biased positively by one or two volts. In fact, when V_{ring}, V_{comp}, V_{mod}, and V_{tube} are adjusted to maximize the loading rate, a 10 pA (primary) beam results in of order 1000 electrons per second trapped, which is $\sim 10^4$ times more efficiently than the collisional mechanism. The success of this technique was our first verification that the damping mechanism would work for trapping positrons. The FEP provides a much more intense incident beam than the positron source, so that electrons can be accumulated and detected

far more quickly than positrons (and independent of the quality of the moderator preparation). This proved to be very useful in our initial studies of the damping mechanism.

The energetic positron beam from the radioactive source itself liberates slow secondary electrons from the moderator, with an efficiency much higher than η. (Several tens or hundreds of slow electrons per slow positron [48,49].) Moreover, these secondary electrons are emitted regardless of the quality of the moderator. We first trapped (via the damping mechanism) and detected these electrons a few weeks after discovering damped loading of secondary electrons produced by the FEP. It was our ability to load and detect these secondary electrons produced by the positron beam—when we were at first failing to trap positrons—which led us to replace our first, defective moderator.

A few positrons per hour load into our trap *regardless* of the values of V_{mod}, V_{tube}, or V_{ring}, provided that V_{ring} is negative and that the positron beam is traveling through the trap. Since the damping mechanism cannot be involved, we expect they load by some collisional process. We are not sure where these collisions are taking place. Positrons accumulate even when the resonant drives are applied which prevent ions from loading into the trap (see below), which suggests that collisions with trapped ions are not a factor. Positron impact with the sides of the entrance apertures is a possible source. Whatever the mechanism, the first positrons we ever trapped and detected were loaded in this way. (Positrons were loaded via the damping mechanism just a few weeks later, after we replaced the defective moderator.)

Unfortunately, positive ions also load into the trap during positron accumulation (or whenever the positron beam passes through the trap, provided the ring electrode is biased negatively). Trapped ions modify the otherwise harmonic axial motion of the positrons and prevent the trapped positrons from forming a "dip" in the noise spectrum of the LRC detection circuit (Section 5.1), which makes it

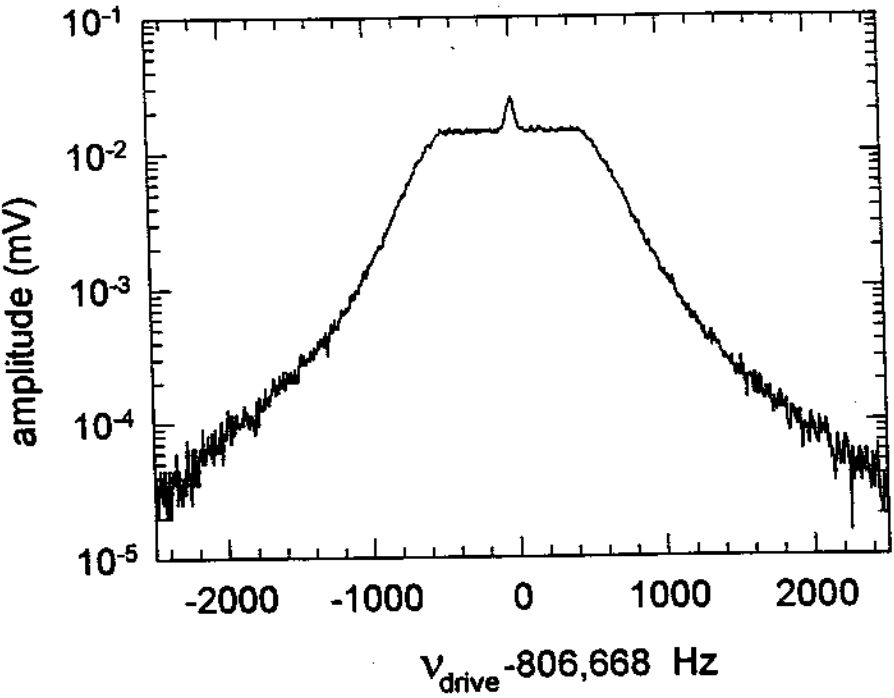

Figure 4.18: Frequency spectrum of the noise-broadened drive used to prevent ions from accumulating in the positron trap. The amplitude shown is applied to the magnet hat's vacuum feedthroughs, before losses in the transmission wires leading to the trap can. The drive frequency shown is for He^+. The axial frequency of other ions scales with the square root of the charge-to-mass ratio.

impossible to determine the number of positrons in the trap. It is still possible to *detect* the positrons via their response to the magnetron sideband excitation drive (Section 5.3), although far less effectively than when the trapped positrons are free from ions.

To prevent ions from loading during positron accumulation, we apply a drive to the bottom endcap electrode which is resonant with the axial frequencies of various ions. (The axial frequencies of the ions scale with the square root of their charge-to-mass ratio.) White noise derived from a frequency synthesizer (at +13 dBm power) is actively filtered (600 Hz low-pass), amplified (+20 dB), and mixed with the drive signal (at +7 dBm power) to noise-broaden the driving

frequency. Figure 4.18 shows a power spectrum of the resulting signal. The center frequency of the noise-broadened drive is swept in 100 Hz steps, 0.1 seconds per step, over a 1 kHz range around the axial frequency of each of the following ion species in succession: H^+, He^+, He^{++}, C^+, N^+, O^+, C_2^+, N_2^+, and O_2^+. This procedure appears to resonantly drive the ions out of the trap without affecting the positron loading. (The axial frequency of the positrons is much higher than that of the ions.) The ion drive is ***only*** applied during positron loading. While the positrons are being magnetron cooled and counted, we turn off the ion drive after closing the mechanical beam shutter.

During positron accumulation, electrons could potentially be trapped and accumulate in the region of the saddle potential at the bottom endcap aperture. A sufficiently large number of trapped electrons could shift V_{h0} due to space charge and thereby change the loading rate. To avoid this problem, we bias $V_{\mathbf{tube}}$ to +4 Volts and $V_{\mathbf{mod}}$ to +5 Volts for one second out of every minute of positron accumulation, which removes all electrons from the entrance tube region.

Chapter 5

Detection of trapped positrons

Positrons loaded into the trap through the off-axis entrance aperture dissipate energy in the LRC circuit until their axial motion comes into thermal equilibrium at 4 K. Their cyclotron energy similarly cools to 4 K via synchrotron radiation. Their magnetron motion, however, remains unchanged ($\rho_{\mathrm{mag}} \simeq \rho_h = 0.14$ inch) unless they are driven by a resonant radio frequency field. After positrons have been accumulated for a suitable length of time (typically several minutes or a few hours), they can be detected and counted through their coupling to the LRC circuit, as described in Section 5.1. In order to accurately count the number of positrons in the trap, it is necessary to move them from their large initial magnetron orbit to the center of the trap ($\rho = 0$). The technique for accomplishing this is described in Section 5.3. It is also important to measure the coupling strength between the LRC circuit and a *single* positron (or electron) in order to calibrate the positron counting technique (Section 5.4). The error bars quoted for number of trapped positrons and the positron loading rates are explained in Section 5.5.

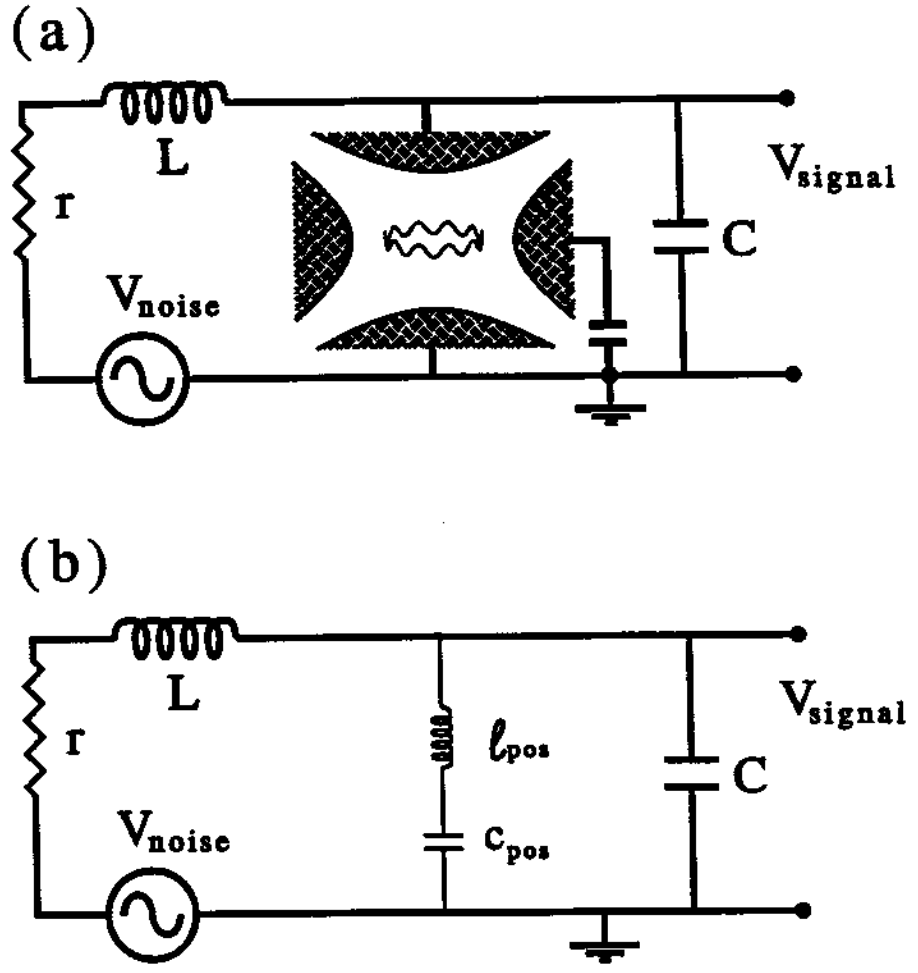

Figure 5.1: (a) Trapped positrons and the detection circuit are coupled harmonic oscillators. This is mathematically equivalent to a circuit (b) where the positrons are replaced by an inductor and a capacitor of the appropriate values [45].

5.1 Counting the positrons

The details of the interaction between trapped particles and a detection circuit have been explained elsewhere [45,50], and we give only a brief review here. The

axial motion of the positrons produces small oscillating image charges on the endcap electrodes, which in turn cause small currents to flow through the inductor L. The inductor has a small series resistance r which represents radiofrequency losses in the inductor and the rest of the detection circuit. Johnson noise in the circuit induces voltages on the endcap electrodes, to which the positrons respond. This is mathematically equivalent to the circuit shown in Fig. 5.1 when we choose [45]

$$\ell_{\rm pos} = Nm\left(\frac{2z_0}{\alpha e}\right)^2 \tag{5.1}$$

and

$$c_{\rm pos} = \frac{1}{\omega_z^2 \ell_{\rm pos}}, \tag{5.2}$$

where N is the number of positrons, $2z_0$ is the distance between the endcap electrodes, and α is a dimensionless quantity ≈ 0.5 for this trap geometry.

We now use the standard techniques of circuit analysis to determine the expected detection signal V_S. When the trap is empty, we obtain

$$|V_S(\omega)|^2 = \frac{|V_{\rm noise}|^2 \omega_{LC}^4}{(\omega_{LC}^2 - \omega^2)^2 + \omega^2\Gamma^2}, \tag{5.3}$$

where $|V_{\rm noise}|^2 = 4k_BT\,r\,\Delta\nu$ is the familiar Johnson noise at temperature T. For $\omega \approx \omega_{LC}$ this gives the Lorentzian form

$$|V_S(\omega)|^2 = \frac{|V_{\rm noise}|^2 Q^2 (\Gamma/2)^2}{(\omega_{LC} - \omega)^2 + (\Gamma/2)^2}, \tag{5.4}$$

where Q is the quality factor of the circuit and $\Gamma = r/L$ is the usual full-width half-maximum of $|V_S|^2$. An example of the noise spectrum for an empty trap is shown in Fig. 4.16. When there are positrons in the trap, Eq. 5.3 becomes [51]

$$|V_S(\omega)|^2 = \frac{|V_{\rm noise}|^2 \omega_{LC}^4 (\omega_z^2 - \omega^2)^2}{\left[(\omega_z^2 - \omega^2)(\omega_{LC}^2 - \omega^2) - \omega^2\Gamma N\gamma_z\right]^2 + \omega^2\Gamma^2\left[(\omega_z^2 - \omega^2) + \Gamma N\gamma_z\right]^2}, \tag{5.5}$$

where, as before, N is the number of trapped positrons, ω_z is their axial frequency (which need not necessarily equal ω_{LC}), and γ_z is the damping constant for the positron axial motion which we calculated in Section 4.3.

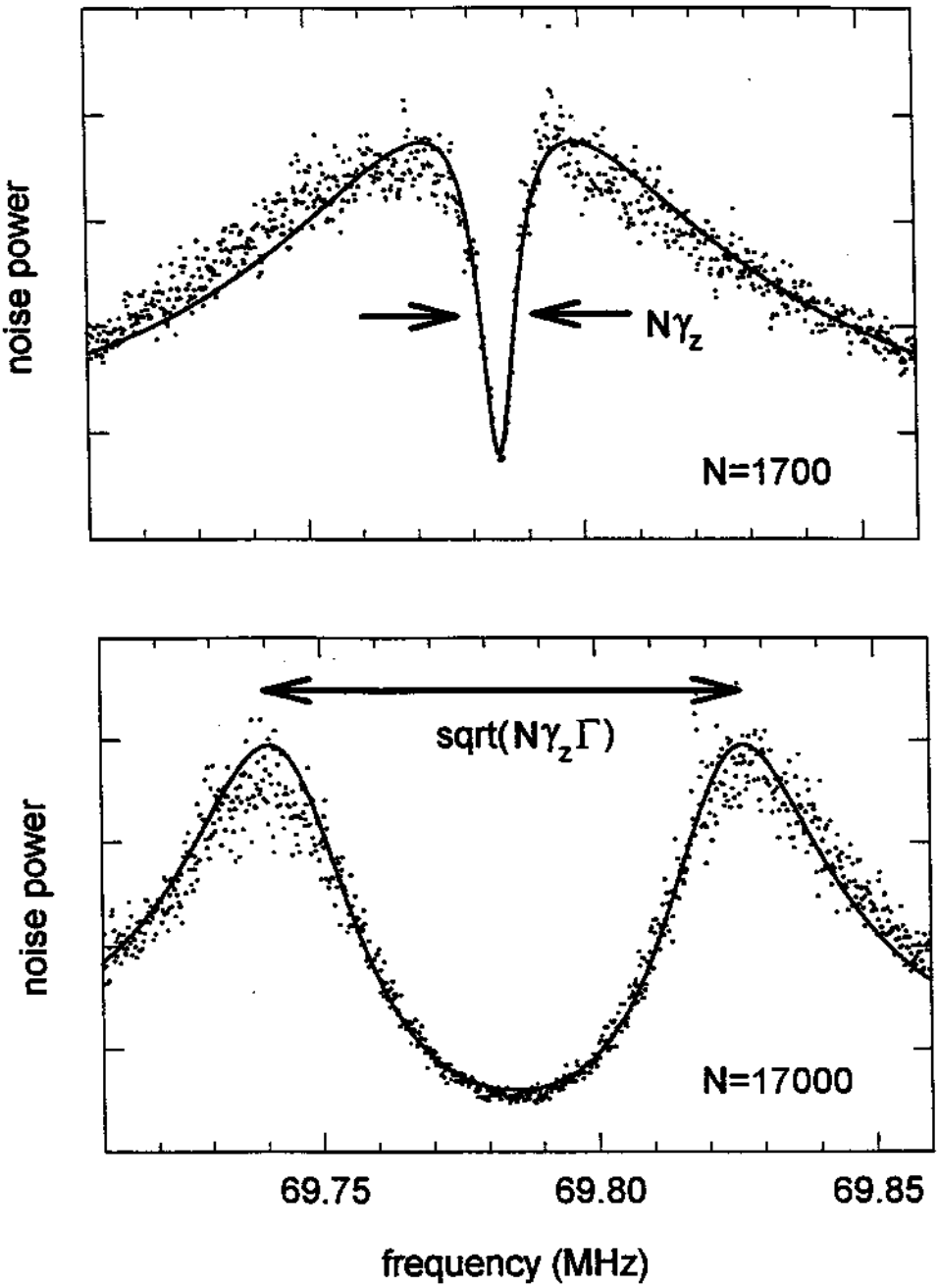

Figure 5.2: Typical noise spectra obtained from trapped positrons and the LRC detection circuit. The darker lines are least-squares fits of the theoretical lineshape. (a) Spectrum with 1700 trapped positrons. The FWHM of the "dip" is approximately equal to $N\bar{\gamma}_z$. (b) Spectrum with 17,000 trapped positrons. The maxima in the signal are separated by approximately $\sqrt{N\bar{\gamma}_z\Gamma}$.

To obtain some intuitive understanding of Eq. 5.5, we examine two limiting cases. When the number of positrons is small ($N\gamma_z \ll \Gamma$) and $\omega_z = \omega_{LC}$, Eq. 5.5 reduces to [50]

$$|V_S(\omega)|^2 \propto |V_{\text{noise}}|^2 \left[1 - \frac{(N\gamma_z/2)^2}{(\omega_z - \omega)^2 + (N\gamma_z/2)^2}\right] \tag{5.6}$$

near resonance ($\omega \approx \omega_z$). This is essentially an inverted Lorentzian "dip" in the peak noise signal with a FWHM equal to $N\gamma_z$. An example of this is shown in Fig. 5.2. The width of the "dip" is proportional to the number of trapped positrons. The other limiting case is for large N (with $\omega_z = \omega_{LC}$), also shown in Fig. 5.2; the maxima in the noise spectrum occur at frequencies

$$\omega^{\pm} \simeq \omega_{LC} \pm \frac{1}{2}\sqrt{N\gamma_z\Gamma}. \tag{5.7}$$

The separation between the maxima grows as $\sqrt{N}$.

To count the number of positrons in the trap, the noise spectra of the trapped particles and circuit are fit to the theoretical lineshape of Eq. 5.5. The least-squares curve fitting takes ω_{LC}, Γ, and γ_z as fixed parameters and adjusts ω_z (the minimum point of the dip) and N (the number of positrons) to obtain a best fit. Examples of best-fit curves are included in Fig. 5.2. The uncertainties in this measurement are discussed in Section 5.5.

5.2 Amplifying the detection circuit signal

The electrical signal produced by the positrons' axial motion and by the Johnson noise in the LRC circuit is very weak and requires a great deal of amplification before it can be analyzed. The inductor is contained in a helical resonator cavity to increase the quality factor of the circuit. We use a dual-gate, gallium arsenide FET as our first stage of amplification. The gate-1 input of the FET is capacitively connected to the inductor at approximately its midpoint. The FET, like the inductor and trap electrodes, is cooled by thermal contact to a liquid helium

reservoir to reduce thermal noise. The drain lead of the FET is impedance matched through a pi network matching circuit to a 50 Ω micro-coax cable, which carries the signal to a vacuum feedthrough on the magnet's "hat" (pictured in Fig. 2.4). The signal then goes through about 100 dB of commercially available low-noise broadband amplifiers. A more detailed description of the GaAs FET, including a wiring diagram, is contained in Refs. [23], [24], and [50].

After the signal is amplified, we analyze and store it on computer by one of two methods: (1) through the use of a commercial spectrum analyzer; (2) by mixing the signal to 5 MHz using a (frequency-swept) local oscillator, then sending the signal through a crystal filter (with a bandwidth of $\sim$ 7 kHz) and a square law detector. (The second method is only useful when the width of the "dip" produced by the trapped positrons is greater than the bandwidth of the crystal filter.) Both methods produce noise spectra such as are shown in Fig. 5.2.

5.3 Moving the positrons to the trap's central axis

It is difficult to detect trapped positrons when they are allowed to remain in their initial distribution of large magnetron orbits ($\rho_h - r_e \leq \rho_{\mathrm{mag}} \leq \rho_h + r_e$). Although it is possible to detect large off-axis clouds (more than 1000 particles) by the "dip" they produce in the noise spectrum, the dip is usually quite shallow and spread over a large frequency range. This, presumably, is due to inhomogeneities in the quadrupole potential. It is preferable to move the positrons to the center of the trap ($\rho \approx z \approx 0$), where the inhomogeneities are less important and all of the positrons move with nearly the same axial frequency. The positrons' axial motion cools to equilibrium at 4 K so long as $\omega_z \approx \omega_{LC}$. The process of shrinking the positrons' magnetron motion radius is typically called "magnetron sideband cooling."

Magnetron cooling is described elsewhere (see Refs. [52,53]), including detailed calculations of the cooling rate [22]. We give a brief description here. Since the magnetron motion is energetically unstable, it is necessary to *add* energy to this motion to reduce the magnetron quantum number and to decrease its radius. This is accomplished by applying, to one quadrant of the bottom compensation electrode, a sideband excitation drive at the frequency $\nu_z + \nu_m$. As the positrons absorb energy from this drive, both their magnetron and axial motions gain energy. The axial motion is damped by coupling to the LRC circuit, so the net effect of applying this drive is a gradual increase of the magnetron energy and a gradual shrinking of the magnetron motion radius. The cooling continues until we reach the condition [22,54,55]

$$\langle E_{\mathrm{mag}} \rangle = -\frac{\omega_m}{\omega_z} \langle E_{\mathrm{axial}} \rangle. \tag{5.8}$$

For axial motion cooled to 4 K, magnetron cooling stops when $\rho_{\mathrm{mag}} \approx 10^{-4}$cm. Figure 5.3 shows an example of the noise spectrum of a small positron cloud with the magnetron cooling drive applied. It is important that the magnetron cooling drive not be too strong, or otherwise it heats the axial motion faster than the LRC circuit can damp the energy, and the positrons are driven out of the trap. Conversely, if the cooling drive is too weak, it takes a very long time to move the positrons to the center of the trap.

Because of the inhomogeneities in the trap's quadrupole potential, we cannot expect the positron's axial frequency ν_z to be the same for all values of ρ_{mag}. In fact, depending upon V_{comp}, ν_z can vary by several hundred kilohertz between $\rho_{\mathrm{mag}} = 0$ and $\rho_{\mathrm{mag}} = \rho_h$. Therefore, we cannot expect to use a single drive frequency to cool the positrons all the way to the center of the trap.

Since this Penning trap was designed to be "orthogonalized" [26,43], we expect only a very small shift in ν_z for on-axis positrons as V_{comp} is adjusted. In fact, we measure

$$\frac{\Delta \nu_z}{\nu_z} = +3 \times 10^{-4} \frac{V_{\mathrm{comp}}}{V_{\mathrm{ring}}} \tag{5.9}$$

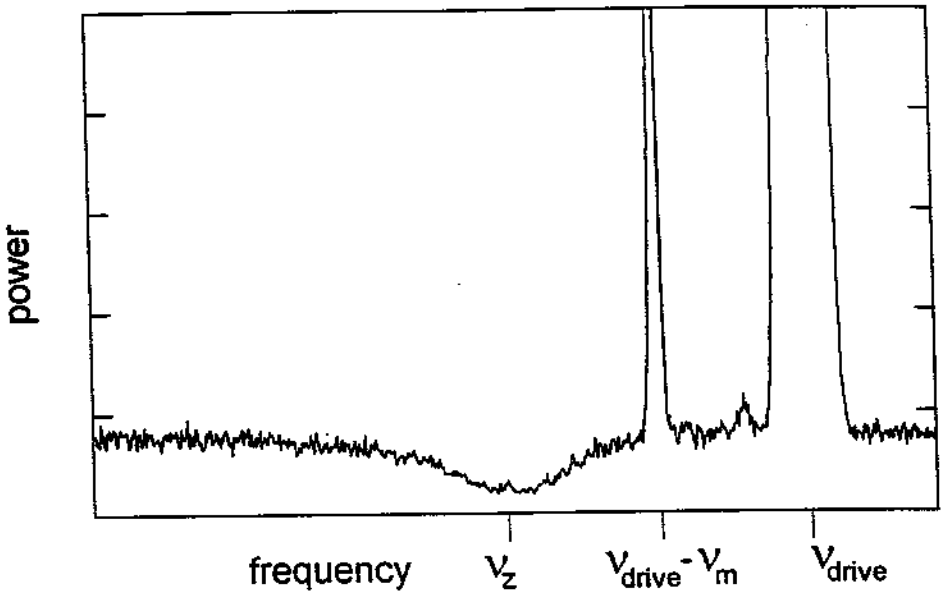

Figure 5.3: Noise spectrum of trapped positrons with the magnetron sideband cooling drive applied. The dip in the noise power is caused by the response of the trapped positrons to Johnson noise in the circuit; its center is at the axial frequency of the trapped positrons. The large signal to the right of the dip is the cooling drive. The "spike" at the right edge of the dip shows the axial motion of the positrons being excited at $\nu_{\text{drive}} - \nu_m$ in response to the drive.

for small numbers of positrons (< 500) trapped on-axis. We see from Fig. 4.15 that for off-axis positrons ($\rho = \rho_h$) in small axial orbits ($z_{\text{max}} < z_0$), we theoretically expect

$$\frac{\Delta\nu_z}{\nu_z} = -1 \times 10^{-2} \frac{V_{\text{comp}}}{V_{\text{ring}}}, \tag{5.10}$$

which is much larger in magnitude and of the opposite sign as the on-axis value.

Although it is possible to adjust V_{comp} so that ν_z is the same for both the on-axis and off-axis locations, we could not be certain that ν_z would remain constant for every radius in between. We choose instead to set $V_{\text{comp}} = 0$ Volts, which

we know empirically causes ν_z (*off axis*) $\simeq$ ν_z (*on axis*) + 400 kHz, and presumably ν_z should change monotonically for all intermediate values of ρ. We then fix V_{ring} and "sweep" the sideband cooling drive frequency slowly downward from ν_z (*off axis*) + ν_m to ν_z (*on axis*) + ν_m, which keeps the cooling drive resonant with the positrons continuously as they move to the center of the trap. Alternatively, we adjust V_{ring} so that initially $\nu_{LC} = \nu_z$ (*off axis*), and keep the cooling drive fixed at $\nu_{LC} + \nu_m$ while slowly sweeping V_{ring} upward until $\nu_{LC} = \nu_z$ (*on axis*), at which point the positrons are centered in the trap. We prefer the latter method because it maximizes the LRC circuit's damping of the axial motion throughout the magnetron cooling process.

In order to maximize the efficiency of the magnetron cooling sweep, and to ensure that we center *all* of the loaded positrons, we tested our procedure on (nearly) identical positron clouds (each loaded for equal lengths of time using identical settings) for a variety of different "sweep" settings. Those results are shown in Fig. 5.4. For each data point, the cooling drive frequency was fixed at $\nu_{LC} + \nu_m$ and V_{ring} was swept from some initial setting to a fixed final value which caused $\nu_{LC} = \nu_z$ (*on axis*). We varied the V_{ring} sweep range, the V_{ring} sweep rate, and the cooling drive power. The first graph shows the number of positrons moved to the center of the trap as a function of the V_{ring} sweep range, with a fixed (slow) sweep rate (0.1 mV per second), for a variety of different cooling drive strengths. The second graph shows the number of positrons moved to the center of the trap as a function of the total V_{ring} sweep time, for fixed V_{ring} sweep range (0.18 Volts), for a variety of different cooling drive strengths. The results show that if the sweep range is too small, or if the sweep rate is too fast, some of the positrons are not centered.

We understand these results as follows: The value of V_{ring} at the beginning of the cooling sweep must be sufficiently far from the final value so that

$$\nu_z \text{ (off axis)} < \nu_{LC} + \nu_m \tag{5.11}$$

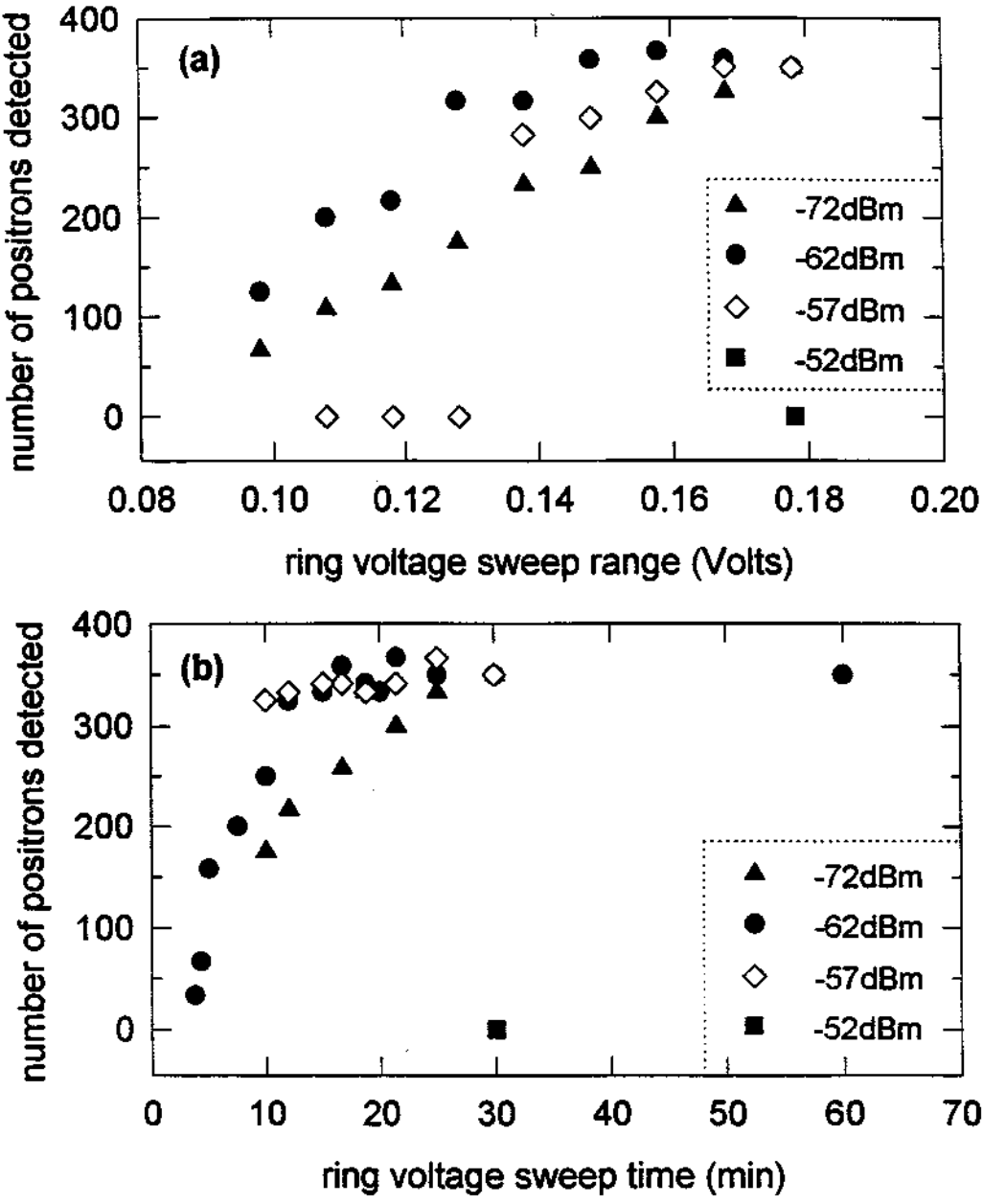

Figure 5.4: Magnetron cooling procedures for various cooling drive strengths. (a) The number of positrons moved to the center of the trap *vs.* the range of the V_{ring} sweep, at a fixed sweep rate (0.1 mV per second) and a fixed final ring voltage. (b) The number of centered positrons *vs.* the total sweep time, for a fixed ring voltage sweep range (0.18 V).

for *all* positrons loaded into the trap. If the initial value of V_{ring} is too close to the final value (*i.e.* the sweep range is too small), some of the positrons have ν_z (*off axis*) $\geq \nu_{LC} + \nu_m$; those positrons are magnetron *heated* by the drive and move *away* from the center of the trap. This explains why fewer positrons are centered when the V_{ring} range is small. Even when Eq. 5.11 holds for all positrons in the trap, not all of the positrons have sufficient time to cool to the trap center if the V_{ring} sweep *rate* is too fast, as shown in graph (b). Note that stronger drive strengths cool the positrons more quickly, allowing for a faster sweep rate. (A drive strength of −72 dBm requires at least 25 minutes to center all of the positrons, compared to 15 minutes at −62 dBm.) If, however, the drive is too strong (> -52 dBm), all of the positrons are lost.

We therefore choose a V_{ring} sweep range of 0.18 Volts, a total sweep time of 15 minutes, and cooling drive power of −62 dBm for all measurements of the positron loading rate. During the magnetron cooling sweep and also at all other times, both V_{ring} and V_{comp} are controlled through low-pass RC filters with a ten-second time constant. The cooling drive strengths listed are the strengths applied to the vacuum feedthrough at the magnet's "hat." Some small losses in power are expected in the 200 Ω twisted pair wires used to carry the signal to the vacuum feedthroughs on the trap can.

It is possible to detect the presence of even a small number of trapped positrons (< 20) during the magnetron cooling sweep, before they have been fully centered. Recall from Fig. 5.3 that, as the magnetron cooling drive heats the positron's axial motion, a "response spike" appears in the noise spectrum at one magnetron frequency sideband below the cooling drive. Often, more sidebands appear at several multiples of ν_m below the cooling drive. We monitor this signal on a spectrum analyzer during the early stages of the magnetron cooling sweep. The presence or absence of a "response spike" at the magnetron sideband is often the first indication of trapped positrons, even before a "dip" appears.

When ions are present in the trap along with positrons, the response spike

during the magnetron cooling sweep is small or non-existent until the very end of the cooling sweep. At the end of a cooling sweep with ions, no dip forms in the noise spectrum, but rather a broad ($\sim$ 1 kHz) "hump" appears in response to the sideband excitation drive.

5.4 Measuring a single positron (electron)

The use of Eq. 5.5 to count the number of trapped positrons requires knowledge of γ_z, the damping constant for a single positron. In principle, one could load a single positron (or electron) into the center of the Penning trap and measure the FWHM of the "dip" in the noise spectrum. This has recently been done in an essentially identical Penning trap with an electron [56]. The signal-to-noise caused by a single positron or electron is small, so that several minutes of integration and signal averaging are required to resolve this dip. Unfortunately, the stability of the voltage source used for V_{ring} in this experiment is inadequate. During the course of several minutes it typically drifts several tenths of a microVolt, which causes ω_z to drift several times the value of γ_z. While this small voltage drift does not affect the positron loading rate or the ability to accurately measure large clouds of positrons, it does make it impossible to directly measure γ_z by this method.

The signal-to-noise of a single trapped particle can be increased by applying a resonant axial drive and measuring the response using phase-sensitive detection [22]. We adjust V_{ring} so that $\omega_z = \omega_{LC}$ and drive the trapped particle at ω, thereby observing a signal

$$V_S(\omega) \propto V_D \frac{(N\gamma_z/2)^2 \cos\phi + (N\gamma_z/2)(\omega_z - \omega)\sin\phi}{(\omega_z - \omega)^2 + (N\gamma_z/2)^2}, \tag{5.12}$$

where V_D is the drive amplitude, N is the number of trapped particles, and ϕ is the (adjustable) relative phase between the drive and the forced response. At $\phi = 0°$ and $\phi = 90°$, we obtain the familiar absorption and dispersion response curves for damped, driven harmonic oscillators. Note that the FWHM of the

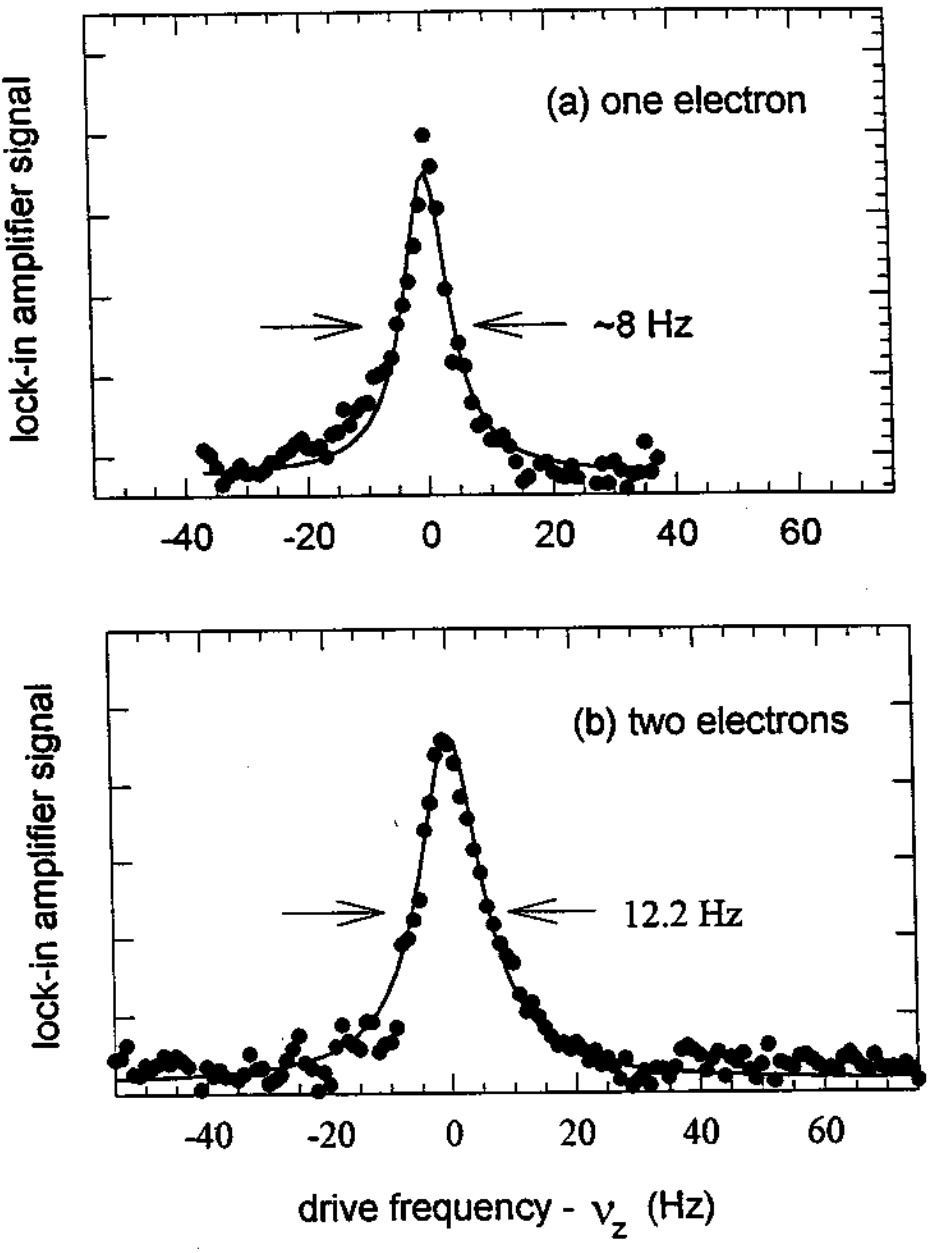

Figure 5.5: Driven response detection of (a) one trapped electron; (b) two trapped electrons. The solid curves are best-fit Lorentzians. Due to drifts in the trapping voltage, the single-electron absorption curves do not fit a Lorentzian lineshape as well as those of larger clouds.

absorption curve is $N\gamma_z$.

Under typical operating conditions, we apply a 5 MHz drive at –27 dBm power to the ring electrode and frequency sweep a second drive around $\nu_z - 5$ MHz at –17 dBm power applied to the bottom endcap. The driven response signal of the particle at $\sim \nu_z$ is mixed with the bottom endcap drive signal, filtered through a 5 MHz bandpass crystal filter, and connected to the input of a commercial lock-in amplifier. The 5 MHz drive applied to the ring electrode also provides the reference signal for the lock-in amplifier. Figure 5.5 shows examples of the output of the lock-in amplifier as a function of the driving frequency for (a) one and (b) two electrons in the trap and $\phi = 0°$. Because this method produces a larger signal-to-noise than an undriven electron, it takes much less integration and averaging time to obtain a good measurement than using the noise-spectrum technique of Section 5.1. Thus, we can make a measurement of γ_z before V_{ring} drifts significantly.

We determined γ_z by using the on-axis FEP to load a variety of small clouds into the center of the trap, ranging from one to nine electrons. (This technique is much quicker than loading and centering small clouds of positrons.) For each cloud, three or four different absorption curves were taken of the type pictured in Fig. 5.5. For each sweep, the FWHM of the lock-in signal was measured, and the results were averaged (to reduce the effect of V_{ring} drift on any particular sweep). The horizontal axis of Fig. 5.6 shows the measured widths for these clouds, which cluster at multiples of 6.1 Hz with the exception of four clouds (all of them < 17 Hz in width) which are broadened due to trapping voltage instability. The broadened clouds did not produce lineshapes which fit the Lorentzian form as well as the clouds whose FWHM clustered around multiples of 6.1 Hz. The instability in V_{ring} proved too great to obtain a good measurement of $N\gamma_z$ on single-electron clouds (and on one occasion for two electrons). Fortunately, we have a fair number of absorption curves, with nice Lorentzian shapes, with FWHM of $\sim$ 12.2 Hz, 18.3 Hz, and 24.4 Hz.

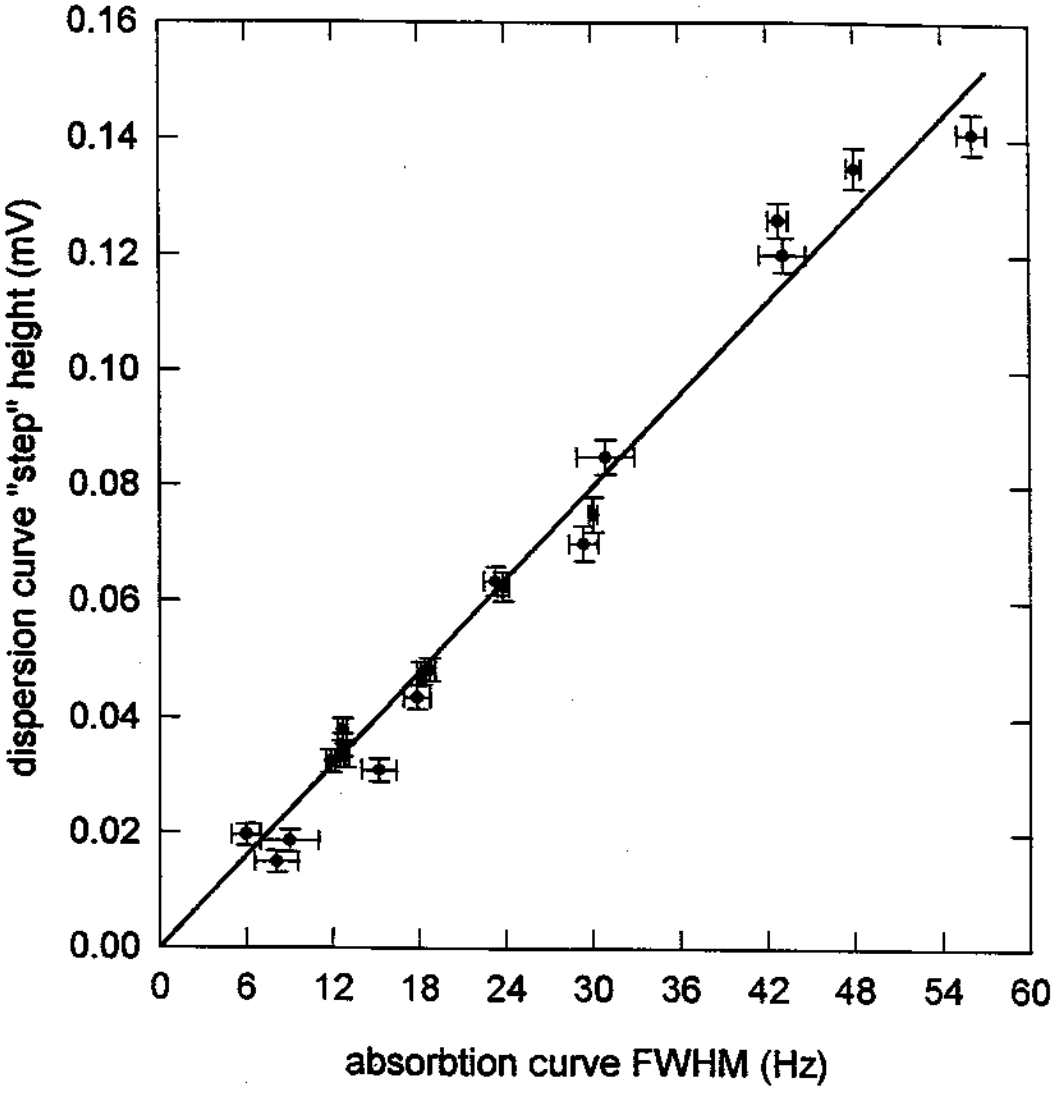

Figure 5.6: Comparison of the FWHM of the absorption curve (horizontal axis) with the height of the "step" in the dispersion curve (vertical axis) for 20 different clouds ranging from 1 to 9 electrons. The absorption FWHM ($= N\gamma_z/2\pi$) are clustered at multiples of 6.1 Hz.

In Penning traps which have a sufficiently stable voltage supply for V_{ring}, it is possible to use the lock-in signal to literally "watch" electrons load into the trap one at a time. (See for example Ref. [57].) Note from Eq. 5.12 that for large detuning in the drive frequency $|\omega - \omega_z| \gg N\gamma_z$, the dispersive component of the lock-in signal ($\phi = 90°$) is proportional to the number of electrons in the trap. By monitoring this signal continuously while the on-axis FEP is fired at a low current, it is possible to see the lock-in signal discontinuously jump each time an additional electron is trapped [50].

Because of the greater instability of V_{ring} in our trap already mentioned, we used a variation of this technique. After the measurements of the absorption curve were taken for each cloud, we rapidly shifted the endcap drive frequency to 400 Hz below resonance and increased the drive strengths by 15 dB, after which the dispersion curve ($\phi = 90°$) lock-in signal was monitored for 90 seconds. At the end of those 90 seconds, V_{ring} was adjusted to shift the electron(s) much farther out of resonance (several kHz), which gave the baseline signal level, which was also monitored for 90 seconds. The results of this procedure for most of the clouds used in Fig. 5.6 is shown in Fig. 5.7. The size of this "step" in the dispersion response for each cloud is shown on the vertical axis of Fig. 5.6, and in each case it clusters around values which are correlated with the measured FWHM of the absorption curve.

By using Fig. 5.6 to determine the number of electrons in each cloud, and averaging the measured values of the $N\gamma_z$ for each N, we obtain Fig. 5.8. The value of the best-fit line at $N = 1$ gives us a measured value of $\gamma_z/2\pi = 6.1 \pm 0.1$ Hz. All of these measurements were taken with an LRC circuit quality factor of $Q = 990$.

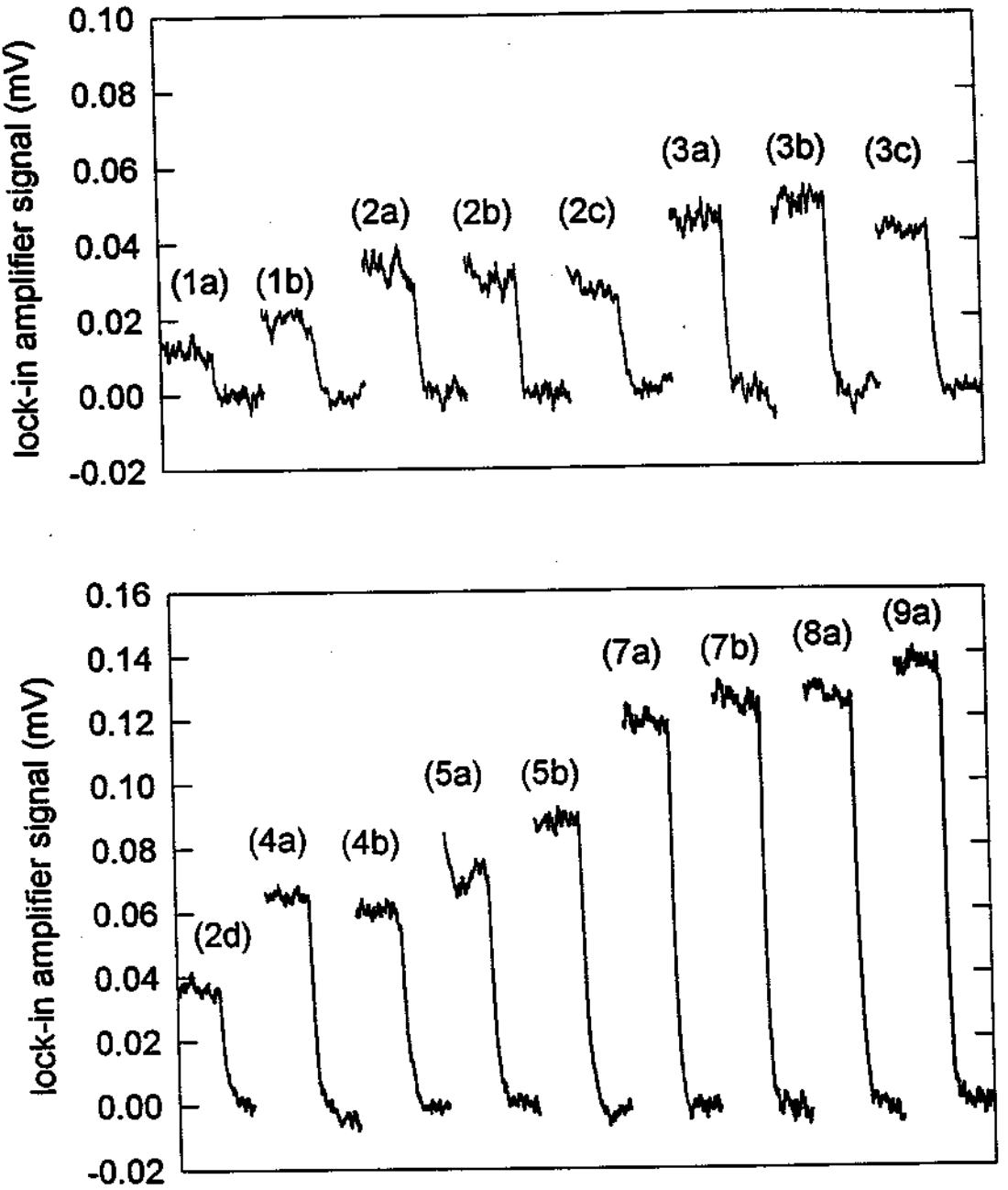

Figure 5.7: The far off-resonance dispersion ($\phi = 90°$) response of the small electron clouds used to measure γ_z.

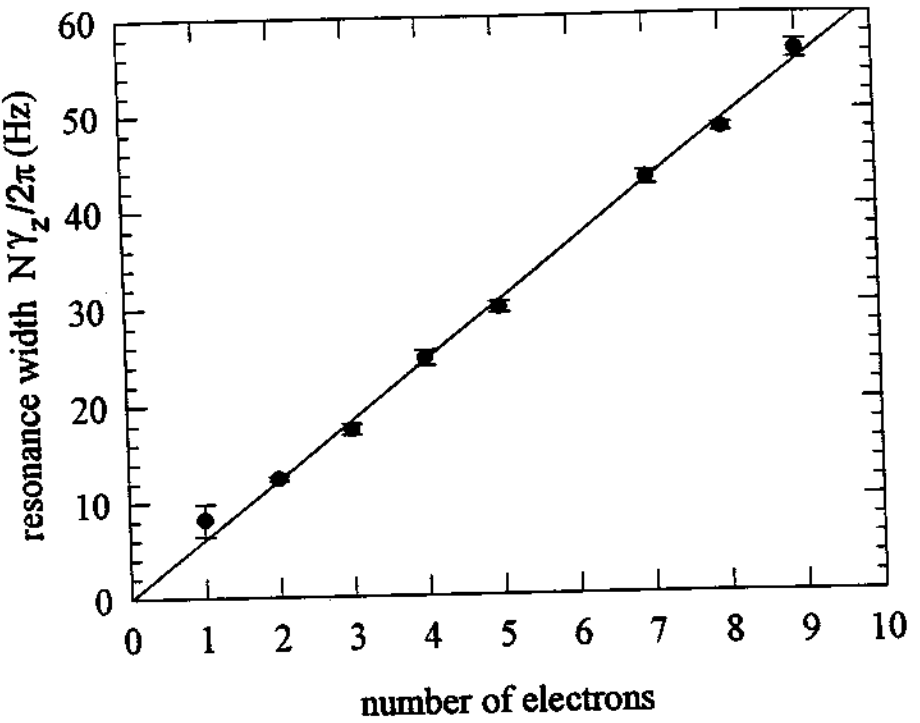

Figure 5.8: The averaged values of $(N\gamma_z/2\pi)$ for each N, where N is the number of trapped electrons and $(N\gamma_z/2\pi)$ is the FWHM of the absorption curve.

5.5 Measuring the loading rate and estimating errors.

All measurements of the positron loading rate presented in the previous chapters were taken with a total positron accumulation time of 35 minutes per data point. At the beginning of each loading cycle, V_{ring}, V_{comp}, V_{tube}, and V_{mod} were set to their chosen values and the mechanical beam shutter was opened. While positrons accumulated, a drive applied to the bottom endcap electrode resonantly drove out positive ions which might also accumulate (Section 4.7). At the end of 35 minutes, the mechanical beam shutter was closed and the ion drive was turned off. The

magnetron sideband cooling drive was then applied to move the positrons to the center of the trap, as described in Section 5.3. Finally, the noise spectrum of the LRC circuit and positrons was taken with a spectrum analyzer or a square law detector, and the spectrum was stored. The positrons were then dumped out of the trap by biasing V_{ring} and V_{comp} positively and the process was repeated. The entire procedure took approximately one hour per cycle. The loading rate was calculated by dividing the number of trapped positrons—as determined by least-squares fit to the noise spectrum—by the accumulation time.

For clouds of 1000 positrons or more, independent noise spectra of the same cloud yield slightly different values of N when fit to the theoretical lineshape, with a standard deviation of about 1%. For smaller clouds, the standard deviation proved to be ~ 10 positrons. (Clouds of fewer than 10 positrons did not produce dips which could be fit to the theoretical lineshape.) Our error estimate for lineshape fitting is therefore 1% of N for $N > 1000$ and 10 otherwise. There is also an uncertainty of 1.6% in γ_z, which we add in quadrature. When the positron loading *rate* is measured, an additional factor of $\sqrt{N}$ is added in quadrature to the error estimate due to shot noise.

The pi network impedance matching circuit on the output of the GaAs FET (Section 5.2) slightly changes the shape of the LRC circuit's noise spectrum. The Lorentzian shape of the LRC's noise (with $Q \simeq 750$) is superimposed on a much broader ($Q \simeq 10$) Lorentzian lineshape of the pi network. This is accounted for in the lineshape fitting by a small quadratic background term, although the effects of including this term on the calculated value of N are not significant.

Chapter 6

Accumulating positrons

Due to the stability of particle motions in a Penning trap and the ultra-high vacuum conditions in the trap can, positrons can be accumulated and stored for days, weeks, or even longer. We have already demonstrated accumulation of more than 36,000 positrons in 52 hours (Section 6.1), and we anticipate that substantially larger numbers are feasible. In Section 6.2 we discuss the expected storage capacity and positron lifetime limits for this trap.

6.1 Loading rate independence of accumulation time

We verify that the positron trapping rate is constant for accumulation times of less than a few hours by counting the number of positrons loaded as a function of accumulation time. An example of this is shown in Fig. 6.1. In this case, the trap was emptied after each measurement. For accumulation times of longer than a few hours, we periodically move the loaded positrons to the trap center without emptying the trap.

The results of our longest positron accumulation run to date are shown in Fig. 6.2. Every four hours the mechanical beam shutter was closed, the resonant

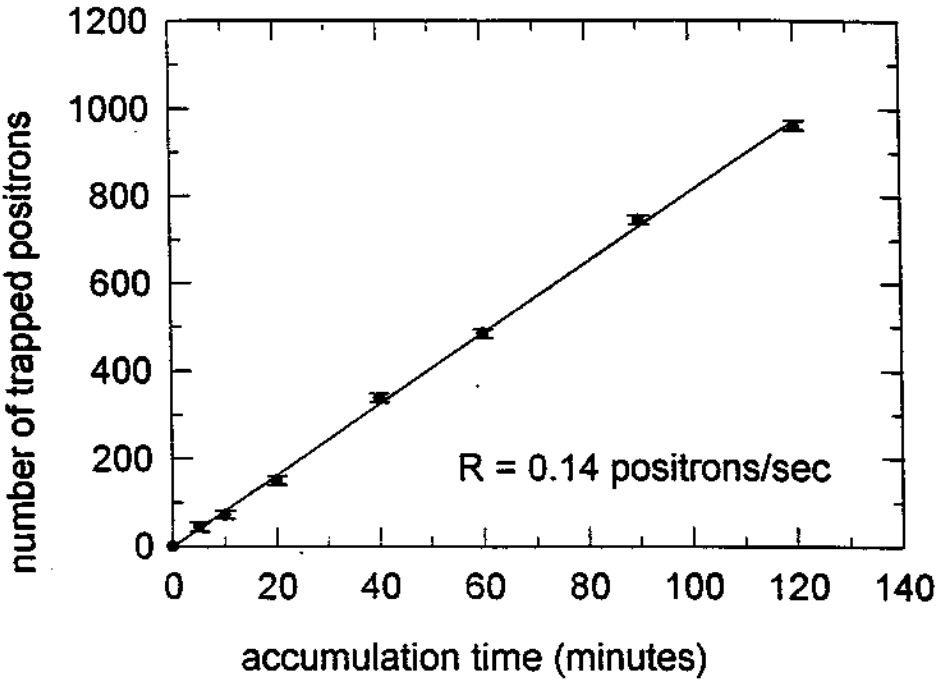

Figure 6.1: Positrons are loaded into the trap at a steady rate, independent of accumulation time between magnetron cooling sweeps, for accumulation times of at least 2 hours and possibly much longer. The trap was emptied at the end of each measurement. In this example, the loading rate was 0.14 positrons per second.

ion drive was turned off, and the accumulated positrons were moved to the trap's center and counted. Then the ion drive was resumed, the beam shutter was re-opened *without* dumping the accumulated positrons, and loading continued for another four hours. This cycle was repeated until the total accumulation time equaled 52 hours. Positrons accumulated steadily at a rate of 0.2 positrons per second, resulting in more than 36,000 trapped. The noise spectrum of this cloud is shown in Fig. 6.3. (The different loading rates between Fig. 6.1 and Fig. 6.2 are due to differences in moderator preparation.)

When the number of trapped positrons exceeds 10^4, it is necessary to make two modifications in the magnetron cooling and counting procedures. First, the axial

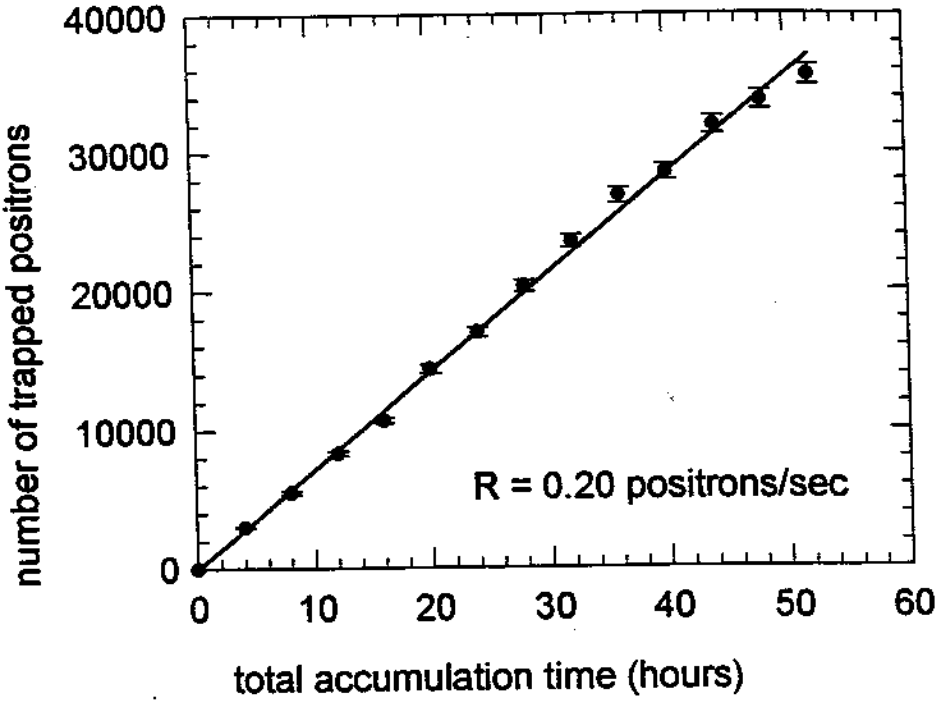

Figure 6.2: Results of the longest accumulation run to date. Positrons loaded at a constant rate of 0.20 positrons per second for 52 hours.

frequency ν_z of these large clouds is noticeably different from that of small clouds or a single positron. This is because larger clouds sample more of the inhomogeneities in the trapping potential. It is therefore necessary to slightly adjust V_{ring} during the magnetron cooling sweep to bring the axial frequency of large clouds back into resonance with ν_{LC} as positrons accumulate. Secondly, as the width of the "dip" in the noise spectrum becomes larger than ν_m, it is necessary to shift the frequency of the cooling drive so that the cooling drive does not resonantly drive the cloud's axial motion. For example, if the width of the positron dip is 50 kHz, the cooling drive should be set at $\nu_{\text{drive}} \simeq \nu_z + \nu_m + 20$ kHz (where $\nu_m \simeq 14.4$ kHz) so that the drive frequency is greater than the frequency spanned by the dip while the "response spike" at $\nu_{\text{drive}} - \nu_m$ lies within the dip. In this way, the entire positron

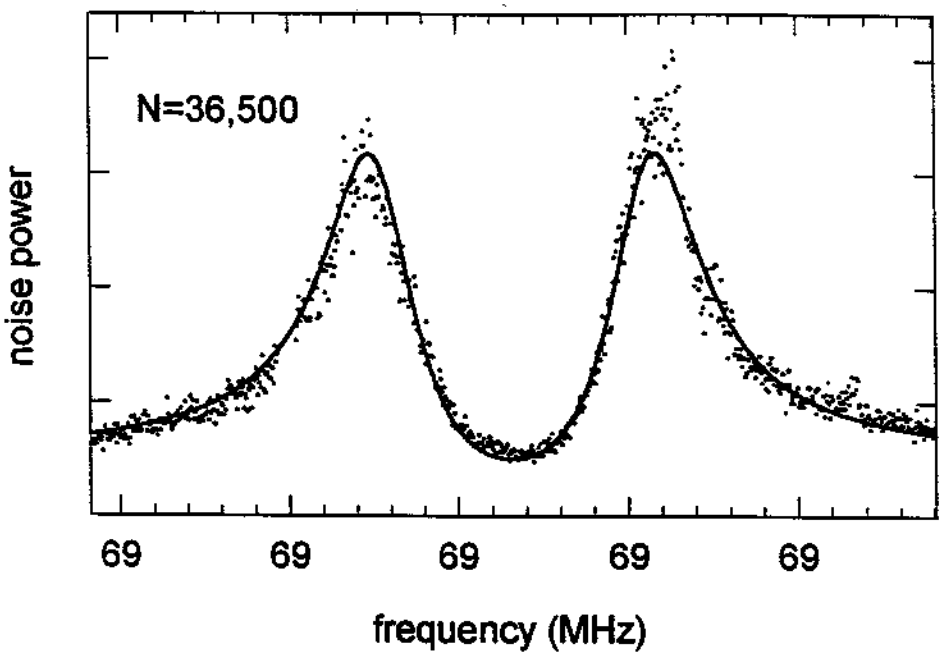

Figure 6.3: Noise spectrum of the largest positron cloud obtained to date, more than 36,000 positrons. The dark line is a fit to the theoretical lineshape.

cloud is magnetron cooled without resonantly driving its axial frequency. Further slight modifications in the magnetron cooling procedure may be necessary when the number of trapped particles exceeds 5×10^4, since the width of the "dip" in the noise spectrum will exceed the width of the LRC damping circuit. We plan shortly to begin tests by loading and centering large, off-axis electron clouds, to insure that we can magnetron cool large positron clouds without loss.

6.2 Expected limits on positron storage

There are a number of mechanisms by which positrons could be lost from the Penning trap [1]. The first we consider is radial transport of positrons out of the trap due to collisions with background gas atoms [58]. Small-angle collisions

with background gas atoms cause trapped positrons to diffusively increase their magnetron radius until they exit the trap. However, this process is unimportant for us because of the extremely high vacuum conditions. Moreover, any radial diffusion of the cloud can be overcome by applying a magnetron cooling drive. The second loss mechanism for positrons is by annihilation with electrons in the background gas atoms. This can happen either by direct annihilation, or—if the positron has sufficient kinetic energy—via positronium formation. We consider these two separately.

Positronium formation can happen only when the positron has kinetic energy greater than $E_i - E_{Ps}$, where E_i is the energy required to ionize the molecule and $E_{Ps} = 6.8$ eV is the binding energy of positronium. At 4 K the dominant background gas should be helium. The cross section for positronium formation on helium (when the positrons have sufficient kinetic energy) is known to be [59,60]

$$\sigma_{Ps} = 0.16\pi a_0^2, \tag{6.1}$$

where a_0 is the Bohr radius. Because of the ultra-high vacuum conditions in our trap can and because the kinetic energy of each positron is damped to below 1 eV rapidly (< 1 second), after which positronium formation is energetically impossible, this is not a significant loss mechanism in our trap.

Once positrons have cooled below energies for positronium formation, only direct annihilation with electrons in the background gas atoms is possible. The effective cross section for direction annihilation is given by [59,61]

$$\sigma_{\text{eff}} = \pi r_0^2 c Z_{\text{eff}}/v, \tag{6.2}$$

where $r_0 = 2.8 \times 10^{-13}$cm is the classical electron radius, c is the speed of light, v is the velocity of the positron. and $Z_{\text{eff}} = 3.94$ for helium. The expected lifetime of a trapped positron at 4 K is therefore

$$\tau = \frac{1}{n v \sigma_{\text{eff}}} \simeq \frac{3.4 \times 10^{13} \text{ sec}}{n} \tag{6.3}$$

where n is the number of background helium gas atoms per cm^3. At 5×10^{-17} Torr and 4 K, $n \simeq 10^2$ which gives a positron lifetime longer than the experimenter's.

If positron loading were continued indefinitely, we would eventually reach the storage capacity of the Penning trap. The capacity of a Penning trap is a function of its physical size and the strengths of the electric and magnetic fields. In principle, the positron density limit is determined by the Brillouin limit [62,63,64], when the particles' radial motion becomes unstable because of the large radial electric field due to space charge. This limit can be written as

$$n_{e+} < 4.8 \times 10^{12} \left(\frac{B}{1 \text{ Tesla}} \right)^2 \quad (cm^{-3}), \tag{6.4}$$

where B is the magnetic field in Tesla and n_{e+} is the number of positrons per cm^3. In practice for these traps, the density limit is also determined by the particles' space charge potential in the axial direction. Consider a spherical cloud of radius L of N_{e+} positrons. The electric potential at the edge of the cloud due to space charge is (in S.I. units)

$$\phi_{e+} = \frac{e^2 N_{e+}}{4\pi\epsilon_0 L}, \tag{6.5}$$

which must be counter-balanced in the axial direction by the trap's electrostatic potential. Assuming a uniform density of positrons in our trap (with hyperbolic electrodes) yields

$$n_{e+} \simeq \frac{10^7 V_0}{1 \text{ Volt}} \quad (cm^{-3}). \tag{6.6}$$

Since the trap has a volume of slightly less than 1 cm^3 and typically operates at $V_0 \approx 10$ Volts, our storage capacity is approximately 10^8 positrons. Accumulating 10^8 positrons at 0.2 per second would take 16 years. With significantly increased loading rates, it may become desirable to accumulate still greater numbers. This could be accomplished by drilling a larger hole in the center of the endcap electrodes and periodically moving positrons from the loading trap into another storage trap which could be operated at higher containment voltages. A Penning

trap at U.C. San Diego operating at several kilovolts has achieved 10^9 trapped electrons at a density of 2×10^{10} electrons per cm^3 [63]. Therefore, the storage capacity of these traps does not currently limit positron accumulation, and is more than adequate for the applications outlined in Chapter 7.

Chapter 7

Applications

The positron trapping system which we have developed meets the criteria (discussed in Chapter 1) of being small (the positrons originate from a small radioactive source, rather than a large accelerator facility), capable of operating under ultra-high vacuum conditions (no buffer gases are required to slow the positrons), and capable of accumulating positrons continuously over long periods of time. Of primary interest during the development of this trap was the possibility of producing antihydrogen by merging cold, trapped plasmas of antiprotons and positrons; this is discussed in Section 7.1. Another potential application is using positrons to cool highly stripped ions, as discussed in Section 7.2. Several other potential applications are discussed briefly at the end of the chapter.

7.1 Antihydrogen

Now that both positrons and antiprotons have been trapped at 4 K, it should be possible to produce and study antihydrogen at these low temperatures [11]. Spin-polarized hydrogen atoms have already been magnetically confined and studied at dilution refrigerator temperatures [16,17.18]. Laser cooling and magneto-optical trapping of atoms such as sodium, rubidium, and cesium has become fairly common in recent years. Laser cooling of (anti)hydrogen is certainly more diffi-

cult because of the challenges in producing a sufficiently powerful Lyman-alpha laser, although some laser cooling of hydrogen has already been demonstrated [18]. Spectroscopic comparisons of hydrogen and antihydrogen—for example, measurement of the 1s–2s transition or the fine and hyperfine intervals—would provide extremely precise tests of CPT symmetry. The standard model, while allowing for C-violation, P-violation, and CP-violation, does not allow CPT-violation. CPT symmetry implies that particles and antiparticles must have exactly opposite electric charges and magnetic moments, and identical masses and lifetimes. A spectroscopic comparison of hydrogen and antihydrogen could provide a more precise CPT test than is typically possible with measurements on single particles [65].

It has recently become possible, through the use of laser cooling, to measure the gravitational acceleration on single atoms. Attempts to measure the gravitation force on charged antiparticles would be extremely challenging because very tiny electric forces can easily overwhelm the gravitational force, as was demonstrated with electrons [66]. Electrically neutral antihydrogen atoms would avoid this problem.

7.1.1 Trap design for combining antiprotons and positrons

Antiprotons are captured, stored, and studied in an apparatus nearly identical to our positron trapping apparatus. (The antiproton trap is described in Refs. [67,23,24].) The two significant differences are: (1) The bottom of the magnet and the bottom of the antiproton trap can are connected to the Low Energy Antiproton storage Ring at CERN via thin vacuum windows which allow antiprotons to pass through; (2) the antiproton Penning trap electrodes are not of a hyperbolic geometry, but rather of an open-endcap cylindrical geometry which we designed to maximize the harmonicity of the trapping potential (for a cylindrical geometry) to facilitate storage and high-precision measurements [67].

An overview of the proposed scheme for producing antihydrogen is represented

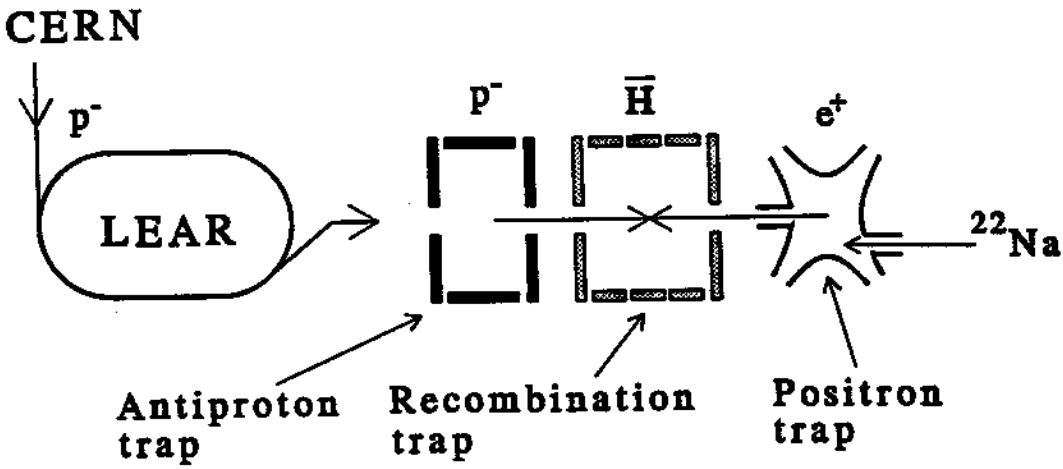

Figure 7.1: Representation of the proposed antihydrogen production scheme. The antiproton trap, positron trap, and recombination trap would all reside in the same cryogenically cooled, vacuum-sealed trap can.

in Fig. 7.1. Antiprotons from LEAR would enter the trap can and accumulate in a storage trap. Positrons would also accumulate (using a trap similar to the one described here) in the same vacuum-sealed trap can. When a sufficient number of both species had been attained, they would be transfered to the "recombination trap" where they could be made to overlap, either by using a nested pair of Penning traps (Fig. 7.2) in which the antiprotons oscillate slowly through a central potential well filled with positrons [68], or by superimposing a radiofrequency signal on the Penning electrodes, which is capable of confining both charged species in the same space by the same mechanism as a Paul trap. Antihydrogen recombination could be signaled by several different mechanisms, including (1) detection of photons, (2) the loss of equal numbers of positrons and antiprotons, and (3) field ionization of the resulting antihydrogen atoms (assuming they are produced in a sufficiently small binding energy state) and detection of the products in a region of the trap

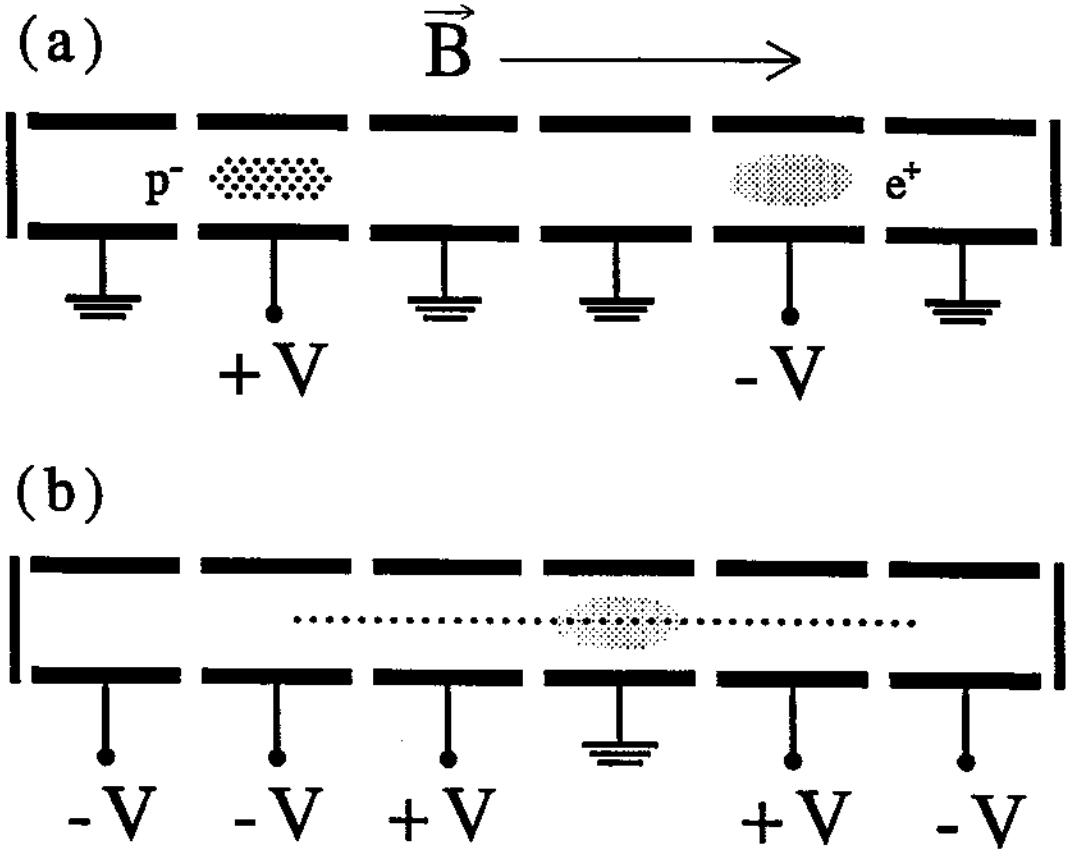

Figure 7.2: Nested Penning traps could be used for antihydrogen production. (a) Antiprotons and positrons are accumulated in separate traps. (b) Antiprotons are made to oscillate through the positron cloud, allowing recombination.

can which is inaccessible to electrically charged particles. We have already built such a trap to test ordinary hydrogen recombination under conditions identical to those expected for antihydrogen, and results are expected in the near future.

7.1.2 Recombination rates

When antiprotons are completely contained within a positron plasma, radiative recombination

$$p^- + e^+ \rightarrow \overline{H} + \gamma \tag{7.1}$$

proceeds at a rate [11,69]

$$R_{\overline{H}} \simeq 3 \times 10^{-11} \left(\frac{4.2}{T}\right)^{1/2} N_{p^-} n_{e^+} \quad s^{-1}, \tag{7.2}$$

where T is the temperature of the positrons. We have assumed that the antiproton velocity is equal to or less than the average positron velocity. For a positron density $n_{e^+} = 10^8/\mathrm{cm}^3$ and a number of antiprotons $N_{p^-} = 10^5$, at 4.2 K, this yields a recombination rate $R_{\overline{H}} = 300/\mathrm{sec}$.

The three-body recombination mechanism

$$p^- + e^+ + e^+ \rightarrow \overline{H} + e^+ \tag{7.3}$$

may be more efficient by many orders of magnitude [11]. Its rate has been calculated in various ways [70], including under conditions of high magnetic field [71], giving

$$R_{\overline{H}} \simeq 10^{-12} \left(\frac{4.2}{T}\right)^{9/2} N_{p^-} n_{e^+}^2 \quad s^{-1}. \tag{7.4}$$

Note the sensitive dependence upon temperature and the squared dependence upon positron density. We can understand these dependences by noting that the relevant length scale for a Coulombic collision is the Thomson radius ($r_T = 2e^2/3k_BT$), the distance at which the Coulomb interaction energy is equal to $\frac{3}{2}k_BT$. Taking $\tau \approx r_T/v$ to be the duration of a collision, r_T^2 as the cross-section of an antiproton-positron collision, and $(n_{e^+} r_T^2 v\tau)$ the probability of a second positron being in the region during the collision, yields

$$R_{\overline{H}} \sim \frac{(n_{e^+} r_T^2 v\tau)^2}{\tau} \sim n_{e^+}^2 T^{-9/2}, \tag{7.5}$$

since the positron velocity v scales as $T^{1/2}$.

Assuming $N_{p^-} = 10^5$ and $n_{e^+} = 10^8/\mathrm{cm}^3$ as above, Eq. 7.4 gives a recombination rate of $R_{\overline{H}} = 10^9/\mathrm{sec}$. Of course, N_{p^-} sets a limit on the total *number* of antihydrogen atoms produced. One potential problem with collisional recombination is that the initial positron capture occurs within a few $k_B T$ of the ionization limit, producing highly excited atoms. However, the resulting antihydrogen atoms will be moving slowly and could possibly be held by their large magnetic moment long enough for collisional de-excitation to a state where spontaneous emission de-excitation would dominate.

7.2 Cooling trapped ions

It is quite challenging to cool highly stripped, heavy ions from the several-keV energies at which they are typically produced and trapped to sub-eV energies, where they can be studied more carefully. Heavy ions under these conditions do not rapidly radiate away their kinetic energy the way positrons do, nor is their motion easily damped with resistive circuits. Neutral buffer gases which might be used to slow the trapped ions would also undergo charge-exchange processes with the ions. Cold positron plasmas could be a very useful tool in cooling these energetic, highly-stripped ions. The ions would rapidly lose energy via collisions with positrons as they oscillate through the trap; the positrons in turn quickly cool themselves via synchrotron radiation. The process is exactly analogous to electron cooling of trapped antiprotons [13], which has already been demonstrated to work efficiently [12,14]. Unlike buffer gases, the positrons would not cause ion loss via charge transfer processes.

Using a positron buffer plasma to cool heavy ions would have several advantages over other possible buffer plasmas (*e.g.* protons). Unlike positrons, trapped protons do not cool themselves via synchrotron radiation under typical laboratory conditions (several Tesla). Because of their small mass, positrons would be eas-

ily purged from the ion trap once the ion cooling was completed. Under many conditions, the ions transfer their energy *more* efficiently to the lighter positrons than they would to a similar cloud of protons. The rate of ion cooling to a buffer plasma which is synchrotron cooled to 4.2 K is given by [13,72]

$$\frac{d}{dt}T_i = -\frac{1}{\tau_{eq}}(T_i - T_b), \tag{7.6}$$

$$\frac{d}{dt}T_b = \frac{N_i}{N_b\tau_{eq}}(T_i - T_b) - \frac{1}{\tau_{synch}}(T_b - 4.2), \tag{7.7}$$

where T_i is the ion temperature, T_b is the buffer plasma temperature, N_i and N_b are the numbers of ions and buffer particles, respectively, and (in cgs units)

$$\tau_{eq} = \frac{3k_B^{3/2}M_i m_b}{8\sqrt{2\pi}\,e^4(\ln\Lambda)Z^2\,n_b}\left(\frac{T_i}{M_i} + \frac{T_b}{m_b}\right)^{3/2}, \tag{7.8}$$

where k_B is Boltzmann's constant, M_i and m_b are the particle masses, Z is the ion charge, n_b is the buffer particle density, and

$$\Lambda \simeq \frac{3}{2Ze^3}\sqrt{\frac{k_B^3\,T_b^3}{\pi\,n_b}}. \tag{7.9}$$

We can use these equations to numerically simulate ion cooling and obtain equilibration rates. Results for one such calculation, comparing positron and proton buffer plasmas, is shown in Fig. 7.3.

7.3 Improved positron lifetime measurement and potential UHV gauge

By loading a large cloud of positrons and monitoring its signal over time, we expect to use this positron trap to establish a new limit on the lifetime of the positron in the same way as was done with antiprotons [15]. In the same way, in limited applications, positron traps could be useful in measuring background gas at pressures below which conventional ion gauges do not operate (10^{-12} torr).

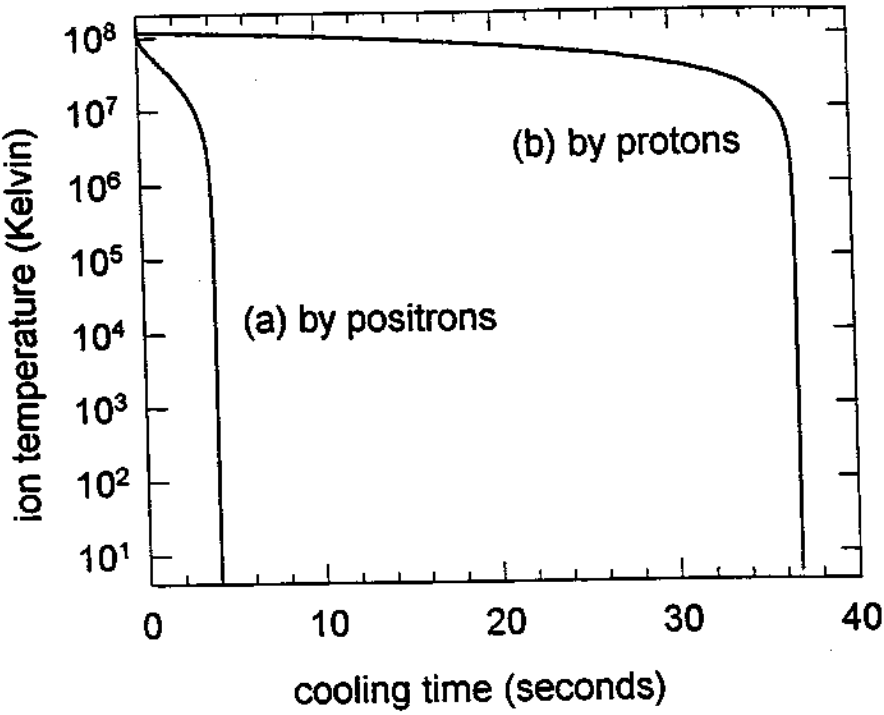

Figure 7.3: Results of a computer simulation cooling $N_i = 10$ fully stripped Uranium-238 ions from 10 keV to 4.2 K using buffer plasmas ($N_b = 10^5$, $n_b = 10^8/cm^3$) of (a) positrons and (b) protons.

Figure 7.4 shows the expected lifetime of a trapped positron as a function of background gas pressure for selected molecules [59,60]. A positron annihilation vacuum gauge would operate by initially loading a cloud of positrons and determining their lifetime by periodically monitoring the number of remaining positrons. To make this device feasible, the positrons would need to be heated by resonant drives to energies which allow positronium formation ($\sim$ 10 eV) in order to increase their annihilation cross-section.

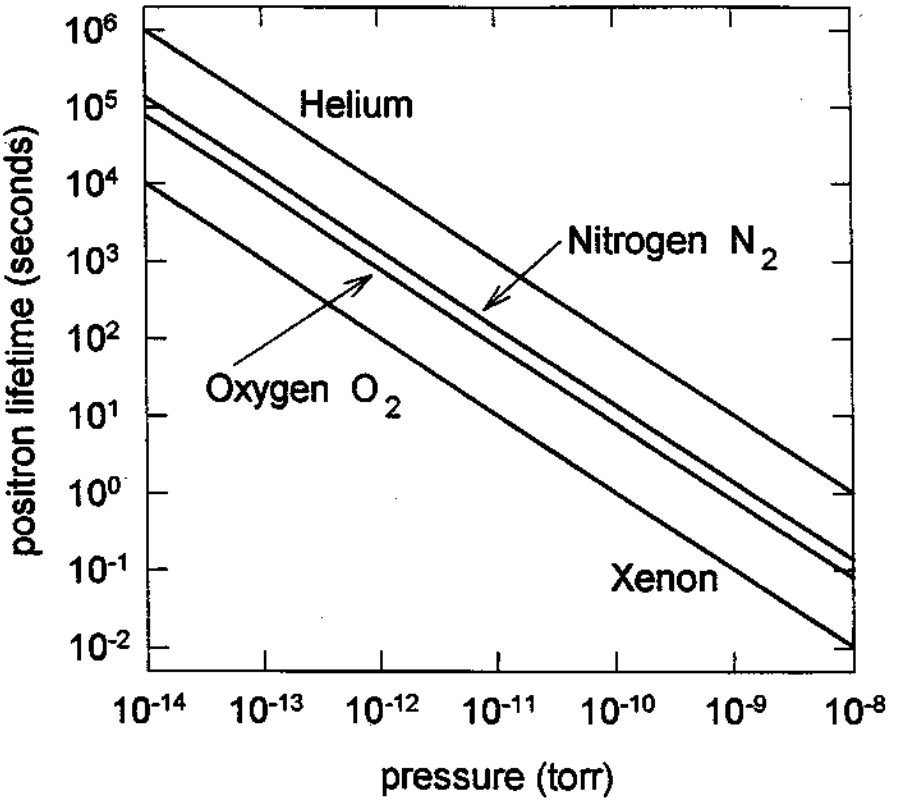

Figure 7.4: Calculated positron lifetime *vs.* background gas pressure for various atoms and molecules. The positrons are assumed to be at 10 eV energy and annihilate via positronium formation.

Chapter 8

Conclusion

We have built and demonstrated a Penning trap which accumulates positrons from a 10 mCi sodium-22 source at a rate of 0.2 positrons per second. Positrons are stored under cryogenic (4 K), ultra-high vacuum ($< 5 \times 10^{-17}$ Torr) conditions and are counted non-destructively via their interaction with a detection circuit, so positron loss from the trap is inconsequential. In one demonstration, positrons loaded steadily for 52 hours, yielding more than 3.6×10^4 trapped positrons. Larger numbers are anticipated with longer accumulation times. At the demonstrated rate, 1.2×10^5 positrons would accumulate in one week, and 10^6 in two months.

The use of a positron moderator is an important feature of our apparatus. In order to achieve a high trapping rate, the moderator must eject positrons with a high efficiency η and a small energy spread ΔE. Field emission point arrays are very useful for cleaning and annealing moderators at temperatures exceeding 2000 K inside the sealed, cryogenic, high magnetic field environment of the trap. Unfortunately, we encountered some difficulties with the long-term reliability of these devices in this environment. When this problem is solved, we hope to optimize the moderator performance. Achieving values of η and ΔE equivalent to the best reported in the literature would increase our trapping rate by a factor of 4 or more.

The demonstrated positron loading rate depends on bias voltages and other trapping parameters as expected. The maximum trapping rate we measure is within our expectations, based upon positron dynamics in the trap and detailed calculations of the electrostatic potentials near the trap entrance apertures. Several modifications to the Penning trap apertures, the loading tubes, the damping circuit, and the position of the radioactive source in the magnetic field would potentially increase the trapping rate by as much as two additional orders of magnitude or more.

Trapped positrons could be useful as a buffer plasma to cool and trap highly stripped ions. The trap vacuum enclosure, liquid helium dewar, superconducting magnet, support apparatus, and detection electronics used in this experiment are all nearly identical to those used to capture, accumulate, and study antiprotons in a Penning trap. The number and density of trapped positrons achievable with this apparatus are sufficient to produce antihydrogen at a high rate when the cold, trapped plasmas of antiprotons and positrons are mixed. Studies of antihydrogen would provide important tests of CPT invariance and the weak equivalence principle.

Bibliography

[1] Paul Schwinberg, Ph.D. thesis, University of Washington, 1979.

[2] P.B. Schwinberg, R.S. Van Dyck, Jr., and H.G. Dehmelt, Phys. Lett. **A81**, 119 (1981).

[3] R.S. Van Dyke, Jr., P.B. Schwinberg, and H.G. Dehmelt, Phys. Rev. Lett. **59**, 26 (1987).

[4] A.P. Mills, Jr., Appl. Phys. Lett. **37**, 667 (1980).

[5] E.M. Gullikson, A.P. Mills, Jr., W.S. Crane, and B.L. Brown, Phys. Rev. **B32**, 5484 (1980).

[6] A. Vehanen, K.G. Lynn, P.J. Schultz, and M. Eldrup, Appl. Phys. **A32**, 2472 (1983).

[7] P.J. Schultz and K.G. Lynn, Rev. Mod. Phys. **60**, 701 (1988).

[8] G. Gabrielse and B. Brown, in *The Hydrogen Atom*, edited by G.F. Bassani, M. Ingscio, and T.W. Hansch (Springer, Berlin, 1989) p. 196.

[9] L. Haarsma, K. Abdullah, and G. Gābrielse, Hyperfine Interactions **76**, 143 (1993).

[10] G. Gabrielse, X. Fei, K. Helmerson, S.L. Rolston, R.L. Tjoelker, T.A. Trainor, H. Kalinowski, J. Haas, and W. Kells, Phys. Rev. Lett. **57**, 2504 (1986).

[11] G. Gabrielse, S.L. Rolston, L. Haarsma, and W. Kells, Phys. Lett. **A129**, 38 (1988).

[12] G. Gabrielse, X. Fei, L.A. Orozco, S.L. Rolston, R.L. Tjoelker, T.A. Trainor, J. Haas, H. Kalinowski, and W. Kells, Phys. Rev. **A40**, 481 (1989).

[13] S.L. Rolston and G. Gabrielse, Hyperfine Interactions **44**, 233 (1988).

[14] G. Gabrielse, X. Fei, L.A. Orozco, R.L. Tjoelker, J. Haas, H. Kalinowsky, T.A. Trainor, and W. Kells, Phys. Rev. Lett. **63**, 1360 (1989).

[15] G. Gabrielse, X. Fei, L.A. Orozco, R.L. Tjoelker, J. Haas, H. Kalinowsky, T.A. Trainor, and W. Kells, Phys. Rev. Lett. **65**, 1317 (1990).

[16] H.F. Hess, G.P. Kochanski, J.M. Doyle, N. Masuhara, D. Kleppner, and T.J. Greytak, Phys. Rev. Lett. **59**, 672 (1987).

[17] J.M. Doyle, J.C. Sandberg, I.A. Yu, C.L. Cesar, D. Kleppner, and T.J. Greytak, Phys. Rev. Lett. **67**, 603 (1991); I.A. Yu, J.M. Doyle, J.C. Sandberg, C.L. Cesar, D. Kleppner, and T.J. Greytak, Phys. Rev. Lett. **71**, 1589 (1993).

[18] I.D. Setija, H.G.C. Werij, O.J. Luiten, M.W. Reynolds, T.W. Hijmans, and J.T.M. Walraven, Phys. Rev. Lett. **70**, 2257 (1993).

[19] R.S. Conti, B. Ghaffari, and T.D. Steiger, in *Proceedings of the Antihydrogen Workshop, Munich, 1992*, edited by J. Eades (CERN, Geneva, Switzerland, 1992).

[20] C.M. Surko, M. Leventhal, and A. Passner, Phys. Rev. Lett. **62**, 901 (1989); T.J. Murphy and C.M. Surko, J. Phys. **B23**, L727 (1990); T.J. Murphy and C.M. Surko, Phys. Rev. **A46**, 5696 (1992).

[21] T.J. Murphy and C.M. Surko, Phys. Rev. Lett. **67**, 2954 (1991).

[22] L.S. Brown and G. Gabrielse, Rev. Mod. Phys. **58**, 233 (1986).

[23] Robert Tjoelker, Ph.D. thesis, Harvard University, 1990.

[24] Xiang Fei, Ph.D. thesis, Harvard University, 1990.

[25] A.T. Aldred, B.D. Rainford, J.T. Hicks, and J.S. Kouvel, in *Low Temperature Physics LT-13*, edited by K.D. Timmerhaus, W.J. O'Sullivan, and E.F. Hammel (Plenum, New York, 1974) Vol. 2, p. 417; P.J. Nacher, G. Tastevin, and L. Wiesenfeld, Rev. Sci. Inst. **59**, 305 (1988); A. Tari and B.R. Coles, J. Phys. **F1**, L69 (1971); J. Crangle and W.R. Scott, J. Appl. Phys. **36**, 921 (1965).

[26] G. Gabrielse, Phys. Rev. **A27**, 2277 (1983).

[27] R.S. Van Dyke, Jr., P.B. Schwinberg, and H.G. Dehmelt, in *Atomic Physics 9*, edited by R.S. Van Dyck, Jr. and E.N. Fortson (World Scientific, Singapore, 1984).

[28] Emilio Segre, *Nuclei and Particles* (Benjamin, New York, 1965), p. 352-353.

[29] W.H. Wilkie and R.D. Birkhoff, Phys. Rev. **135**, A1133 (1964).

[30] A.P. Mills, Jr., P.M. Platzman, and B.L. Brown. Phys. Rev. Lett. **41**. 1076 (1978).

[31] D.A. Fischer, Ph.D. thesis, State University of New York at Stony Brook. 1984.

[32] D.A. Fischer, K.G. Lynn, and D.W. Gidley, Phys. Rev. **B33**. 4479 (1986).

[33] B.L. Brown, W.S. Crane, and A.P. Mills, Jr., Appl. Phys. Lett. **48**, 739 (1986).

[34] Kelvin Lynn (private communication).

[35] Carl Canter (private communication).

[36] D.T. Britton, P.A. Huttunen, J. Mäkinen, E. Soininen, and A. Vehanen, Phys. Rev. Lett. **62**, 2413 (1989).

[37] D.M. Chen, K.G. Lynn, R. Pareja, and B. Nielsen, Phys. Rev. **B31**. 4123 (1985)

[38] Capp Spindt (private communication).

[39] F.M. Jacobsen, M. Charlton, J. Chevallier, B.I. Deutch, G. Laricchia, and M.R. Poulsen, J. Appl. Phys. **67**, 575 (1990).

[40] Ben Brown (private communication).

[41] J.D. Jackson, *Classical Electrodynamics*, 2nd ed. (Wiley, New York, 1975), Sec. 14.2.

[42] R.S. Van Dyck, Jr., D.J. Wineland, P.A. Ekstrom, and H.G. Dehmelt, Appl. Phys. Lett. **28**, 446 (1976).

[43] G. Gabrielse, Phys. Rev. **A29**, 462 (1984).

[44] F.L. Walls and H.G. Dehmelt, Phys. Rev. Lett. **21**, 127 (1968).

[45] D.J. Wineland and H.G. Dehmelt, J. Appl. Phys. **46**, 919 (1975).

[46] T.J. Murphy and C.M. Surko, Phys. Rev. **A46**, 5696 (1992).

[47] Anton Khabbaz (private communication).

[48] W.H. Cherry, Ph.D. thesis, Princeton University, 1958.

[49] Alexander Weiss, Ph.D. thesis, Brandeis University, 1982.

[50] Joseph N. Tan, Ph.D. thesis, Harvard University, 1992.

[51] Thanks to J. Tan and D. Hall for helpful suggestions about this general form.

[52] D.J. Wineland and H.G. Dehmelt, Int. J. Mass Spectrom. Ion Phys. **16**, 338 (1975); **19**, 251(E) (1976).

[53] R.S. Van Dyck, Jr., P.B. Schwinberg, and H.G. Dehmelt, in *New Frontiers in High Energy Physics*, edited by B. Kursunoglu, A. Perlmutter, and L. Scott (Plenum, New York, 1978).

[54] S.P. Vyatchanin, Dok. Akad. Nauk. SSSR **234**, 1295 (1977); Sov. Phys.—Dokl. **22**, 321 (1977).

[55] D.J. Wineland and W.M. Itano, Phys. Rev. **A20**, 1521 (1979).

[56] C.H. Tseng and G. Gabrielse (unpublished).

[57] D.J. Wineland, P. Ekstrom, and H.G. Dehmelt, Phys. Rev. Lett. **31**, 1279 (1973).

[58] F.L. Walls, Ph.D. thesis, University of Washington, 1970.

[59] H. Massey, Phys. Today **29**, 42 (1976).

[60] T.C. Griffith and G.R. Heyland, Phys. Rep. **39**, 243 (1978).

[61] G.R. Heyland, M. Charlton, T.C. Griffith, and G.L. Wright, Can. J. Phys. **60**, 503 (1982).

[62] R.C. Davidson, *Theory of Nonneutral Plasmas* (Benjamin, Reading, Mass., 1974).

[63] J.H. Malmberg, T.M. O'Neil, A.W. Hyatt, and C.F. Driscoll, in *Proceedings of the 1984 Sendai Symposium on Plasma Nonlinear Phenomena* (Tohoku U.P., Sendai, Japan. 1984), p. 31.

[64] C.F. Driscoll, in *Low Energy Antimatter*, edited by D. Cline (World Scientific, Singapore, 1986) p. 184.

[65] A summary of the most precise measurements can be found in *Review of Particle Properties*, Phys. Rev. **D45** (1992).

[66] J.M. Lockhart, F.C. Witteborn, and W.M. Fairbank, Phys. Rev. Lett. **38**, 1220 (1977); J.M. Lockhart, F.C. Witteborn, and W.M. Fairbank, Rev. Sci. Inst. **48**, 1 (1977).

[67] G. Gabrielse, L. Haarsma, and S.L. Rolston, Int. J. of Mass Spectrom. and Ion Proc. **88**, 319 (1989).

[68] W. Quint, R. Kaiser, D. Hall, and G. Gabrielse, Hyperfine Interactions **76**, 181 (1993).

[69] D.R. Bates and A. Dalgarno, *Atomic and Molecular Processes* (Academic Press, New York, 1962) p. 245.

[70] D.R. Bates, A.E. Kingston, and R.W.P. McWhirter, Proc. R. Soc. **A267**, 297 (1962); J. Stevefelt, J. Boulmer, and J.F. Delpech, Phys. Rev. **A12**, 1246 (1975).

[71] M.E. Glinsky and T.M. O'Neil, Phys. Fluids **B3**, 1279 (1991).

[72] L. Spitzer, Jr., *Physics of Fully Ionized Gases* (John Wiley and Sons, Inc., New York, 1962) p. 135.